

Development of Quantum Information Tools Based on Multi-Photon Raman Processes in  
Rb Vapor

Nikunj Kumar Prajapati

Galloway Township, New Jersey

Master of Science, College of William & Mary, 2017  
Bachelor of Science, Stockton University, 2015

A Dissertation presented to the Graduate Faculty  
of The College of William & Mary in Candidacy for the Degree of  
Doctor of Philosophy

Department of Physics

College of William & Mary  
August 2020

©2020  
Nikunj Kumar Prajapati  
All rights reserved.

## APPROVAL PAGE

This Dissertation is submitted in partial fulfillment of  
the requirements for the degree of

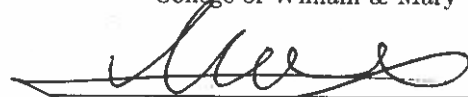
Doctor of Philosophy


  
Nikunj Kumar Prajapati


Approved by the Committee June 2020

  
Committee Chair

Irina Novikova, Professor, Physics  
College of William & Mary

  
Eugeny Mikhailov, Associate Professor, Physics  
College of William & Mary

  
William Cooke, Professor, Physics  
College of William & Mary

  
Todd Averett, Professor, Physics  
College of William & Mary

  
Ryan T. Glasser, Assistant Professor, Physics  
Tulane University

## ABSTRACT

Multi-photon nonlinear processes in atoms have served as important tools for quantum metrology, quantum communications, and quantum sensing. In this thesis, we experimentally address the interplay of various multi-photon Raman processes in hot Rb vapor, with the four-wave mixing (FWM) process being a central theme. FWM is the nonlinear response of a medium to a strong optical pump field inelastically scattering off atomic resonances and resulting in the generation of additional photons in different modes. FWM is a detrimental, but inherent part of electromagnetically induced transparency (EIT) and Raman based quantum memories. However, we were able to weaken the four-photon resonance by utilizing two-photon absorption to remove the additional photons without interfering with the signal beam. We also demonstrate the ability to tailor FWM to generate new photons in a controlled fashion for mode conversion. With this, we showed the conversion of 795 nm light to 420 nm light. While FWM is a source of noise in quantum memories, it can also be used for the generation squeezed twin-beams. Such beams have relative intensity noise reduced below the classical shot noise limit and share mode dependence based on the phase-matching conditions. Using this, we demonstrated that twin-beams can be generated with largely different spatial structure (optical angular momentum) and still share strong correlations, so long as the phase-matching conditions are satisfied. We then constructed and demonstrated the operation of a polarization-based quantum interferometer using squeezed twin-beams and showed that our beams were entangled under the inseparability condition. Using this interferometer, we were also able to achieve squeezing at low detection frequencies, which is necessary for things like quantum imaging and gravitational wave detection. We also demonstrated that squeezed twin-beams can be utilized to enhance the sensitivity of two-photon absorption spectroscopy. This research has touched on many different subjects related to quantum information science and improved upon some of the tools needed for the implementation of such technologies.

## TABLE OF CONTENTS

Acknowledgments . . . . .	iv
Dedication . . . . .	v
List of Figures . . . . .	vi
CHAPTER	1
1 Introduction . . . . .	1
1.1 Four-Wave Mixing in Quantum Memories . . . . .	2
1.2 Frequency Conversion via Four-Wave Mixing . . . . .	4
1.3 FWM as a Source of Squeezed Light . . . . .	5
1.3.1 Squeezed Light and Transfer of Optical Angular Momentum . . . . .	7
1.3.2 Squeezed Light for a Quantum Interferometer . . . . .	8
1.3.3 Spectroscopic Measurement using Squeezed Light . . . . .	9
1.4 Overview of Thesis . . . . .	10
2 Theory . . . . .	12
2.1 Propagation through a medium . . . . .	12
2.2 Semi-Classical Approach to Light-Atom Interactions . . . . .	15
2.2.1 Selection Rules . . . . .	16
2.2.2 Density Matrix Formalism . . . . .	18
2.3 Coherent Nonlinear Processes . . . . .	22
2.3.1 Far-Detuned Raman Resonance . . . . .	25
2.3.2 Electromagnetically Induced Transparency . . . . .	27
2.4 Four-Wave Mixing . . . . .	29

2.4.1	Frequency Conversion via FWM . . . . .	32
2.4.2	FWM as a Source of Decoherence of the Dark State . . . . .	35
2.4.3	FWM for Transfer of Optical Angular Momentum . . . . .	38
2.5	Quantization of the Electromagnetic Field . . . . .	41
2.5.1	Quantum Limit of Optical Measurements . . . . .	45
2.5.2	Squeezed light from FWM . . . . .	47
2.5.3	Balanced Homodyne Detection for Squeezing Quadrature Measurements . . . . .	49
3	Suppression of FWM in Quantum Memory . . . . .	54
3.1	Experimental arrangements . . . . .	54
3.2	Resonant EIT case . . . . .	57
3.3	Off-resonant Raman case . . . . .	63
3.4	Conclusion . . . . .	66
4	Comparison of collimated blue light generation in $^{85}\text{Rb}$ atoms via the D1 and D2 lines . . . . .	68
4.1	Experimental arrangements . . . . .	69
4.2	CBL generation via the $D_1$ line . . . . .	71
4.3	CBL generation via the $D_2$ line . . . . .	76
4.4	Simplified theoretical simulations . . . . .	80
4.5	Conclusion . . . . .	83
5	Experimental Generation of FWM Squeezing . . . . .	85
5.1	Beam Preparation . . . . .	86
5.2	Beam Monitoring . . . . .	87
5.3	FWM and the Phase Matching Conditions . . . . .	89
5.4	Pump Filtering and Intensity Difference Squeezing Detection . . . . .	90

6	Optical Angular Momentum manipulations in a Four Wave Mixing process . . .	94
6.1	Experimental arrangements . . . . .	96
6.2	Optical angular momentum conversion with single vortex beams . . . . .	98
6.3	Optical angular momentum conversion for a composite vortex pump field	101
6.4	Conclusion . . . . .	104
7	Implementation of Polarization-Based Truncated SU (1,1) Interferometer in Hot Rb Vapor . . . . .	105
7.1	Introduction . . . . .	105
7.2	Experimental Arrangements . . . . .	108
7.3	Analytic Description of the Optical Joint Quadrature Control and Detection . . . . .	111
7.4	Measurement of Squeezed Joint Quadratures and Entanglement . . . . .	118
7.5	Conclusion . . . . .	121
8	Enhancement of Raman Two-Photon Spectroscopy using Squeezed Light . . .	123
8.1	Introduction . . . . .	123
8.2	Raman Resonance Response of $5D_{3/2}$ State . . . . .	126
8.3	Conclusion . . . . .	131
9	Conclusion and Outlook . . . . .	133
	Bibliography . . . . .	138
	Vita . . . . .	159

## ACKNOWLEDGMENTS

I would like to begin by thanking my advisor, Irina Novikova. Not only did she help me grow as a scientist, but she fostered my personal and professional development as well. My time here under her guidance has been a delight. I truly look upon her as a role model in science. She continually pursues outreach opportunities and leadership roles to help the science community progress. I thank Eugeny Mikhailov for his support on research projects, wonderful Russian sayings, and continual laughs in the lab. It all started with "blah1.m". I thank my colleague Savannah Cuozzo for advice on projects and being such a cheery and positive personality. I thank my other group members who I have worked with or around for the good times that we had in the lab and group meetings-Hana, Alex, Kangning, Melissa, Ziqi, Sophia, Scott, Jason, Micheal, Ravn, Mi, Nathan, Austin, Aiden, Gleb, Ellie, Haley, Hunter, Owen, and Josh. I also thank my predecessors for laying the groundwork for me to build upon.

During my time here, we have also collaborated with the group of Jon P. Dowling at LSU. I thank Jon and his group for the whacky, yet somehow productive discussion we had on quantum imaging. In this group: Lior Cohen, Elisha Siddiqui, Sefura Sharifi, Narayan Bhusal, ZhiHao Xiao, and Nicholas Lanning. I thank our collaborator, Alexandre Akoulchine from Swinburne University of Technology in Austria for discussions on collimated blue light generation. I also thank Patrick McArdle for useful discussions in on spectroscopic measurements which led me to think of applying squeezed light to Raman two-photon absorption.

My first introduction to physics was in high school, by a very enthusiastic teacher who made the learning process enjoyable, Sean Swanson. This placed me on the path to physics and was further helped along in undergrad by all the professors who taught at Stockton University-Sipra Pal, Neil Aaronson, Yizhak Sharon, Jason Schulman, Joseph Trout, Lui Fang, Benjamin Agyare, Russell Manson, and Monir Sharobeam.

My time during courses was not the easiest and so I thank the class of graduate students that I came in with for the support through the process. I was lucky that my classmates shared the same interests as me and were better than me at physics. It gave me something to strive for which made for a great environment for growth. I feel as though I have made some life long friends through this process. I thank the department faculty and staff for the good times over the past 5 years. I also want to thank all of my committee members for taking part in this process and guiding me during the annual reviews.

Last, but not least, I thank my family for always telling me to aim higher and pushing me to challenge myself and the support throughout my life.



I present this thesis in honor of my parents.

## LIST OF FIGURES

2.1	Two-level diagram with incoming photon of energy $\omega$ . . . . .	18
2.2	Three-level diagram with incoming photons of energy $\omega_a$ and $\omega_b$ . The decay rates are given by $\gamma'$ , $\gamma$ , and $\tilde{\gamma}$ . . . . .	23
2.3	Plot of absorption of probe field in Eq. 2.58 as a function of the two-photon detuning for different values pump detuning $\Delta$ , where $\gamma_{12} = 0$ and $\gamma_{13}$ is set to $2\pi \cdot 6MHz$ . . . . .	27
2.4	(a) shows the energy conservation of the FWM process where two pump photons are absorbed while a probe photon is added and a new conjugate photon is generated with energy to match the difference. The solid lines represent real states, while dashed are virtual states marking multi-photon resonances. (b) shows the momentum conservation. . . . .	31
2.5	Level diagrams of some possible configurations of FWM, where solid lines represent input fields and dashed lined represent new fields. Many more combinations exist. . . . .	34
2.6	Level diagram of FWM in $^{85}Rb$ involving the upper 5D state. . . . .	35
2.7	Three-level diagram of FWM where, $\omega_a$ is the probe, $\omega_b$ is the pump, and $\omega_c$ is the conjugate. The decay rates $\gamma'$ , $\gamma$ , and $\tilde{\gamma}$ are the same as those in Fig. 2.2. . . . .	35
2.8	Shown are the equiphase surfaces, phases, and intensity map of the OAM modes for different $\ell$ numbers. Taken from [157]. . . . .	40
2.9	(a) shows the noise noise as a fuzz for the probe beam after amplification and the blue dashed lines are shot noise for a beam of equivalent power. (b) shows the noise as a fuzz for the conjugate beam after amplification and the blue dashed lines are shot noise for a beam of equivalent power. (c) shows the joint-amplitude quadrature with squeezing along the difference and anti-squeezing along the sum. (d) shows the joint-phase quadrature with squeezing along the sum and anti-squeezing along the difference. . . .	50
2.10	(a) shows the detection using homodyne detection of a local oscillator (LO) mixed with a vacuum. (b) shows homodyne detection, but with a squeezed vacuum input. . . . .	51

3.1	Level diagram of Rb atom based quantum memory. . . . .	55
3.2	Optical schematic of setup. ECDL and Ti:Sapph denote the two independent lasers used in the experiment (external cavity diode laser and Ti:Sapph cw laser, correspondingly). Optical path of the control field is shown in red, the Raman pump laser in green, and the probe and stokes fields are correspondingly blue and black. See text below for abbreviations. . . . .	56
3.3	Possible realizations of a ladder Raman absorption resonance for the stokes field in EIT configuration using only $^{85}\text{Rb}$ atoms ( <i>a, b</i> ), or using $^{85}\text{Rb}$ for EIT and $^{87}\text{Rb}$ for Raman absorption ( <i>c</i> ). $\Delta$ is 80 MHz, and $\Delta_{\text{HF}}$ is 3035 MHz. . . . .	59
3.4	( <i>a</i> ) Measured transmission for stokes (black) and control (red) optical fields as the Raman pump frequency is scanned across the two-photon absorption resonance in the level configuration shown in Fig. 3.3(a). Both control and stokes fields experience absorption since they are simultaneously in a two-photon resonance with the pump. ( <i>b</i> ) Stokes field transmission vs Raman pump frequency using $^{87}\text{Rb}$ resonances, as shown in Fig. 3.3(c). The control field has no absorption in this case, and thus not shown. All curves are normalized to the transmission value without Raman pump. Vertical dashed lines indicate the optimal operational frequency. Raman pump power was 180 mW for ( <i>a</i> ) and 220 mW for ( <i>b</i> ). . . . .	60
3.5	Transmission of ( <i>a</i> ) probe field and ( <i>b</i> ) stokes field as functions of two-photon frequency difference between the control and probe field with (red) and without (blue) Raman pump-induced stokes absorption. All curves are normalized to the input probe field power. Raman pump power for both graphs is 220 mW. Here $I_0$ and $I_S$ are the heights of the probe transmission peak without and with the Raman pump, correspondingly. . . . .	61
3.6	( <i>a</i> ) Suppression factor for stokes output field as a function of Raman pump power for EIT configuration. ( <i>b</i> ) Probe field suppression as a function of the stokes field suppression. The data shown in blue correspond to seeded probe field (no input stokes), while the red data points correspond to the seeded stokes fields (no input probe). Each data point corresponds to the average of five independent measurements, with the error bar equal one standard deviation. Dashed blue line corresponds to the reference reduction factor for the output probe field, if the input stokes field was attenuated <i>before</i> entering the vapor cell. . . . .	62

3.7	(a) Level configuration used for the FWM suppression in the Raman configuration. The control field one-photon detuning from the $F = 3 \rightarrow F' = 3$ transition is $\Delta = 200$ MHz, and the Raman pump field wavelength is 762.1038 nm. (b, c) Examples of the two-photon resonances for the probe and stokes fields with and without Raman pump of 80 mW, correspondingly. All curves are normalized to the input probe field power. Here again $I_0$ and $I_S$ are the heights of the probe transmission peak without and with Raman pump, correspondingly, and $I_b$ is the background level, corresponding to the probe transmission away from the two-photon resonance. . . . .	64
3.8	Measured transmission for the stokes and control optical fields as the Raman pump frequency is scanned across the absorption resonances. Raman pump power is 80 mW. Vertical dashed line indicates the optimal operational frequency. . . . .	65
3.9	(a) Suppression factor for stokes output field as a function of Raman pump power for far-detuned Raman configuration. (b) Probe field suppression as a function of the stokes field suppression. The data shown in blue correspond to seeded probe field (no input stokes), while the red data points correspond to the seeded stokes fields (no input probe). Each data point corresponds to the average of five independent measurements, with the error bar equal one standard deviation. Dashed blue line corresponds to the reference reduction factor for the output probe field, if the input stokes field was attenuated <i>before</i> entering the vapor cell. . . . .	66
4.1	The optical layout of the experimental setup. ECDL- $D_1$ , ECDL- $D_2$ , and Ti:Sapph denote three independent lasers used in the experiment. The optical paths of the $D_1$ , $D_2$ , and Ti:sapph pump lasers and the generated blue light are show in, red, black, green, and blue, respectively. Inset shows relative orientation of the optical beams. See text for the abbreviations. . .	70
4.2	Interaction configuration through the $5P_{1/2}$ intermediate level: lower pump (795 nm) and the upper pump (762 nm) excite Rb atoms to the $5D_{3/2}$ level, followed by the emission of $5.032 \mu\text{m}$ (not detectable) and collimated blue light at 422 nm. The repump field is tuned to the $5S_{1/2}, F = 2 \rightarrow 5P_{3/2}$ transition. . . . .	72

4.3	Power of the generated blue light as the lower pump was swept across: (a) $5S_{1/2}, F = 3 \rightarrow 5P_{1/2}$ transition, (b) $5S_{1/2}, F = 2 \rightarrow 5P_{1/2}$ , and (c) 1.2 GHz above $5S_{1/2}, F = 2 \rightarrow 5P_{1/2}$ transitions. The upper pump was tuned to 762.1036 nm for (a,b), and 762.1054 nm for (c). Four different polarization configurations of the two pump lasers are shown: linear parallel (red, solid line), linear orthogonal (magenta, solid line), circular parallel (blue, dashed line), and circular orthogonal (green, dashed line). The powers of both lower pump ( $D_1$ laser) and the repump ( $D_2$ laser) were kept at 16 mW, and the power of the upper pump (Ti:Sapph laser) at 200 mW. The zero detuning of the $D_1$ pump corresponds to the cross-over transition of the $5S_{1/2}, F = 3 \rightarrow 5P_{1/2}$ state. . . . .	73
4.4	Generated CBL power as a function of normalized power of each pump and repump fields. For each individual dependence the power of one laser was varied between zero and its maximum value, while the other two lasers were kept at their maximum powers: 65 mW for the lower pump (795 nm), 200 mW for the upper pump (762 nm), and 17 mW for the repump laser (780 nm). The laser detuning corresponded to the conditions for the maximum CBL power as shown in Fig. 4.3(a). . . . .	75
4.5	Generated CBL power as a function of normalized power of each pump and repump field. As in Fig. 4.4, for each individual measurement the power of one laser was varied between zero and its maximum amount, while the other two lasers were kept at their maximum powers: 65 mW for the lower pump (795 nm), 200 mW for the upper pump (762 nm), and 17 mW for the repump laser (780nm). The laser detuning corresponded to the conditions for the maximum CBL generation in Fig. 4.3(c), approximately +1.2 GHz blue of the $5S_{1/2}, F = 2 \rightarrow 5P_{1/2}$ transition. . . . .	77
4.6	Interaction configuration for CBL generation via the $5P_{3/2}$ intermediate state, that uses the lower pump (780 nm) and the upper pump (776 nm) to excite Rb atoms into the $5D_{3/2}$ state, resulting in emission of $5.032 \mu\text{m}$ (not experimentally observed) and collimated blue light (422 nm). The repump (795 nm) field is tuned to the hyperfine ground state opposite of the lower pump. . . . .	77
4.7	Measured CBL power for varying polarizations of lower pump (780 nm) and upper pump (776.1568 nm) as the lower pump is swept across the hyper-fine split ground states. The considered polarization arrangements for the two pumps are: linear parallel (red, solid line), linear orthogonal (magenta, solid line), circular parallel (blue, dashed line), and circular orthogonal (green, dashed line). . . . .	78

4.8	Generated CBL as a function of normalized power of the pump and repump fields. As in Fig. 4.4, for each individual dependence, the power of one laser was varied between zero and its maximum value, while the other two lasers were kept at their maximum powers: 17 mW for the lower pump (780 nm), 200 mW for the upper pump (776 nm), and 65 mW for the repumper (795 nm). The laser detuning corresponded to the conditions for the maximum CBL generation in Fig. 4.7(b), near $S_{1/2}F = 2 \rightarrow 5P_{3/2}F'$ transition. The upper pump wavelength was fixed at 776.1568 nm. . . . .	79
4.9	Calculated CBL gain as a function of either pump Rabi frequency. While the Rabi frequency of one of the pump fields is varied, the other is maintained at its maximum value of $5 \times 10^{10}$ Hz. In (a) the Rabi frequencies change in the range similar to those used for experimental data in Fig. 4.4. In (b) the range of variation is increased by a factor of 10 to display the more complete power dependence. For these simulations we used parallel circular polarizations for all optical fields; however, the same general behavior is observed for other polarization configurations. . . . .	82
4.10	Calculated CBL gain as a function of repump Rabi frequency. For these simulations we used parallel circular polarizations for all optical fields, and the Rabi frequencies of the lower and upper pump fields of $2 \times 10^{10}$ Hz and $5 \times 10^{10}$ Hz, corresponding to the calculated maximum CBL gain. . . . .	82
4.11	(a) Calculated CBL gain as a function of lower pump frequency for the four polarization arrangements tested in the experiment. For these simulations the Rabi frequencies of the lower and upper pump fields of $2 \times 10^{10}$ Hz and $5 \times 10^{10}$ Hz, and the upper pump was resonant with the corresponding optical transition. (b) Modification of the CBL gain lower power dependence for different polarization arrangements. The simulation parameters are identical to those using in Fig. 4.9. . . . .	83
5.1	Full schematic for the generation and detection of squeezed light via FWM	86
5.2	This is the cutout of the beam prep which generates the probe and pump fields. . . . .	87
5.3	(a) The absorption spectroscopy setup. (b) The oscilloscope trace, blue is signal for the absorption spectroscopy of an Rb natural abundance cell and red is the output of the EOM filtered by the etalon as the laser frequency is swept. . . . .	88

5.4	(a) is the interaction in the cell with phase matching angles shown and (b) is the FWM level diagram for generating squeezed light where $\Delta_{HF}$ is the hyper-fine splitting. . . . .	90
5.5	The probe (left) and conjugate (right) OAM mode structures as a result of FWM and the effects as the two-photon detuning is changed. . . . .	91
5.6	(a) The detection portion of the schematic. (b) The output from the spectrum analyzer. . . . .	92
5.7	(a) The shot noise measurement method for the apparatus. (b) The calibration of the spectrum analyzer noise. . . . .	93
6.1	Realization of the four-wave mixing in $^{85}\text{Rb}$ vapor: (a) level diagram and (b) geometrical arrangement. (c) Example of the output probe (left) and generated stokes (right) field with mutual difference of $\Delta\ell = 4$ . . . . .	95
6.2	The optical layout of the experimental setup. A single laser is used to generate all outputs. The high-power pump (red) is output through a fiber dock system while the lower power pump output is in free space and later used to generate the probe (blue). The stokes (black) optical field is generated through FWM in the cell. The set-up has four main sections; probe prep, OAM prep, interaction, noise detection, and imaging. Abbreviations and explanations are given in the text. . . . .	96
6.3	<i>Left:</i> Intensity squeezing (left axis) and the FWM amplification for the probe and Stokes fields (right axis) as functions of the two-photon detuning, measured for (a) $\ell_{\text{probe}} = +1$ , $\ell_{\text{pump}} = +1$ , and (b) $\ell_{\text{probe}} = +1$ , $\ell_{\text{pump}} = -1$ configurations. Images on the left show the flat-front interferograms of the input pump and probe fields at the cell's position, and on the right — the interferograms of the output probe and Stokes fields for each configuration. . . . .	99
6.4	Composite vortex pump beam: (a) experimentally measured interferogram of the pump beam at the location of the Rb cell, (b) simulated pump beam transverse intensity distribution, described by Eq. (6.2), and (c) a phase map of the simulated pump field. . . . .	101
6.5	Top row: (a1, a3) experimentally measured and (a2, a4) numerically simulated intensity profiles of the generated Stokes field for the composite pump field, containing two $\ell = \pm 1$ spatially-separated optical vortices, correspondingly. Middle row: spiral interferograms of each beam. Bottom row: Fourier mode decomposition of the radial intensity distributions of the spectral interferograms for different LG mode indices $\ell$ . . . . .	103

6.6	Measured intensity squeezing (left axis) and the FWM amplification for the probe and stokes fields (right axis) as functions of the two-photon detuning, measured for (a) $\ell_{\text{probe}} = +1$ , composite pump $\ell_{\text{pump}} = 2 \times 1$ , and (b) $\ell_{\text{probe}} = +1$ , $\ell_{\text{pump}} = 2 \times (-1)$ configurations. . . . .	103
7.1	(a) Traditional SU(1,1) interferometer: the first cell acts as a noiseless amplifier (shown in blue) while the second cell and the balanced photodiodes serve as a detector (shown in pink).(b) A truncated SU(1,1) interferometer, in which the second cell is replaced with balanced homodyne detectors with external local oscillators (LOs) (shown in pink). (c) A polarization-based truncated SU(1,1) interferometer. Here the amplifier cell is also used to generate local oscillators and combined with the quantum fields using polarization optics, and then final detection is carried out by a single balanced photodiode. . . . .	106
7.2	(a) The level diagram of $^{85}\text{Rb}$ and the corresponding FWM process where the probe (blue), pump (red), and conjugate (black) form a four-photon resonance and couple the two hyperfine ground states through a virtual level detuned $\approx +1$ GHz from the $5P_{1/2}$ excited state. The pump frequency was fixed at 794.9727 nm. (b) The schematics of the experimental apparatus for the polarization based truncated SU(1,1) interferometer (see text for abbreviations). Images are taken from Ref.16. . . . .	108
7.3	Individual photo-currents of each port of the balanced photodetector as the local oscillator phases are scanned with respect to their squeezed fields to demonstrate the high interference visibility. Flat regions correspond to pump leakage measurements (see text for details). . . . .	110
7.4	(a) The differential current (red, dashed) and noise power (red, solid) as a function of the phase $\phi(t)$ swept from 0 to $2\pi$ for the case $\phi_\alpha = \phi_\beta$ ( $\Delta\phi = 0$ ). (b) The differential current (blue, dashed) and noise power (blue, solid) as a function of the phase $\phi(t)$ swept from 0 to $2\pi$ for the case $\phi_\alpha = \phi_\beta$ ( $\Delta\phi = \pi$ ).116	116
7.5	(a) Measured joint quadrature noise power for the cases 1 ( $\Delta\phi = 0$ ) and the case 2 (blue, $\Delta\phi = \pi$ ) as the phase $\phi(t)$ of the LOs is swept with respect to the squeezed fields, for the case of seeded squeezed field. Solid green line shows the minimum detected quadrature noise, $\approx -2dB$ below the shot noise (dashed green line). (b) Analogous measurements performed with the vacuum-seeded input field, showing the joined quadrature noise power as a function of the phase $\phi(t)$ . . . . .	118



7.6	(a) The noise spectrum for intensity squeezing (blue) obtained within a single rail as a function of the detection frequency. Green line represent the shot noise level. (b) Analogous measurements for the noise spectrum of the dual rail interferometer output. The inset zooms on the lower detection frequencies, and was measured using a different spectrum analyzer with less low frequency noise. . . . .	121
8.1	(a) shows the level diagram of the $^{85}\text{Rb}$ D1 line and the corresponding FWM process where the probe (blue), conjugate (black), and pump (red) optical fields are shown. $\Delta$ (1GHz) is the two-photon detuning of the probe and pump and $\Delta_{HF}$ (3036 MHz) is the hyper-fine splitting of the $5S_{1/2}$ ground state. (b) shows one of the ladder level configurations of this method to probe highly excited states using the Raman pump beam (green). (c) shows the lambda configuration of this method which can be used to probe low energy states and vibrational states of molecules and crystals. . . . .	124
8.2	Shaded region shows the possible range of energies probable by the two-photon absorption of the probe field, limited by the range of our Ti:Sapph laser. . . . .	125
8.3	(a) shows the experimental schematic of the experiment, see text for details. (b) shows the two-photon transition ( $5S_{1/2}, F = 2 \rightarrow 5D_{3/2}$ ) of the probe field coupled to the Raman pump field. (c) shows the noise signal produced from absorbing the probe field as the detuning of the Raman pump ( $\Delta_{Ramana}$ ) is swept by 200 MHz. The hyper-fine splitting of the $5D_{3/2}$ state are labeled accordingly. . . . .	126
8.4	(a) and (c) show the differential intensity of the photodetectors as the pump frequency is tuned through the two-photon resonance with the 5D state for pump powers of 10 mW and 1 mW, respectively. (b) and (d) show the differential noise of the photodetectors picked up by the spectrum analyzer as the pump frequency is tuned through the two-photon resonance with the 5D state for pump powers of 10 mW and 1 mW, respectively. The SA sweep time here is 8 seconds, the resolution bandwidth is 10kHz and the video bandwidth is 10 Hz . . . . .	127
8.5	(a)-(e) The mesh plot of noise traces, as the Raman pump power is changed and frequency is scanned. The different plots are for varying temperatures, as labeled. The black trace outlines the power dependence of the absorption signal for the $5S_{1/2}, F = 2 \rightarrow 5D_{3/2}, F'' = 1$ transition which is extracted for the power dependent traces in Fig. 8.6 . . . . .	129

8.6	(a) shows the power dependence shown by the black trace in Fig. 8.5 (a)-(e) for the $5S_{1/2}, F = 2 \rightarrow 5D_{3/2}, F'' = 1$ two-photon transition absorption. In this, the power dependence at different Raman cell temperatures are plotted as different colors, as labeled. (b) shows the atomic density dependence of the two-photon absorption for a Raman pump power of 10 mW, shown by the dashed black outline in (a) . . . . .	130
9.1	(a) shows the cross correlation of two classical beams. (b) shows the cross correlation between the two-mode squeezed twin-beams. . . . .	136

DEVELOPMENT OF QUANTUM INFORMATION TOOLS BASED ON  
MULTI-PHOTON RAMAN PROCESSES IN RB VAPOR

# CHAPTER 1

## Introduction

Quantum information technologies have been rapidly developing over the last 30 years offering a wide range of applications. In quantum sensing and metrology, they have been used for gravitational wave detectors [1–5], bio-sensing [5, 6], quantum imaging [7–10], and weak RF detection using Rydberg atoms [11, 12]. In quantum communications, they enabled absolutely secure information transfer offered by entangled light [7, 13–16] and increased channel capacity through the use of quantum and structured light [17, 18]. In this thesis, we make complimentary advancements to the fundamental processes which govern the quantum information revolution.

At its heart, the advancement of quantum information technologies has come about from the coherent control of light matter interactions and the resulting nonlinear effects, made possible by the advent of the laser in 1961 by Theodore Maiman [19]. While nonlinear effects involving electric and magnetic fields like the Pockels effect and the Kerr effect were discovered in the late XIX century, a strong source of coherent electromagnetic fields was necessary for other polarization effects, made available by the laser. This was a necessary component for the coherent control of atomic populations and light matter inter-

actions [20]. The year the laser was invented was also the year second harmonic generation was first demonstrated by Franken et. al. [21], proving the earlier development of nonlinear polarization theories by Dirac [22]. Following this initial discovery, many other parametric nonlinear effects followed: frequency sum and difference generation, optical parametric amplification, Raman scattering, etc [20, 23–25]. Also observed were coherent nonlinear effects like electromagnetically induced transparency and Raman absorption [20].

The nature of these nonlinear responses depend on the medium used. In the first demonstration of second harmonic generation, a crystal exhibiting  $\chi^{(2)}$  (second order in polarization response) nonlinearity was used to convert red 794 nm light to blue 347 nm light [21]. Non-centrosymmetric crystals break inversion symmetry and thus allow  $\chi^{(2)}$  processes [20, 23]. However, when comparing the strength of the nonlinearity per atomic density, alkali vapors offer more promise and added benefits based on the application [26]. Since vapors are symmetric under rotation and translation, they only show odd order contributions from the susceptibility. The most common and explored is the  $\chi^{(3)}$  nonlinearity, that gives rise to four-wave mixing (FWM), polarization self rotation, the Kerr effect, and other processes [26]. In this thesis, we look at FWM as both a positive and negative factor in quantum information science.

## 1.1 Four-Wave Mixing in Quantum Memories

In the realm of quantum communications, quantum memories are essential for long range transmission of entangled states [27]. There are two main processes which can be used to generate a quantum memory. One process relies on engineered absorption or photon echos inhomogeneously broadened media. The two main processes, controlled-reversible-inhomogeneous-broadening (CRIB) and atomic frequency combs (AFC) are such photon echo based memories [28]. In both, the signal pulse is absorbed coherently by the

in-homogeneously broadened atomic ensemble. Upon the application of a  $\pi/2$  pulse, the ensemble begins to dephase and the pulse is stored. However, to retrieve the pulse from CRIB or pulse train from AFC, a  $\pi$  pulse must be applied at the exact rephasing time for efficient retrieval. The coherent ensemble then echoes the signal photons [29]. While these protocols have seen storage times on the order of hours [28, 30] and have great promise as a memories, more versatility is needed [28].

Optically-controlled memories do not have this limitation. The storage and retrieval is controlled by a strong pumping laser which reversibly maps the optical signal on the ground state coherence of non-interacting superposition of spin-states, which can then be retrieved on-demand with a second pump pulse [28, 31]. This non-interacting superposition is the dark state and can be produced by the two-photon processes of on-resonant electromagnetically induced transparency (EIT) [32–34] and off-resonant Raman absorption [35–37]. These processes have been observed in alkali vapors [32–37], crystals containing nitrogen-vacancy centers in diamonds [38–40], and even molecules [41]. Alkali vapors have the largest storage times of the optically controlled memories, primarily limited by the collisional depahasing of the dark state rather than the decay between the two states comprising the superposition [28]. However, the storage times are still much smaller than those observed for quantum memories utilizing engineered absorption. For this reason, hybrid schemes incorporating both optically controlled memories and engineered absorption have been conceived [28].

Unfortunately, optically controlled memories share a deficiency. The strong pump field used to optically trap the coherent ensemble results in inelastic Raman scattering, known as four-wave mixing. This is detrimental to these memories since adds excess noise photons into the signal, thereby decreasing the fidelity of these quantum memories [28, 36, 37, 42–49]. Methods to subvert this added noise have involved the optimization of frequencies [36, 50], polarizations [51], or introducing an optical cavity for spectral

filtering [52, 53], but each has its own limitations. The suppression of the FWM effect has also been attempted with the use of higher-order nonlinear effects [54, 55]. However, the introduction of such effects can lead to unwanted modifications of the ground-state coherence [56]. More recently, it was shown that the overall FWM gain could be suppressed by sufficient absorption of the conjugate field as it is generated. The method for absorption relies on Raman two-photon absorption using separate isotopes of the given atoms mixed into the coherent ensemble [42, 43, 45, 57]. This method drastically limits the effects of FWM and can increase the fidelity of EIT and Raman based quantum memories without altering the dark state.

## 1.2 Frequency Conversion via Four-Wave Mixing

While FWM plays a negative role in quantum memories, it is useful in applications where the efficient frequency conversion of light is necessary. For quantum communications, there is a need to switch between telecom wavelengths (1550 nm) for transmission channels and quantum memory wavelengths (795 nm in Rb atoms) for repeater stations. Any loss during conversion results in noise and loss of entanglement [8]. FWM is a parametric nonlinear response which can be used to generate collimated light with the frequency-sum or frequency-difference of the input fields and scattered photons from resonance decays [20]. By tuning the input field alignment and frequencies, one can tailor the output light as desired. A broad variety of interaction configurations exist to this effect and among them, the scheme involving two-photon excitation reaching higher energy levels have been investigated for efficient frequency up-conversion [58–60], single-photon frequency conversion [61], quantum memory [62], active filtering and selective non-linearity suppression [43, 63], quantum noise dynamics [64], etc.

The configurations involving higher energy levels of alkali vapors also offer other in-

interesting possibilities for nonlinear optics. The population inversion guaranteed between certain excited levels with appropriate lifetimes and branching ratios, result in amplified spontaneous emission (ASE) and spontaneously-seeded four-wave mixing for the involved optical transitions. A lot of attention was recently given to the generation of collimated blue light (CBL) at 420.3 nm via the  $5S_{1/2} \rightarrow 5P_{3/2} \rightarrow 5D_{5/2}$  transition in Rb vapor [65–72]. Such interacting systems have been successfully used to study the interplay of co-existing nonlinear processes [44, 73], the effects of externally-seeded optical fields [74] and of the ground-state repumping [75, 76], and of optical resonators [77]. It also served as a tool for studies on orbital angular momentum conservation and manipulations in nonlinear processes [78–80].

### 1.3 FWM as a Source of Squeezed Light

FWM can also be used to prepare non-classical states of light, specifically squeezed states. Squeezed states are similar to coherent laser light in regards to being a minimum uncertainty state in phase and amplitude [23, 24, 81]. However, for squeezed light, one observable has noise below this limit (squeezed), while the other has noise above this limit (anti-squeezed), introduced more precisely in Ch. 2. The original definition of squeezing referred to noise reduction in the electric field amplitude or phase quadrature noise, but has since extended to sub-poissonian photon number distributions, polarization squeezing, and other observables [26].

The first demonstration of 0.3 dB squeezed light was in 1985 by Slusher et al. [82] using FWM in sodium vapor, nearly 25 years after the invention of the laser and first demonstration of second harmonic generation. Since then improvements in detectors, electronic noise suppression, and the reduction of loss in optical elements has led to substantial increases in squeezing. Nearly 9 dBs of squeezing has been observed in alkali vapors [83, 84],



7 dBs in optical fibers [85], and over 15 dBs in crystals [86]. Due to the versatility of these sources, squeezed light has seen use in a variety of situations including entangled pair generation for quantum communications [7, 13–16], correlated images for quantum imaging [7, 87, 88], bio-sensing [89, 90], enhancements in magnetometers [91, 92], gravitational wave detection [93], and others given by these reviews articles [26, 87, 94, 95].

FWM in atomic vapors produces bright two-mode squeezed twin-beams. They are formed when the spontaneous inelastic scattering of a pump field off of the ground state coherence is stimulated by a seed (probe) field. The result is the simultaneous generation of additional probe photons and conjugate photons. The pump, probe, and conjugate photons complete a four-photon resonance involving the hyper-fine split ground state and two intermediary states coupling the conjugate and probe to the pump beam. The spontaneous addition of photons to each beam results in extra noise for the individual twin beams. However, since the addition occurs in a pair-wise fashion, the twin-beams share these fluctuations. The result is the increased signal strength without an increase in the differential intensity noise of the probe and conjugate twin beams. The differential measurement of the two beams result in a lower noise floor than if two classical beams were used [23, 24, 81]. The twin beams share quantum correlations in phase and intensity and as such, they are said to be entangled [96, 97].

Squeezed light generated in atomic vapors have some key benefits to their counterparts. As stated before, the nonlinearity of atomic ensembles near resonance is much larger than the those of crystals or fibers. This allows for squeezed light generation at lower pump powers and removes the need for cavities [26]. While the level of squeezing produced by FWM in vapors is lower, there are still certain advantages. For example, squeezed light produced by FWM in Rb vapor is near resonant with the D1 line, the same frequency as EIT and Raman quantum memories [32–37]. FWM can also be used for differential absorption measurements to monitor plasmons [83] or molecules and cells [90].

For applications in communications, FWM is a source of entanglement and can transfer complicated phase structure from the input beams to the newly generated field [8, 18], thanks to the multi-mode nature of the FWM.

### 1.3.1 Squeezed Light and Transfer of Optical Angular Momentum

An important facet of squeezed light generated by FWM is its multi-mode nature and ability to transfer phase information between the correlated twin-beams [8, 98, 99]. A useful resource carrying complex phase and spatial information is structured light, such as beams carrying optical angular momentum (OAM) [100–102]. This resource rapidly became useful for a wide range of applications, from optomechanical manipulations [103, 104] to super-resolution imaging [105, 106]. In quantum information science it has been used for the generation of hyper-entanglement [107, 108], quantum multiplexing [109], etc. Nonlinear optical processes used for OAM manipulations have been observed [8, 99, 110–113], as the OAM phase-matching conditions make it possible to control the spatial structure of the generated optical field by shaping the profiles of the strong pump and weak probe fields before the interaction.

Twin-beams generated in this manner also exhibit the same level of noise reduction as non-structured twin-beams [8, 18], even when they have very different spatial structure [18]. The ability to maintain spatial correlations in this manner also opens the possibility for quantum imaging. Mapping correlations of complex structured light may help in gaining resolution in imaging [105]. It is also possible to use twin-beams carrying OAM in communications to extend the channel dimensionality for information propagation [114, 115]. OAM demodulation schemes for this already exist [100, 116].

### 1.3.2 Squeezed Light for a Quantum Interferometer

To this point, we have simply referenced intensity correlations and the photon number distribution when considering squeezing. However, for communications and sensing, enhanced phase measurements are also necessary. These can be obtained by interferometers which incorporate squeezed light. Such devices are grouped into two categories, interferometers defined by the  $SU(2)$  symmetry group and those defined by the  $SU(1,1)$  group [117].  $SU(2)$  interferometers are most similar to classical interferometers where a single mode squeezed vacuum is injected into a dark port of the interferometer to enhance the measurement sensitivity. A 3 dB quantum enhancement has been achieved with the inclusion of squeezed light in LIGO [3, 118]. The geometry of the  $SU(1,1)$  interferometer is similar to the Mach-Zehnder interferometer, but with the linear beam splitters replaced by nonlinear ones. A true  $SU(1,1)$  interferometer can potentially reach Heisenberg-limited phase measurements (i.e., the phase noise can be inversely proportional to the number of photons rather than to the square root of the number of photons) [117, 119]. Such interferometers have potential application in phase sensitive measurement of molecules and biological samples due to the low light powers of the amplified probe and the newly generated conjugate field [90, 120, 121]. However, they are hard to build due to inconsistencies in the two nonlinear amplifiers and the resulting instabilities, the  $SU(1,1)$  interferometer has seen progress only recently [119].

The truncated  $SU(1,1)$  interferometer can avoid such issues [119, 122, 123]. It removes the need for the second nonlinear beam splitter by using two balanced homodyne detectors for the probe and conjugate fields. This device allows for the rotation of the squeezing ellipses to move through different squeezing quadratures, the joint-amplitude and joint-phase quadratures in the case of FWM. This rendition can operate with improved joint-phase or joint-amplitude detection for selective squeezed light applications, as discussed

in Ch. 7.

### 1.3.3 Spectroscopic Measurement using Squeezed Light

While squeezed light generated by FWM has many attractive features, it has its limitations. The spectral range of FWM lies within a GHz of the frequency of the atomic D1 line [98]. This severely limits applications of FWM squeezing for spectroscopy. While other sources of squeezed light have broad spectral ranges, crystals for example [124, 125], the need for supplementing the spectral range of FWM still exists.

Spectroscopic measurements involve measuring the response of light to specific resonances in a medium. There is a variety of methods of taking measurements and ranges of frequencies covered. In IR- and UV-VIS spectroscopy, broadband light of these frequencies is passed through a medium to map the resonant structure in optical absorption [126]. However, other methods which probe into the vibrational modes of molecules require the use of multi-photon processes. One example is Raman spectroscopy, where pump photons inelastically scatter with the frequency shift matching the energy of the vibrational mode of the molecules [120]. This effect requires large laser powers and has issues with large fluorescence response which can reduce the visibility of the signal [126, 127]. A solution to this is the seeded version of Raman scattering, coherent anti-Stokes Raman scattering (CARS). In this, a broadband seed field is injected along with the pump field resulting in the amplification of the seed at frequencies where a two photon resonance is formed with the pump field and a molecular transition [128, 129]. The response of this process is stronger than just Raman scattering alone. There are several other methods which use a similar principle [126, 129–132]. The effect can also be further amplified by using a cavity for the seed field [133, 134]. In all of these cases, the power needed for obtaining measurable nonlinear response is large, and that can be detrimental for power sensitive

samples [126, 127].

Another spectroscopic method is Raman two-photon absorption, described in 7.1.1 for the suppression of FWM in EIT and Raman quantum memories. By coupling the probe and Raman pump fields via a two-photon transition with the ground state and a highly excited state, the absorption of the probe field can be observed and used to make spectroscopic measurements of highly excited states by tuning of the pump frequency. This process can be extended to utilize the probe field of squeezed twin-beams, allowing for the tunable application of squeezed light for spectroscopic measurement, limited only by the spectral range of the Raman pump field. The ladder configuration has potential to probe highly excited atomic resonances, like Rydberg atoms [11, 12]. When the Raman pump and probe are coupled in a  $\Lambda$ -configuration, it may be possible to probe molecular vibrational modes. This has potential for application in enhanced imaging of biological and molecular samples [135].

## 1.4 Overview of Thesis

This thesis details experiments that look to improve upon various quantum information tools using hot rubidium vapor. Chapter 2 introduces the basic theory of multi-photon interactions of atoms with classical or non-classical electromagnetic fields. In Chapter 3 we experimentally generate FWM in conditions similar to EIT and Raman quantum memory and address the problem of FWM using Raman two-photon absorption using various coupling configurations. In Chapter 4 we discuss the FWM used to generate blue light by excitation to the  $5D_{3/2}$  state. We discuss the decay paths of excited state and how repumping can play into the FWM process. In Chapter 5 we describe the basic experimental apparatus used to generate and detect squeezed light from FWM in the proceeding Chapters. In Chapter 6, we look at the effects of using the pump and probe carrying OAM on

FWM squeezing. Specifically, how probe and conjugate beams maintain correlations even with very different spatial mode structure. In Chapter 7, we introduce polarization-based version of the truncated  $SU(1,1)$  interferometer, analyse its advantages and potential. In Chapter 8, we discuss Raman two-photon spectroscopy and the enhancement of the measurement with the use of squeezed light. We conclude with a summary of the basic outcomes and future steps in Ch. 9.

# CHAPTER 2

## Theory

### 2.1 Propagation through a medium

In this chapter, we develop the theory to describe the nonlinear processes which will be used in the experiments to follow. We begin here with the fundamental equations governing electricity and magnetism, Maxwell's equations [136].

$$\vec{\nabla} \cdot \vec{D} = \rho, \tag{2.1}$$

$$\vec{\nabla} \times \vec{E} = -\frac{\partial \vec{B}}{\partial t}, \tag{2.2}$$

$$\vec{\nabla} \cdot \vec{B} = 0, \tag{2.3}$$

$$\vec{\nabla} \times \vec{H} = \vec{J} + \frac{\partial \vec{D}}{\partial t}. \tag{2.4}$$

These equations describe the response of charges to electromagnetic fields in media and vice versa. Here,  $\vec{E}$  is the electric field,  $\vec{B}$  is the magnetic flux density,  $\vec{H}$  is the magnetic field intensity, and  $\vec{D}$  is the electric displacement field. We take the condition of being in a source-free region and so the charge density  $\rho$  and the current density  $\vec{J}$  are

zero.

The electric displacement and the magnetic field intensity describe the distribution of the fields in a medium and can be written in terms of the polarization  $\vec{P}$  and magnetization  $\vec{M}$ , respectively.

$$\vec{\nabla} \cdot \vec{D} = \varepsilon \vec{E} = \varepsilon_0 \vec{E} + \vec{P}, \quad (2.5)$$

$$\vec{\nabla} \cdot \vec{H} = \mu \vec{B} = \mu_0 \vec{B} + \vec{M}, \quad (2.6)$$

where  $\varepsilon$  and  $\varepsilon_0$  are the permittivity of a light in a medium and free space, respectively. The  $\nu$  and  $\nu_0$  are the permeability of a light in a medium and free space, respectively.

The medium we use is an alkali vapor, which is not magnetic, so the magnetization  $\vec{M}$  is zero [24, 137]. We then substitute Eqs. 2.5 and 2.6 into Maxwell's equations

$$\vec{\nabla} \cdot (\varepsilon_0 \vec{E} + \vec{P}) = 0, \quad (2.7)$$

$$\vec{\nabla} \times \vec{E} = -\frac{\partial \vec{B}}{\partial t}, \quad (2.8)$$

$$\vec{\nabla} \cdot \vec{B} = 0, \quad (2.9)$$

$$\vec{\nabla} \times \frac{\vec{B}}{\mu_0} = \frac{\partial(\varepsilon_0 \vec{E} + \vec{P})}{\partial t}. \quad (2.10)$$

Then we take the curl of Eq. 2.8 and substitute Eq. 2.10 to find

$$\vec{\nabla} \times \vec{\nabla} \times \vec{E} = -\vec{\nabla} \times \frac{\partial \vec{B}}{\partial t} = -\mu_0 \varepsilon_0 \frac{\partial^2 \vec{E}}{\partial t^2} - \mu_0 \frac{\partial^2 \vec{P}}{\partial t^2}. \quad (2.11)$$

The left side is reduced by using the identity  $\vec{\nabla} \times \vec{\nabla} \times \vec{E} = \vec{\nabla}(\vec{\nabla} \cdot \vec{E}) - \nabla^2 \vec{E}$ . This can be further reduced by using the fact that we are treating a system with no charge and by assuming isotropic polarization of the media,  $\vec{\nabla} \cdot \vec{E} = \vec{\nabla} \cdot \vec{P} = 0$ . By substituting



$\mu_0\varepsilon_0 = \frac{1}{c^2}$ , where  $c$  is the speed of light, we arrive at the wave equation

$$\nabla^2 \vec{E} - \frac{1}{c^2} \frac{\partial^2 \vec{E}}{\partial t^2} = \mu_0 \frac{\partial^2 \vec{P}}{\partial t^2}. \quad (2.12)$$

The wave equation describes the propagation of light through space. On the right hand side is the polarization response of the medium. Depending on the strength of the light-matter interaction, the polarization response takes on different forms. I address nonlinear responses of the polarization in a later section.

In its simplest form, the response is linear and the polarization is written as  $\vec{P} = \varepsilon_0(1 + \chi^{(1)})\vec{E}$ , where  $\chi^{(1)}$  is the linear susceptibility of the medium. For this case, the wave equation reduces to

$$\nabla^2 \vec{E} - \frac{1}{v^2} \frac{\partial^2 \vec{E}}{\partial t^2} = 0 \quad (2.13)$$

where  $v$  is the speed of light in the medium.

Here, the linear polarization response was combined with the electric field on the left-hand side. The solution to the wave equation for  $\hat{x}$ -polarized light is [24]

$$\vec{E}(z, t) = \frac{1}{2} E_0(z, t) \hat{x} e^{i(kz - \omega t)} + c.c., \quad (2.14)$$

where  $c.c.$  is complex conjugate. This describes the propagation of a plane wave in free space with positive and negative frequency components

$$\hat{E}^{(+)} = E_0 \hat{x} e^{i(kz - \omega t)}, \quad (2.15)$$

$$\hat{E}^{(-)} = E_0 \hat{x} e^{-i(kz - \omega t)}. \quad (2.16)$$

## 2.2 Semi-Classical Approach to Light-Atom Interactions

In this section, we develop the tools needed to describe light-atom interactions. We begin with a simple example of a two-level system with levels  $|a\rangle$  and  $|b\rangle$  separated by energy  $\hbar\omega_{ab} = \hbar(\omega_a - \omega_b)$ , shown in Fig. 2.1. The light-atom interaction is given by the minimal coupling Hamiltonian [23, 24]

$$\hat{H} = \frac{1}{2m}[\vec{p} + e\vec{A}]^2 - e\phi + V_c(\vec{r}), \quad (2.17)$$

where  $\vec{A}$  and  $\phi$  are the electrostatic vector and scalar potentials for the external fields, respectively. The contribution from the atom is given by the momentum  $\vec{p}$  and the Coulomb potential  $V_c(\vec{r})$ . We are working in the radiation gauge, making  $\phi = 0$  and  $\vec{\nabla} \cdot \vec{A} = 0$ , leaving us with

$$\hat{H} = \frac{1}{2m}p^2 + V_c(\vec{r}) + \frac{e}{m}\vec{A} \cdot \vec{p} + \frac{[e\vec{A}]^2}{2m}, \quad (2.18)$$

where the first two terms describe the Hamiltonian of an atom,  $\hat{H}_0$ . The second two terms represent the light-atom interaction for the linear and quadratic responses, where the quadratic term is generally neglected [23]. In addition to this, we assume that the external field has a wavelength much larger than the size of the atom  $\lambda \gg r$ . As a result, the applied field is uniform across the atom for any given instance in time and allows us to make a comparison between the vector potential and the electric field  $\vec{A} \cdot \vec{p} \approx \vec{E} \cdot \vec{r}$  [23] and leaves us with

$$\hat{H} = \hat{H}_0 - e\vec{r} \cdot \vec{E} \quad (2.19)$$

In this thesis, we consider an interaction weak enough as to not effect the atomic energy levels. By doing this, we can employ time-dependent perturbation theory and

treat just the interaction term [23, 24, 137]. We use the Schrodinger picture to evolve the state in time

$$|\psi(t)\rangle = \sum_k C_k(t)e^{-E_k t/\hbar}|k\rangle, \quad (2.20)$$

where the coefficient  $C_k(t)$  represents the population of the level  $|k\rangle$ , and  $|\psi\rangle$  is the state of the system. By plugging this into the time-dependent Schrodinger equation, we can find the coefficients  $C_k(t)$ , and thus gain information on the evolution of the populations of the levels

$$i\hbar \frac{\partial |\psi\rangle}{\partial t} = (\hat{H}_0 + \hat{H}_I)|\psi\rangle, \quad (2.21)$$

where  $\hat{H}_I = -e\vec{r} \cdot \vec{E}$  is the interaction term. By plugging Eq. 2.20 into Eq. 2.21 and solving for the coefficients  $C_1(t)$ , we arrive at

$$\dot{C}_2(t) = -\frac{i}{\hbar} \sum_1 C_1(t)e^{i\omega_{21}} \langle 2|\hat{H}_I|1\rangle, \quad (2.22)$$

where  $\omega_{21} = \frac{E_2 - E_1}{\hbar}$  is the transition frequency and  $\langle 2|\hat{H}_I|1\rangle$  is the dipole transition strength.

### 2.2.1 Selection Rules

We now look at the effects of parity of states on the transition probability. Rubidium is a hydrogen like-atom, so we define our states in terms of wave functions resembling those of the hydrogen atom

$$|k\rangle = |n, l, m\rangle, \quad (2.23)$$

where  $n$  is the principle quantum number,  $l$  is the angular momentum quantum number, and  $m$  is magnetic quantum number. When we consider the transition strength

$\langle 2|\hat{H}_I|1\rangle$  in Eq. 2.22, we know there are only certain transitions which would be allowed. The transition is defined by

$$\langle 2|\hat{H}_I|1\rangle = \langle 2|\vec{E} \cdot \vec{r}|1\rangle = \langle 2|eE_0(t)\hat{e}_p \cdot \vec{r}|1\rangle, \quad (2.24)$$

where the electric field has been split into its polarization  $\hat{e}_p$  and time dependent amplitude. The main contribution that determines if the interaction is feasible is the parity of the states and the polarization of the light

$$\wp_{lk} = \langle n_2, l_2, m_2|\hat{e}_p \cdot \vec{r}|n_1, l_1, m_1\rangle. \quad (2.25)$$

where  $\wp_{21}$  is the transition dipole moment.

In general, the polarization of the light which we work with is in the x-y plane  $\hat{e}_p = \hat{e}_x$ . For this, the transition dipole moment is non-zero only if the two states have opposite parity. The allowed transitions are then [138]

$$\Delta l = \pm 1, \quad (2.26)$$

$$\Delta m = 0, \pm 1. \quad (2.27)$$

Here, we take the opportunity to simplify the Hamiltonian and consider the interaction term in Eq. 2.24. The interaction is broken into the positive and negative frequency contributions of each operator, the electric field and dipole operators

$$\hat{E} = \frac{1}{2}E_0\hat{x}[e^{i\omega t} + e^{-i\omega t}] = \hat{E}^{(+)} + \hat{E}^{(-)}, \quad (2.28)$$

$$\hat{d} = -e(\wp_{21}|2\rangle\langle 1| + \wp_{12}|1\rangle\langle 2|) = \hat{d}^{(+)} + \hat{d}^{(-)}. \quad (2.29)$$

where the time dependence of the dipole operators is  $\langle \psi(t)|\hat{d}^{(+)}|\psi(t)\rangle = \langle \psi(t)|\hat{d}^{(+)}|\psi(t)\rangle^* =$

$e^{i\omega_{12}}$ . Looking again at the interaction in Eq. 2.24

$$\hat{E} \cdot \hat{d} = [\hat{E}^{(+)} + \hat{E}^{(-)}] \cdot [\hat{d}^{(+)} + \hat{d}^{(-)}], \quad (2.30)$$

we see that there are exponentials with frequency sums and differences, where the contributions from the frequency sum terms will oscillate too fast and average out in time. This is the rotating wave approximation and so we remove the frequency sum terms and keep the difference terms. This is allowed so long as the frequency difference  $\Delta = \omega - \omega_{21} \ll \omega + \omega_{21}$  [24]. Using the rotating wave approximation and the the selection rules, we now write the simplified interaction Hamiltonian

$$\hat{H}_I = \hat{E}^{(+)} \cdot \hat{d}^{(-)} + \hat{E}^{(-)} \cdot \hat{d}^{(+)}. \quad (2.31)$$

## 2.2.2 Density Matrix Formalism

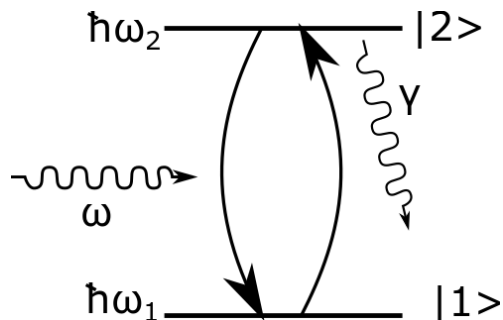


FIG. 2.1: Two-level diagram with incoming photon of energy  $\omega$ .

It is useful to switch to the density matrix formalism over the wave function approach to handle relaxation processes. It allows us to work with statistical mixtures of states and deal with things like spontaneous emission. We follow the formalism established in [24, 137]. The density matrix for the pure state of the two level system, shown in

Fig. 2.1 is defined as

$$\begin{aligned}
\hat{\rho} &= |\psi\rangle\langle\psi|, \\
&= \begin{pmatrix} |C_1|^2 & C_1 C_2^* \\ C_2 C_1^* & |C_2|^2 \end{pmatrix}, \\
&= \begin{pmatrix} \rho_{11} & \rho_{12} \\ \rho_{21} & \rho_{22} \end{pmatrix}
\end{aligned} \tag{2.32}$$

where the the diagonal terms correspond to the populations of the states,  $|k\rangle$  and  $|\ell\rangle$ . The off-diagonals represent the coherences and give information on the dispersion in the system. The coefficients are defined in Eq. 2.22. The evolution of the density matrix in time is given by

$$\begin{aligned}
\frac{d\hat{\rho}}{dt} &= \frac{d}{dt} |\psi\rangle\langle\psi|, \\
&= \left[ \frac{d}{dt} |\psi\rangle \right] \langle\psi| + |\psi\rangle \left[ \frac{d}{dt} \langle\psi| \right],
\end{aligned} \tag{2.33}$$

and by using the time-dependent Schrodinger equation, we get

$$\begin{aligned}
\frac{d\hat{\rho}}{dt} &= -\frac{i}{\hbar} [\hat{H} |\psi\rangle\langle\psi| - |\psi\rangle\langle\psi| \hat{H}], \\
&= -\frac{i}{\hbar} [\hat{H}, \hat{\rho}].
\end{aligned} \tag{2.34}$$

Our Hamiltonian from Eq. 2.19 can be written in matrix form as

$$\begin{aligned}
\hat{H} &= (|1\rangle\langle 1| + |2\rangle\langle 2|)\hat{H}(|1\rangle\langle 1| + |2\rangle\langle 2|), \\
&= \hbar\omega_1|1\rangle\langle 1| + \hbar\omega_2|2\rangle\langle 2| \\
&+ \frac{1}{2}(eE_0\wp_{21}e^{i\omega t}|1\rangle\langle 2| + eE_0\wp_{21}e^{-i\omega t}|2\rangle\langle 1|), \\
&= \begin{pmatrix} 0 & \frac{eE_0\wp_{21}}{2}e^{i\omega t} \\ \frac{eE_0\wp_{21}}{2}e^{-i\omega t} & \hbar\omega_{21} \end{pmatrix},
\end{aligned} \tag{2.35}$$

where we have applied the selection rules and adjusted the energy of the states relative to the ground state  $|1\rangle$ . The energy of the excited state  $|2\rangle$  is  $\omega_{21} = \omega_2 - \omega_1$ . From here, we also substitute in the Rabi frequency

$$\Omega = \frac{e|E_0|\wp_{21}}{\hbar}. \tag{2.36}$$

To remove the time dependence in the Hamiltonian, we transform into the rotating frame of the laser field. This is by using a unitary transformation on the state of the system

$$|\tilde{\psi}\rangle = \hat{U}^\dagger|\psi\rangle, \tag{2.37}$$

where  $\hat{U} = e^{i\frac{\hat{H}_0 t}{\hbar}} = e^{i\omega t|1\rangle\langle 1|}$  is the unitary operator and  $\tilde{\psi}$  denotes the wave function in the rotating wave frame. By inserting Eq. 2.37 into the Schrodinger equation Eq. 2.21, we can

find the Hamiltonian in the rotating frame [24]

$$\begin{aligned}
i\hbar \frac{\partial}{\partial t} |\tilde{\psi}\rangle &= i\hbar \frac{\partial}{\partial t} (\hat{U}^\dagger |\psi\rangle) = \tilde{H} |\tilde{\psi}\rangle, \\
&= i\hbar \frac{\partial}{\partial t} \hat{U}^\dagger \hat{U} + \hat{U}^\dagger \hat{H} \hat{U} |\tilde{\psi}\rangle, \\
&= \begin{pmatrix} 0 & \frac{\hbar}{2}\Omega \\ \frac{\hbar}{2}\Omega^* & \hbar\Delta \end{pmatrix} |\tilde{\psi}\rangle,
\end{aligned} \tag{2.38}$$

where we see that the time dependence has been removed,  $\Delta = \omega_{12} - \omega n$  and  $\Omega = \frac{e|E_0|\rho_{21}}{\hbar}$  is the slowly varying amplitude. Now, to find the equations of motion for our system we insert Eqs. 2.38 and 2.32 into Eq. 2.34

$$\begin{pmatrix} \dot{\rho}_{11} & \dot{\rho}_{12} \\ \dot{\rho}_{21} & \dot{\rho}_{22} \end{pmatrix} = \begin{pmatrix} i\frac{\Omega}{2}[\rho_{12} - \rho_{21}] & i\frac{\Omega}{2}[\rho_{11} - \rho_{22}] - i\Delta \cdot \rho_{12} \\ i\frac{\Omega}{2}[\rho_{22} - \rho_{11}] + i\Delta \cdot \rho_{21} & i\frac{\Omega}{2}[\rho_{21} - \rho_{12}]. \end{pmatrix} \tag{2.39}$$

This system of equations are the same as those produced from the wave function approach used earlier to find Eq. 2.22. However, we have the ability here to account for spontaneous emission and collision processes in the atoms, which cause de-excitations and decoherence. We introduce these relaxation processes as a decay rate from the excited state population  $\rho_{22}$  to the ground state  $\rho_{11}$  and as a decoherence between the states and describe them as a population decay  $\gamma$  and decoherence rate  $\gamma_{12}$

$$\begin{pmatrix} \dot{\rho}_{11} & \dot{\rho}_{12} \\ \dot{\rho}_{21} & \dot{\rho}_{22} \end{pmatrix} = \begin{pmatrix} i\frac{\Omega}{2}[\rho_{12} - \rho_{21}] + \gamma\rho_{22} & i\frac{\Omega}{2}[\rho_{11} - \rho_{22}] - (\gamma_{12} + i\Delta)\rho_{12} \\ i\frac{\Omega}{2}[\rho_{22} - \rho_{11}] + (\gamma_{12} - i\Delta)\rho_{21} & i\frac{\Omega}{2}[\rho_{21} - \rho_{12}] - \gamma\rho_{11}. \end{pmatrix} \tag{2.40}$$

Using these equations, we can find the populations of the two states and the absorption of the optical field. By using the density matrix approach in combination with the wave equation, we can also find the propagation dynamics in the system. This is done by relating



the polarization in Eq. 2.12 to the ensemble of atoms. The polarization can be defined as

$$P = \varepsilon_0 \chi \vec{E} = \frac{N}{V} \langle \psi | \hat{d} | \psi \rangle, \quad (2.41)$$

where  $N$  is the number of atoms in the ensemble and  $V$  is the volume. The transition strength is substituted by the off diagonal components of the density matrix

$$P = \frac{N}{V} \wp_{lk} \rho_{lk}, \quad (2.42)$$

and the susceptibility is defined as [23, 24]

$$\chi = \frac{2\wp_{kl}^2}{\hbar \varepsilon_0} \frac{\rho_{kl}}{\Omega}. \quad (2.43)$$

This shows that the density matrix off diagonal terms are related to the polarization, and this susceptibility can be used to find both the absorption and dispersion in the medium. We use this approach to light-atom interactions to solve more complicated systems in the next section.

## 2.3 Coherent Nonlinear Processes

In this section, we derive coherent nonlinear effects like EIT and Raman absorption, where a pump field is used to tune the dispersion of the atomic medium for the probe field [28, 31, 36, 139, 140]. By doing this, we can control the speed of light and absorption in the medium using the pump, enabling quantum memories and sensing applications [5, 28, 36, 122, 141]

We begin with a three-level system in a  $\Lambda$ -configuration with two resonant fields, shown by Fig. 2.2. We start by defining the Hamiltonian of the system, where we have

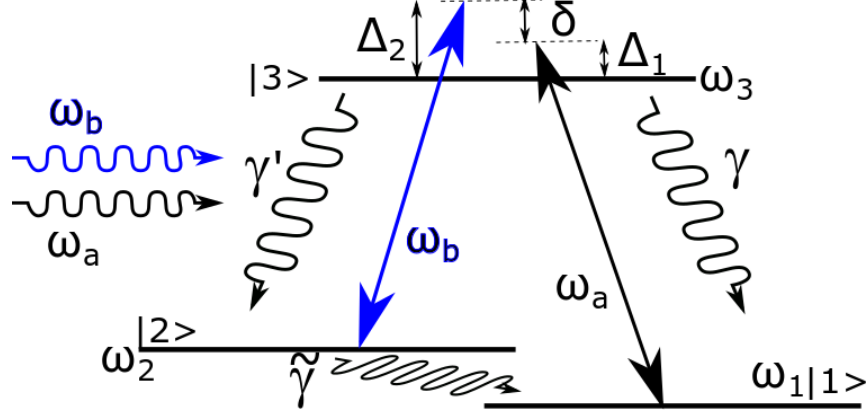


FIG. 2.2: Three-level diagram with incoming photons of energy  $\omega_a$  and  $\omega_b$ . The decay rates are given by  $\gamma'$ ,  $\gamma$ , and  $\tilde{\gamma}$

already made the rotating wave approximation [24, 142, 143]

$$\hat{H} = \begin{pmatrix} \hbar\omega_1 & 0 & \frac{\hbar}{2}\Omega_a e^{i\omega_a t} \\ 0 & \hbar\omega_2 & \frac{\hbar}{2}\Omega_b e^{i\omega_b t} \\ \frac{\hbar}{2}\Omega_a^* e^{-i\omega_a t} & \frac{\hbar}{2}\Omega_b^* e^{-i\omega_b t} & \hbar\omega_3 \end{pmatrix}, \quad (2.44)$$

where  $\Omega_{a,b} = e|E_{a,b}|/\hbar$  are the Rabi frequencies for the two resonances. We define our energy levels relative to our ground state  $|1\rangle$

$$\Delta_{1,2} = \omega_{a,b} - (\omega_{1,2} - \omega_3), \quad (2.45)$$

$$\delta = \Delta_1 - \Delta_2 = (\omega_a - \omega_b) - \omega_{12}, \quad (2.46)$$

where  $\Delta_{1,2}$  are the single-photon detunings of the fields relative to the respective transitions  $\omega_{13}$  and  $\omega_{23}$ . The two-photon detuning of the two fields is  $\delta$ . The Hamiltonian is then given by

$$\hat{H} = \begin{pmatrix} 0 & 0 & \frac{\hbar}{2}\Omega_a e^{i\omega_a t} \\ 0 & \hbar\Delta_1 & \frac{\hbar}{2}\Omega_b e^{i\omega_b t} \\ \frac{\hbar}{2}\Omega_a^* e^{-i\omega_a t} & \frac{\hbar}{2}\Omega_b^* e^{-i\omega_b t} & \hbar\Delta_2 \end{pmatrix}. \quad (2.47)$$

After shifting the energy levels, we change into the rotating frame using the unitary operator

$$\hat{U} = e^{i(\omega_a|3\rangle\langle 3| + (\omega_a - \omega_b)|2\rangle\langle 2|)t}, \quad (2.48)$$

Transforming the Hamiltonian to

$$\tilde{H} = \begin{pmatrix} 0 & 0 & \frac{\hbar}{2}\Omega_a \\ 0 & \hbar\delta & \frac{\hbar}{2}\Omega_b \\ \frac{\hbar}{2}\Omega_a^* & \frac{\hbar}{2}\Omega_b^* & \hbar(\Delta_2 + \delta) \end{pmatrix}. \quad (2.49)$$

We now find the equations of motion using Eq. 2.34

$$\dot{\rho}_{11} = i(\rho_{31} - \rho_{13})\Omega_a + \tilde{\gamma}\rho_{22} + \gamma'\rho_{33}, \quad (2.50)$$

$$\dot{\rho}_{22} = \frac{i}{2}\Omega_b(\rho_{32} - \rho_{23}) + \gamma\rho_{33} - \tilde{\gamma}\rho_{22}, \quad (2.51)$$

$$\dot{\rho}_{21} = \frac{i}{2}(\Omega_a\rho_{23} - \Omega_b\rho_{31}) - (\gamma_{12} - i\delta)\rho_{21}, \quad (2.52)$$

$$\dot{\rho}_{31} = \frac{i}{2}\Omega_a(\rho_{11} - \rho_{33}) - \frac{i}{2}\Omega_b\rho_{21} - (\gamma_{13} - i(\Delta + \delta))\rho_{31}, \quad (2.53)$$

$$\dot{\rho}_{32} = \frac{i}{2}\Omega_b(\rho_{22} - \rho_{33}) - \frac{i}{2}\Omega_a\rho_{12} + (\gamma_{23} - i\Delta)\rho_{32}, \quad (2.54)$$

$$1 = \rho_{33} + \rho_{22} + \rho_{11}, \quad (2.55)$$

where we have taken  $\Delta = \Delta_2$  and included the population decays  $\gamma, \gamma'$ , and  $\tilde{\gamma}$  and decoherence rates  $\gamma_{13}, \gamma_{23}$ , and  $\gamma_{12}$ , shown in Fig. 2.2. The decoherence rates in our system for Rb atoms are  $\gamma_{13} \approx 2\pi \cdot 6MHz$  and  $\gamma_{12} \approx 0kHz$  [31, 144–146]. However, in the case of dephasing and population decays from collisions,  $\gamma_{12} \approx 3kHz$  and grows with effects from the pump laser power as  $\gamma_s = \gamma_{12} + \gamma_{13}|\Omega_2|^2/\Delta_{HF}^2$ .

In general, we deal with a strong pumping field  $E_b$  and a weak signal field  $E_a$ . This allows us to make the assumption that  $\Omega_b \gg \Omega_a, \gamma, \delta$  and results in some interesting

properties. Due to the strong pumping from a state by a pump  $\Omega_b$ , the atomic population quickly shifts to the  $|1\rangle$  state and is trapped there. So, for the first-order effect in  $\Omega_a$ ,  $\rho_{11} \approx 1$  and  $\rho_{22} = \rho_{33} \approx 0$ . In addition to this, the coherence between the empty levels is also then zero,  $\rho_{23} = 0$ . In the steady state, the equations of motion are now easily solved

$$\rho_{21} = -\frac{\Omega_a \Omega_b}{4\Gamma_{12}\Gamma_{13} + |\Omega_b|^2}, \quad (2.56)$$

$$\rho_{31} = i\frac{2\Omega_a\Gamma_{12}}{4\Gamma_{12}\Gamma_{13} + |\Omega_b|^2}, \quad (2.57)$$

where  $\Gamma_{12} = \gamma_{12} - i\delta$  and  $\Gamma_{13} = \gamma_{13} - i(\Delta + \delta)$ . Here,  $\rho_{21}$  is the coherence between the ground states established by the strong pumping field  $E_b$ , and  $\rho_{31}$  is the optical coherence at the signal frequency  $\omega_b$ .

The susceptibility  $\chi$  of the probe field is related to the coherence  $\rho_{31}$  by Eq. 2.43

$$\chi_a = i\frac{\rho_{13}^2(\gamma_{13} + i(\Delta + \delta))}{\hbar\varepsilon_0(\gamma_{13}^2 + (\Delta + \delta)^2)}\left[1 - \frac{|\Omega_b|^2/4}{(\gamma_{12} - i\delta)(\gamma_{13} - i(\Delta + \delta)) + |\Omega_b|^2/4}\right], \quad (2.58)$$

Using this, we can find the absorption and dispersion of the probe field, where the first term is the linear response for the field and the second term is from the two-photon process. The real part is the dispersion in the medium and the imaginary part is the absorption. We now analyze the atom field two-photon interaction for two cases, far-detuned and resonant.

### 2.3.1 Far-Detuned Raman Resonance

In the event that the two optical fields are tuned far from the atomic resonances, ( $|\Delta_1|, |\Delta_2| \gg \Omega_{a,b}, \delta, \gamma_{ij}$ ), it is possible to still observe absorption through the two-photon interaction with the hyper-fine split ground states. Under these conditions, the suscepti-

bility in Eq. 2.58 reduces to

$$\chi_a = -i \frac{\wp_{13}^2}{\hbar \varepsilon_0} \frac{|\Omega_b|^2 / (4\Delta^2)}{\left(\frac{\gamma_{12}}{2} + \frac{\gamma_{13}}{2} \frac{|\Omega_b|^2}{4\Delta^2}\right) - i\left(\delta - \frac{|\Omega_b|^2}{\Delta}\right)}. \quad (2.59)$$

The imaginary part of the susceptibility is proportional to the absorption. Eq. 2.59 shows the structure of the absorption resulting from the two-photon interaction of the pump and signal field. This resonance is interesting for a few reasons, (i) the absorption occurs far off resonance, (ii) it arises from the coupling between two states which are normally non-interacting due to selection rules, and (iii) an absorption profile with a width significantly smaller than the radiative decay rate of the optical excited state. This width is proportional to the dephasing rate  $\tilde{\gamma}$  of the hyper-fine split states. The denominator in Eq. 2.59

$$\gamma_{eff} = \frac{\gamma_{12}}{2} + \frac{\gamma_{13}}{2} \frac{|\Omega_b|^2}{4\Delta^2} \quad (2.60)$$

is the width of this resonance and  $\gamma_{12} \ll \gamma_{13}, \gamma_{23}$  and  $\gamma_{13} \gg \frac{\gamma_{13}}{2} \frac{|\Omega_b|^2}{4\Delta^2}$  for a three-level  $\Lambda$ -system.

We now look at the absorption of a single photon resonant with the atomic transition. In this case, the absorption is given by

$$\alpha = \text{Im}\{\chi_a\} = \frac{\wp_{13}^2}{\hbar \varepsilon_0} \frac{\gamma_{13}}{\gamma_{13}^2 + \Delta^2}. \quad (2.61)$$

Here, the absorption width is  $\gamma_{13}$  which is much larger than the absorption width in the two-photon resonance, as shown in Fig. 2.3. The narrow feature is useful to combat broadening effects from power and temperature and can be used for increased precision in measurement [11, 12]. However, as we tune away from the atomic resonance, the response becomes increasingly weaker and higher pump powers are necessary.

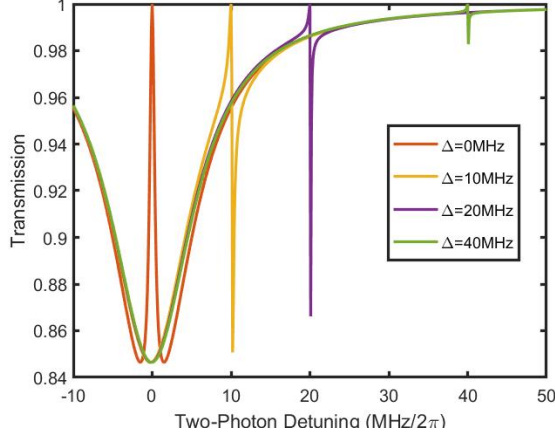


FIG. 2.3: Plot of absorption of probe field in Eq. 2.58 as a function of the two-photon detuning for different values pump detuning  $\Delta$ , where  $\gamma_{12} = 0$  and  $\gamma_{13}$  is set to  $2\pi \cdot 6MHz$ .

### 2.3.2 Electromagnetically Induced Transparency

Next, we consider the case where the pump is resonant with the  $2 \rightarrow 3$  transition,  $\Delta_2 = 0$  and so  $\delta = \Delta_1$ . Like before, we look at the susceptibility of the probe field.

$$\chi_a = i \frac{\wp_{13}^2}{\hbar \epsilon_0 (\gamma_{13} - i\Delta)} \left( \frac{(\gamma_{12} - i\Delta)}{\gamma_{12} - i\Delta} + \frac{|\Omega_b|^2}{(\gamma_{13} - i\Delta)} \right). \quad (2.62)$$

There are a couple of take aways here. The absorption profile  $\Im\{\chi_a\}$  has a region where the absorption for the probe field is suppressed, shown in Fig. 2.3. This begins to develop as probe detuning  $\Delta$  approaches zero. For  $\Delta = 0$  we see Eq. 2.62 reduce to

$$\Im\{\chi_a\} = \frac{\wp_{13}^2}{\hbar \epsilon_0} \frac{\gamma_{12}}{|\Omega_b|^2}. \quad (2.63)$$

where  $\gamma_{12} \ll \gamma_{13}, \Omega_b$ . This points to the absorption going to zero for the two-photon resonance. This is electromagnetically induced transparency (EIT), where we have lossless propagation of light through this medium [31, 33]. Additionally, this transparency window is very narrow ( $\propto \gamma_{12}$ ). Similar to the Raman resonance, it can be used to overcome broadening effects and gain precision.

We can also look at the ground state coherence  $\rho_{12}$  from Eq. 2.57 and find that it is non-vanishing

$$\rho_{12} = -\frac{\Omega_a}{\Omega_b}, \quad (2.64)$$

defined by the dark state given by

$$|D\rangle = \frac{1}{\sqrt{|\Omega_a|^2 + |\Omega_b|^2}}(\Omega_a|1\rangle - \Omega_b|2\rangle). \quad (2.65)$$

The interaction of this state with the fields is given by

$$\begin{aligned} \hat{H}_I|D\rangle &= \frac{1}{\sqrt{|\Omega_a|^2 + |\Omega_b|^2}}(-\Omega_a|1\rangle\langle 3| - \Omega_b|2\rangle\langle 3| + c.c.)(\Omega_a|1\rangle - \Omega_b|2\rangle) \\ &= 0. \end{aligned} \quad (2.66)$$

where the dark state is unaffected by the fields and avoids decoherence. By pumping all the atoms into this dark state using the pump and probe, we can write the information carried by the signal field onto the atomic spin state [147]. Then by turning off the pump, they are trapped there until second retrieval pump pulse is sent. Utilizing the light atom interactions in this manner is a path towards quantum memories [145, 148]. This ground state coherence has potential as a storage state [28, 31].

Raman absorption and EIT are coherent nonlinear processes which can be used for this purpose, but the quantum memory which they are used to generate are prone to other decoherence effects [43, 45, 149]. Collisions are a major contributor to decoherence, but can be overcome by using a buffer gas or cold atomic systems [149, 150]. It is other nonlinear effects, like FWM which add noise into the system and are not so easily removed [45, 54–56].

## 2.4 Four-Wave Mixing

To introduce FWM, we begin by returning to wave equation Eq. 2.12 where we consider the polarization response of the medium more thoroughly. Following the work in [20, 23, 24], we take into account the nonlinear contributions of the polarization

$$\vec{P} = \varepsilon_0(1 + \chi^{(1)}\vec{E} + \chi^{(2)}\vec{E}^2 + \chi^{(3)}\vec{E}^3 + \dots). \quad (2.67)$$

where each susceptibility term  $\chi^{(n)}$  is an increasing rank tensor.

Depending on the symmetries of the system we are working with, the higher order contributions come from even or odd  $\chi$  terms. For example, we can only observe  $\chi^{(2)}$  responses in crystals or fibers, since it is possible to have non-centrosymmetric sites. FWM exists in the  $\chi^{(3)}$  polarization response and has been realized in crystals, fibers, and vapors where medium had rotational symmetry [20]. The polarization response is given by

$$\vec{P}^{(3)} = \varepsilon_0\chi^{(3)}(\vec{E}_a + \vec{E}_b)^3, \quad (2.68)$$

where the electric fields of the pump ( $E_b$ ) and the probe ( $E_a$ ) have been substituted in. The polarization response here many terms, however, the number of terms reduce substantially based on the strength of their contributions depending on the proximity to atomic resonances and strengths of the fields. When considering the three-level  $\Lambda$ -system which is used regularly in this thesis, the only term which contributes is

$$\begin{aligned} \vec{P}_p^{(3)} &= \varepsilon_0\chi^{(3)}E_a^*E_b^2e^{-i[(\vec{k}_a-2\vec{k}_b)z-(\omega_a-2\omega_b)t]}, \\ &= \varepsilon_0\chi^{(3)}E_c^*e^{i[\vec{k}_cz-\omega_ct]} \end{aligned} \quad (2.69)$$

where  $\chi^{(3)}E_a^*E_b^2$  is the strength of the newly generated field ( $E_c$ ) and the phase matching



conditions

$$\Delta\omega + \omega_c = 2\omega_b - \omega_a, \quad (2.70)$$

$$\Delta\vec{k} + \vec{k}_c = 2\vec{k}_b - \vec{k}_a, \quad (2.71)$$

determine the wave vector  $\vec{k}_c$  and frequency  $\omega_c$  of the new field.  $\Delta\vec{k}$  and  $\Delta\omega$  are the phase mismatch which would weaken the FWM resonance, depicted in Fig. 2.4. The wave vector contribution is generally tied to the dispersion of the medium and so the momentum phase matching conditions can be supplemented, to a small degree, by shifting frequencies rather than the alignment as demonstrated in Ch. 5. This is written as [24]

$$2\frac{n(\omega_b) \cdot \omega_b}{c} \cos(\theta_b) - \frac{n(\omega_a) \cdot \omega_a}{c} \cos(\theta_a) = \frac{n(\omega_c) \cdot \omega_c}{c} \cos(\theta_c), \quad (2.72)$$

where  $\theta_i$  are the angles of propagation relative to the propagation axis. Moving forward, we take both  $\Delta\vec{k}$  and  $\Delta\omega$  to be zero. We also introduce the polarization response of the new conjugate field

$$\vec{P}_c^{(3)} = \varepsilon_0 \chi^{(3)} E_p^* e^{i[\vec{k}_p z - \omega t]}. \quad (2.73)$$

The FWM process generates a new conjugate field as a result of the nonlinear response of the medium. To better understand the coupling of this field in the system, we want to observe how this new field and the original input field evolve as they move through the Rb vapor.

We turn our attention back to the wave equation Eq. 2.12 to monitor the propagation. It is generally a good assumption for the phase and the amplitude of an optical field to vary little within an optical wavelength. This is the slow varying amplitude and phase approximation and a plane wave in the z-direction. Allowing us to make the following

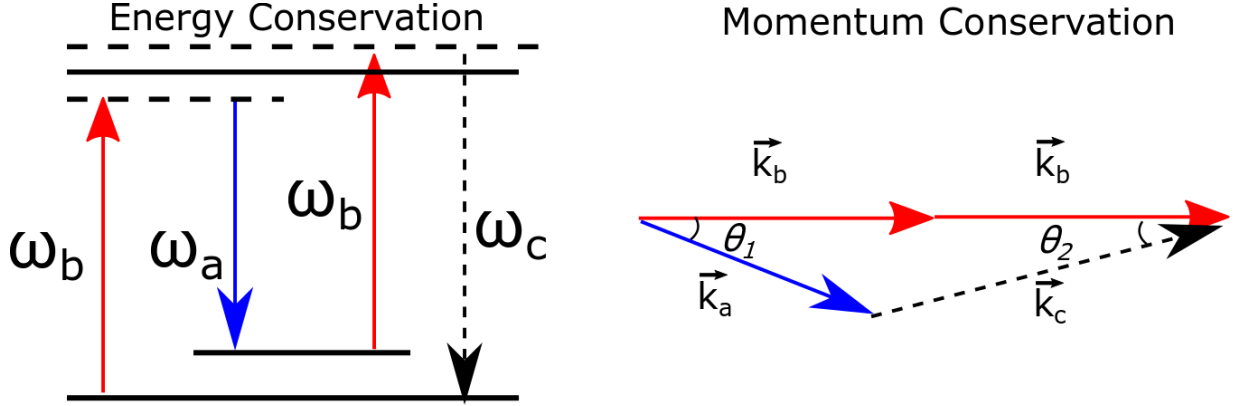


FIG. 2.4: (a) shows the energy conservation of the FWM process where two pump photons are absorbed while a probe photon is added and a new conjugate photon is generated with energy to match the difference. The solid lines represent real states, while dashed are virtual states marking multi-photon resonances. (b) shows the momentum conservation.

simplifications [23, 24]

$$\left| \frac{\partial E}{\partial t} \right| \ll \omega E, \quad (2.74)$$

$$\left| \frac{\partial E}{\partial z} \right| \ll k E, \quad (2.75)$$

$$\left| \frac{\partial P}{\partial t} \right| \ll \omega P, \quad (2.76)$$

$$\nabla^2 E \rightarrow \frac{\partial^2}{\partial z^2} E. \quad (2.77)$$

The wave equation is now

$$\frac{\partial E_0}{\partial z} = -\frac{k}{2\varepsilon_0} \text{Im}\{P\}, \quad (2.78)$$

where we have taken the steady state form as the field propagates through the medium. Considering that the pumping field is strong, we assume it does not change with this interaction and maintains its energy, making the undepleted pump approximation. Now, the evolution of the probe ( $E_a$ ) and conjugate ( $E_c$ ) are found by plugging the polarization

responses of the fields Eq. 2.69 and Eq. 2.73 into Eq. 2.78

$$\frac{\partial E_a}{\partial z} = \frac{ik_c}{2\varepsilon_0} \chi^{(3)} E_c'^*, \quad (2.79)$$

$$\frac{\partial E_c}{\partial z} = \frac{ik_a}{2\varepsilon_0} \chi^{(3)} E_a'^*, \quad (2.80)$$

where the exponential has been absorbed into the field  $E_i e^{i\vec{k}_p z} \rightarrow E_i'$ . The solutions to this are [23, 143].

$$E_a(L) = \cosh(|\eta_a|L) E_a'^*(0), \quad (2.81)$$

$$E_c(L) = -i \frac{\eta_a}{|\eta_a|} \sinh(|\eta_a|L) E_a'^*(0), \quad (2.82)$$

where  $\eta_{a,c} = \frac{k_{a,c}}{2\varepsilon_0} \chi^{(3)}$  and we have used the initial conditions where the seeded probe field  $E_a(0)$  is the input field strength and the new conjugate  $E_a(0)$  is initially zero. These equations give the evolution of the fields through the medium. Using this, we can see the effects of FWM in different systems, both beneficial and detrimental. A detailed derivation of the susceptibility tensor can be found in [151].

### 2.4.1 Frequency Conversion via FWM

In the last section, we discussed how FWM can lead to the generation of a new field with a frequency that is close to those of the pump and probe. Here, we point another application of the resonant coupling of FWM as a means to convert a signal from one frequency to another frequency [58–60]. This is a useful tool for switching between different tasks in a communication link [44]. For example, rubidium based quantum memories operate near 800 nm while optical fiber communications are most efficient at 1550 nm wavelengths [152]. An efficient transduction method is necessary to avoid decoherence in the link [153].

In this section, we will look at the generation of the conjugate field far detuned from the input pump and probe fields. In this case, the field is generated by the coupling of probe and pump optical fields in a ladder configuration to a second excited state of the Rb atom. The resulting fluorescence from the upper excited state via alternate levels seeds the FWM process for the generation of new fields, shown in Fig. 2.6. In this case, there is no seed probe field.

We begin with Eq. 2.68 where we look at the polarization response of a medium and consider the other possible combinations of the fields [20]. We introduce a place holder term for potential new fields to be generated. So Eq. 2.68 now looks like

$$\vec{P}^{(3)} = \varepsilon_0 \chi^{(3)} (\vec{E}_a + \vec{E}_b + \vec{E}_c + \vec{E}_d)^3, \quad (2.83)$$

where  $E_c$  and  $E_d$  are place holders for the newly generated fields. Some of the possible configurations are shown in Fig. 2.5. However, we consider the four-photon resonance where there is a two-photon absorption with a simultaneous two-photon emission, shown by Fig. 2.5 (a). We write the polarization response here [20]

$$\begin{aligned} \vec{P}^{(3)} &= \varepsilon_0 \chi^{(3)} \vec{E}_a \vec{E}_b \vec{E}_c^* e^{i(\omega_a + \omega_b - \omega_c)} + \varepsilon_0 \chi^{(3)} \vec{E}_a \vec{E}_b \vec{E}_d^* e^{i(\omega_a + \omega_b - \omega_d)} + c.c., \\ &= \varepsilon_0 \chi^{(3)} (\vec{E}_c^* e^{i\omega_c} + \vec{E}_d^* e^{i\omega_d} + c.c.), \end{aligned} \quad (2.84)$$

where  $\omega_a + \omega_b - \omega_c - \omega_d = 0$  and  $\vec{k}_a + \vec{k}_b - \vec{k}_c - \vec{k}_d = 0$  are the phase matching conditions for the frequency which correspond to energy conservation. In this case, we can see that  $\omega_c$  and  $\omega_d$  can be any value so long as  $\omega_c + \omega_d = \omega_a + \omega_b$ .

The new fields  $E_c$  and  $E_d$  can have a large range of frequencies, but the atomic resonances mediate and enhance the nonlinearity, thus limiting the range of frequencies at which the new fields can be generated. Specifically in the case of Fig. 2.6, two input fields

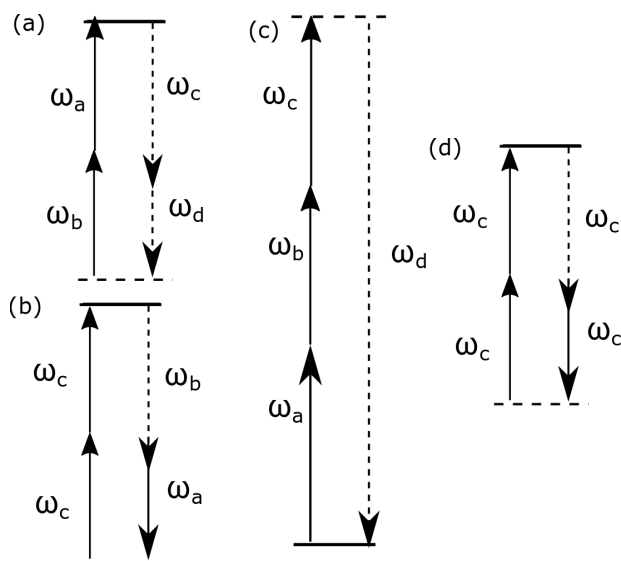


FIG. 2.5: Level diagrams of some possible configurations of FWM, where solid lines represent input fields and dashed lined represent new fields. Many more combinations exist.

(795 *nm* and 762 *nm*) are used to pump to the second excited state and the resulting decay to the  $6P_{3/2}$  state and subsequently the ground state yield seed photons for the FWM process. FWM results in the generation of two newly generated fields  $E_c$  and  $E_d$  with frequencies 5032 *nm* and 422 *nm*. These fields are coherent radiation and have a wavefront determined by the phase matching conditions from FWM. With effecient FWM, this process can be used to convert a photon from one energy to another with out measurement of the signal. Such a conversion would preserve the quantum state which would be used in communications. [44].

We use Rubidium as an example, shown in Fig. 2.6. Here, the 795 *nm* and 762 *nm* fields are input and we observe that the  $6P_{1/2}$  state acts as the intermediary state and results in the emission of 5032 *nm* and 422 *nm* collimated radiation. There are also effects of parasitic decays which remove atoms from the interaction through other decay channels, but it an additional repump field can be used to replenish the system and enhance the FWM process [154]. It is also possible to acheive coupling with other decay channels where a seed field can be used [79]. The one presented here is the stronger effect. However, there

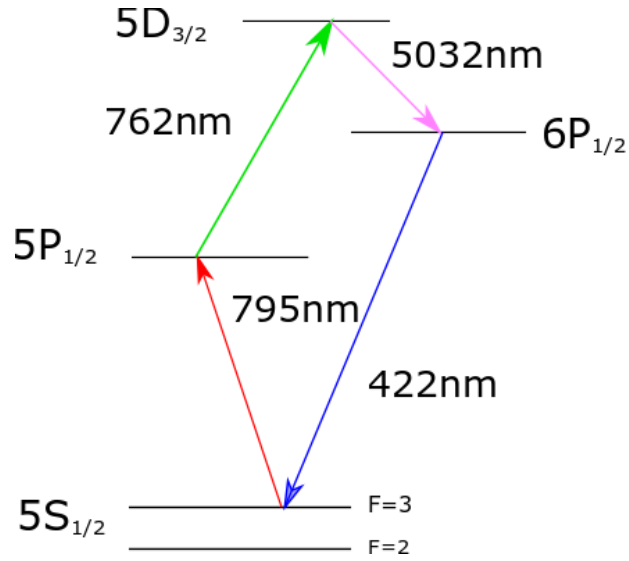


FIG. 2.6: Level diagram of FWM in  $^{85}\text{Rb}$  involving the upper 5D state.

are other decay channels with weaker contribution to FWM [69, 80, 153]. We use the concept of frequency conversion later in Chp. 4 and discuss the decay paths in more detail.

### 2.4.2 FWM as a Source of Decoherence of the Dark State

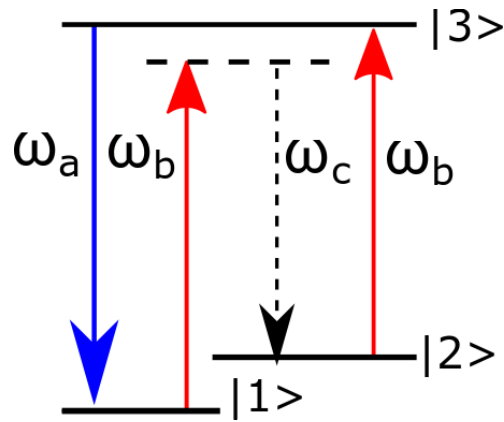


FIG. 2.7: Three-level diagram of FWM where,  $\omega_a$  is the probe,  $\omega_b$  is the pump, and  $\omega_c$  is the conjugate. The decay rates  $\gamma'$ ,  $\gamma$ , and  $\tilde{\gamma}$  are the same as those in Fig. 2.2.

As mentioned before, FWM is detrimental to quantum memories, but inevitable due to the requirement of a large optical depth. Here we discuss the decoherence in EIT

quantum memories as a result of additional noise photons generated from FWM and a potential solution to this issue. We first begin with the Hamiltonian where we have included the newly generated conjugate field [142, 143]

$$\hat{H} = \begin{pmatrix} 0 & 0 & -\frac{\hbar}{2}(\Omega_a e^{i\omega_a t} + \Omega_b e^{i\omega_b t}) \\ 0 & \hbar\omega_{21} & -\frac{\hbar}{2}(\Omega_b e^{i\omega_b} + \Omega_c e^{i\omega_c}) \\ -\frac{\hbar}{2}(\Omega_a^* e^{-i\omega_a t} + \Omega_b^* e^{-i\omega_b t}) & -\frac{\hbar}{2}(\Omega_b^* e^{-i\omega_b} + \Omega_c^* e^{-i\omega_c}) & \hbar\omega_{31} \end{pmatrix}, \quad (2.85)$$

where the pump field couples to both hyper-fine states in a double- $\Lambda$  four-photon resonance with the probe and conjugate fields, as seen in Fig. 2.7. The coupling with the probe is on resonance and produces EIT and traps atoms into the dark state, as was seen sec. 2.3.2. However, the pump coupling with the conjugate field is through a virtual state and allows for population transfer between the hyper-fine split states,  $|1\rangle$  and  $|2\rangle$ . This ruins the coherence established by EIT, as will be demonstrated in this section. We move into the rotating frame using the unitary operator in Eq. 2.48

$$\hat{H} = - \begin{pmatrix} 0 & 0 & \frac{\hbar}{2}(\Omega_a + \Omega_b e^{i(\omega_{12} + \delta)t}) \\ 0 & \hbar\delta & \frac{\hbar}{2}(\Omega_b + \Omega_c e^{i(\omega_{12} + \delta)t}) \\ \frac{\hbar}{2}(\Omega_a^* + \Omega_b^* e^{-i(\omega_{12} + \delta)t}) & \frac{\hbar}{2}(\Omega_b^* + \Omega_c^* e^{i(\omega_{12} + \delta)t}) & \hbar\delta \end{pmatrix}, \quad (2.86)$$

where we have made the substitution  $\delta + \omega_{12} = (\omega_a - \omega_b)$  and for our system  $\omega_{12}$  is the the hyperfine splitting  $\Delta_{HF}$ . Note that the time dependence was not removed by moving into the rotating frame, so we take other measures to address this. We can find an effective Hamiltonian which is time-independent by accounting for the light shift from the AC stark effect. This is done by utilizing the Floquet analysis seen in [45, 143, 155]. The

time-independent Hamiltonian is

$$\hat{H} = - \begin{pmatrix} 0 & \frac{\hbar}{2} \frac{\Omega_b^* \Omega_s}{\omega_{12}} & \frac{\hbar}{2} \Omega_a \\ \frac{\hbar}{2} \frac{\Omega_b \Omega_s}{\omega_{12}} & \hbar(\delta - \frac{|\Omega_b|^2}{\omega_{12}}) & \frac{\hbar}{2} \Omega_b \\ \frac{\hbar}{2} \Omega_a^* & \frac{\hbar}{2} \Omega_b^* & \hbar(\delta - 2 \frac{|\Omega_b|^2}{\omega_{12}}) \end{pmatrix}, \quad (2.87)$$

where we can see that the time dependence has been removed and the energy levels have been shifted by  $\delta_{ls} = \frac{|\Omega_b|^2}{\omega_{12}}$ . In addition to this, we see that there is now an exchange term between the states  $|1\rangle$  and  $|2\rangle$ . We now find the equations of motion like before

$$\dot{\rho}_{11} = i(\rho_{31} - \rho_{13})\Omega_a + \gamma' \rho_{33} + i \frac{\Omega_b \Omega_c}{\omega_{12}} (\rho_{21} - \rho_{12}), \quad (2.88)$$

$$\dot{\rho}_{22} = \frac{i}{2} \Omega_b (\rho_{32} - \rho_{23}) + \gamma \rho_{33} - i \frac{\Omega_b \Omega_c}{\omega_{12}} (\rho_{21} - \rho_{12}), \quad (2.89)$$

$$\dot{\rho}_{21} = \frac{i}{2} (\Omega_b \rho_{13} - \Omega_a \rho_{23}) - (\gamma_{12} - i(\delta - \delta_{ls})) \rho_{21} - i \frac{\Omega_b \Omega_c}{\omega_{12}} (\rho_{11} - \rho_{22}), \quad (2.90)$$

$$\dot{\rho}_{13} = \frac{i}{2} \Omega_a (\rho_{11} - \rho_{33}) - \frac{i}{2} \Omega_b \rho_{21} - (\gamma_{13} - i(\delta - 2\delta_{ls})) \rho_{13} - i \frac{\Omega_b \Omega_c}{\omega_{12} \rho_{32}}, \quad (2.91)$$

$$\dot{\rho}_{23} = \frac{i}{2} \Omega_b (\rho_{22} - \rho_{33}) - \frac{i}{2} \Omega_a \rho_{12} + (\gamma_{23} - i(\delta_{ls} + \gamma)) \rho_{32} - i \frac{\Omega_b \Omega_c}{\omega_{12}} \rho_{31}. \quad (2.92)$$

We notice here that the  $\rho_{21}$  contains a term regarding the population exchange between the  $|1\rangle$  and  $|2\rangle$  states which was not present before. This population exchange removes photons from the dark state and causes noise in the quantum memory [45]. We remedy this, by trying to absorb the conjugate photons before they cause decoherence and couple into the system [42]. We introduce this absorption into the propagation equations in Eq. 2.80

$$\frac{\partial E_a}{\partial z} = \frac{ik_c}{2\varepsilon_0} \chi^{(3)} E_c^*, \quad (2.93)$$

$$\frac{\partial E_c}{\partial z} = \frac{ik_p}{2\varepsilon_0} \chi^{(3)} E_a^* - \frac{D}{L} E_c, \quad (2.94)$$

where D and L are the optical depth and length of the medium, respectively. Taking



the derivative of Eq. 2.94 and plugging the conjugate of Eq. 2.94 in, we see that these equations can be written as

$$\frac{\partial E_a}{\partial z} - ik_c \xi \chi^{(3)} E_c'^* = 0, \quad (2.95)$$

$$\frac{\partial^2 E_c}{\partial z^2} + \frac{\partial}{\partial z} \frac{D}{L} E_c - k_a k_c \xi E_c = 0, \quad (2.96)$$

The solution to this system are dampened hyperbolic functions with solutions [42]

$$E_a(L) = e^{\frac{|\eta_a|L}{D}} E_a'^*(0), \quad (2.97)$$

$$E_c(L) = -i \frac{\eta_a}{|\eta_a|D} e^{\frac{|\eta_a|L}{D}} E_a'^*(0), \quad (2.98)$$

which have a form similar to Eqs. 2.81 and 2.82. However, this shows that the absorption of the new conjugate field in the medium can also reduce the gain on the probe field. As described in Sec. 2.3.1, we use a second two-photon Raman resonance as a competing process with FWM to suppress the generation of additional photons. The experimental configurations for this are given in Ch. 3. With a strong enough absorption,  $D \gg \eta_a$ , it is possible to completely remove the new conjugate field and the additional photons in the signal field. This preserves the quantum state which was stored in the quantum memory.

### 2.4.3 FWM for Transfer of Optical Angular Momentum

In this section, we consider the spatial mode structure of the beams. Here, the notion a picture is worth thousand words has merit, but more in terms of data density. With tunability of the signal beam shapes, we can increase the amount of information which is communicated [109]. In addition to this, by using FWM in conjunction, we can achieve an even larger number of channels for communication [8, 98, 99]. Optical angular momentum (OAM) is a property of light which we take advantage of here [100–102]. OAM modes

have cylindrical spatial profiles defined by the grouping of Laguerre Gauss (LG) modes. These modes are orthonormal and a demodulation scheme has already been developed for them [100, 109, 116]. In this section, we look at the LG spatial structure for light and discuss how FWM can be used to further increase the channel capacity for communications.

In order to look at the spatial dependence, we turn back to the wave equation and more carefully treat the beam profile. We consider the shape of a laser to be cylindrically symmetric and so it is beneficial to adjust our wave equation to that coordinate system

$$\frac{1}{r} \frac{\partial}{\partial r} \left( r \frac{\partial E}{\partial r} \right) + \frac{\partial^2 E}{\partial z^2} + 2ik \frac{\partial E}{\partial z} = 0 \quad (2.99)$$

where we split the field into two parts  $E(r, z) = u(r, z)e^{ikz}$ . The beam profile is given by  $u(r, z)$  and  $e^{ikz}$  the phase is for the propagation.

Like before, we expect the beam envelope to be uniform or have little change with propagation. We make the slow varying or paraxial approximation [20, 23]

$$\left| \frac{\partial^2 E}{\partial z^2} \right| \ll \left| 2k \frac{\partial E}{\partial z} \right|, \quad (2.100)$$

$$\left| \frac{\partial^2 E}{\partial z^2} \right| \ll \left| \frac{1}{r} \frac{\partial}{\partial r} \left( r \frac{\partial E}{\partial r} \right) \right|. \quad (2.101)$$

The wave equation now becomes

$$\frac{1}{r} \frac{\partial}{\partial r} \left( r \frac{\partial E}{\partial r} \right) + 2ik \frac{\partial E}{\partial z} = 0, \quad (2.102)$$

for which the solutions are the Laguerre Gaussian modes [156]

$$u_{\ell,p}(r, z) = \frac{\sqrt{2p!/\pi(|\ell| + p)!}}{w(z)} e^{-\frac{r^2}{w(z)^2}} e^{-\frac{ikr^2 z}{2(z^2 + z_R^2)}} \left( \frac{\sqrt{2}r}{w(z)} \right) \times L_p^{|\ell|} \left( \frac{2r^2}{w(z)^2} \right) e^{i\ell\phi} e^{i(2p+|\ell|+1) \arctan(z/z_R)}, \quad (2.103)$$

where  $w(z) = w_0\sqrt{1 + (z/z_R)^2}$  is the beam waist,  $z_R = \pi w_0^2/\lambda$  is the Rayleigh range, and  $w_0$  is the beam waist at the point of focus. As we continue, we only consider the contribution of the  $\ell$  modes and set  $p = 0$ . These are modes with a constant radial phase profile, but vary by  $2\pi\ell$  in phase along the azimuth, as shown by Fig. 2.8. The hole in the center for non-zero  $\ell$  is from the phase singularity produced from the accumulation of all the phases about the azimuth. We are left with

$$\begin{aligned}
u_\ell(r, z) &= \frac{\sqrt{2/\pi(|\ell|)!}}{w(z)} e^{-\frac{r^2}{w(z)^2}} e^{-\frac{ikr^2z}{2(z^2+z_R^2)}} \left(\frac{\sqrt{2}r}{w(z)}\right) \\
&\times L_0^{|\ell|} \left(\frac{2r^2}{w(z)^2}\right) e^{i\ell\phi} e^{i(|\ell|+1)\arctan(z/z_R)}, \\
&= u'_\ell(r, z) e^{i\phi\ell}.
\end{aligned} \tag{2.104}$$

where we focus on the phase contribution from the  $\ell$ -mode. The rest, packed into  $u'_\ell(r, z)$ , is for handling the beam size and focusing.

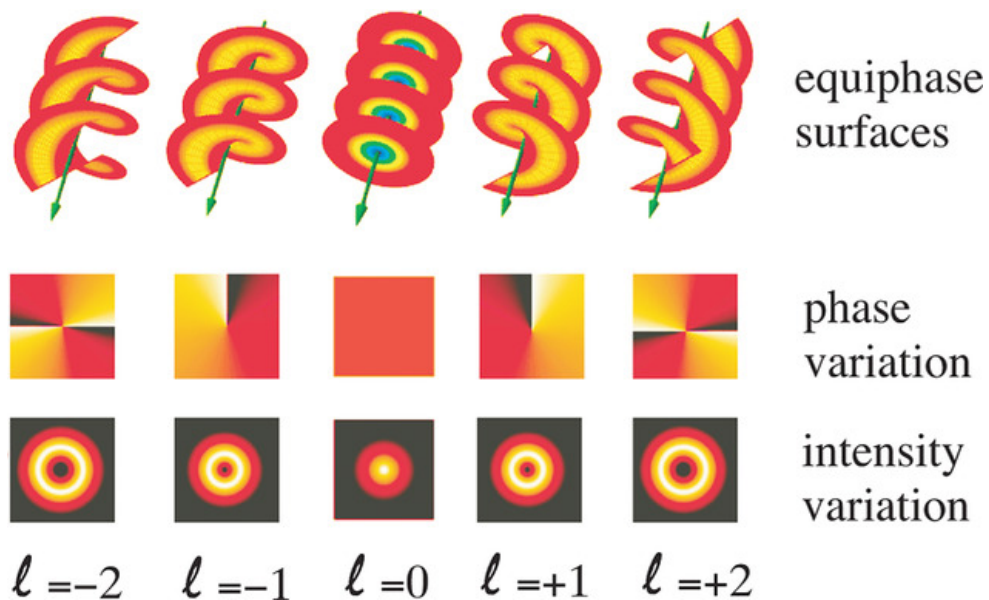


FIG. 2.8: Shown are the equiphase surfaces, phases, and intensity map of the OAM modes for different  $\ell$  numbers. Taken from [157].

Now, we turn our attention back to the polarization response of the medium. Using

Eq. 2.104 for the fields in Eq. 2.68, we find [156]

$$\vec{P}^{(3)} = \varepsilon_0 \chi^{(3)} (u_a(r, z) e^{i(k_a z - \omega_a t + \ell_a \phi)} + u_b e^{i(k_b z - \omega_b t + \ell_b \phi)})^3, \quad (2.105)$$

where we limit ourselves to the FWM conditions we saw in sec. 2.4. The term we keep is

$$\begin{aligned} \vec{P}_p^{(3)} &= \varepsilon_0 \chi^{(3)} E_a^* E_b^2 e^{-i[(2\vec{k}_b - \vec{k}_a)z - (2\omega_b - \omega_a)t + (2\ell_b - \ell_a)\phi]}, \\ &= \varepsilon_0 \chi^{(3)} E_c^* e^{i[\vec{k}_c z - \omega_c t + \phi \ell_c]}. \end{aligned} \quad (2.106)$$

Here, we see an additional component to the phase matching conditions

$$\omega_c = 2\omega_b - \omega_a, \quad (2.107)$$

$$\vec{k}_c = 2\vec{k}_b - \vec{k}_a, \quad (2.108)$$

$$\ell_c = 2\ell_b - \ell_a. \quad (2.109)$$

The spatial mode of the newly generated field is controlled by independently adjusting the OAM for the pump and probe fields [8, 18]. A single beam is limited by the number of OAM modes which can be generated since the mode size scales with the  $\ell$  number. In the twin-beams, signals are carried jointly by the probe and conjugate spatial modes, so various combinations of the two could be used to transmit information, increasing the possible number of channels to  $\ell^2$ . This is discussed in detail in Chp. 6

## 2.5 Quantization of the Electromagnetic Field

So far, we have limited our approach to the semi-classical picture, where we used the quantum treatment for the atoms and the classical description of the optical fields. Here, we switch to the fully quantum picture. This allows us to uncover additional effects which

arise from FWM and overcome the classical shot noise limit. We follow the derivation in [23, 24] and start with the quantization of the electromagnetic fields.

We begin here with the wave equation Eq. 2.12 and consider solutions which satisfy the spatial restraints of a cavity. In this case, the electric field of  $x$ -polarization can be written as a sum over the normal modes of the cavity

$$E_x(z, t) = \sum_i \sqrt{\frac{2\omega_i^2}{V\epsilon_0}} q_i(t) \sin(k_i z), \quad (2.110)$$

where  $V$  is the volume,  $k = \pi n c / L = \omega / c$ , and  $L$  is the length of the cavity. We can write the magnetic field in a similar manner using Eq. 2.8

$$H_y(z, t) = \sum_i \sqrt{\frac{2\omega_i^2}{V\epsilon_0} \frac{\epsilon_0 \mu_0}{k_i}} \dot{q}_i(t) \cos(k_i z), \quad (2.111)$$

then by using Eqs. 2.110 and 2.111, we find the energy of the fields

$$\mathcal{H} = \frac{1}{2} \int_V d\tau (\epsilon_0 E_x^2 + \frac{1}{\mu_0} H_y^2), \quad (2.112)$$

$$\mathcal{H} = \frac{1}{2} \sum_i (\omega_i^2 q_i^2 + \dot{q}_i^2), \quad (2.113)$$

where  $H$  is the classical Hamiltonian of the fields.

From this equation, we see that the energy in the field is that of harmonic oscillators of different modes where  $p_i = m_i \dot{q}_i$  is the canonical momentum of unit mass and  $\omega_i^2 = k_i^2 c^2$  is the frequency of the mode. By drawing analogy to the quantum harmonic oscillator, we replace the position and momentum as operators which obey the commutation relations

$$[\hat{q}_i, \hat{p}_j] = i\hbar \delta_{ij}, \quad (2.114)$$

$$[\hat{q}_i, \hat{q}_j] = [\hat{p}_i, \hat{p}_j] = 0, \quad (2.115)$$

We make a canonical transformation to the annihilation and creation operators

$$\hat{q}_i = \hbar(\hat{a}_i e^{-i\omega_i t} + \hat{a}_i^\dagger e^{i\omega_i t}), \quad (2.116)$$

$$\hat{p}_i = im_i \omega_i \hbar(\hat{a}_i^\dagger e^{i\omega_i t} - \hat{a}_i e^{-i\omega_i t}), \quad (2.117)$$

$$\hat{a}_i e^{-i\omega_i t} = \frac{1}{2m_i \hbar \omega_i} (m_i \omega_i \hat{q}_i + i \hat{p}_i), \quad (2.118)$$

$$\hat{a}_i^\dagger e^{i\omega_i t} = \frac{1}{2m_i \hbar \omega_i} (m_i \omega_i \hat{q}_i - i \hat{p}_i), \quad (2.119)$$

which follow the commutation relations

$$[\hat{a}_i, \hat{a}_j^\dagger] = \delta_{ij}, \quad (2.120)$$

$$[\hat{a}_i, \hat{a}_j] = [\hat{a}_i^\dagger, \hat{a}_j^\dagger] = 0. \quad (2.121)$$

Now, by substituting Eqs. 2.116 and 2.117 into Eq. 2.113, we find the quantized Hamiltonian

$$\hat{\mathcal{H}} = \hbar \sum_i (\hat{a}_i^\dagger \hat{a}_i + \frac{1}{2}), \quad (2.122)$$

and the quantized electromagnetic fields are found by plugging Eqs. 2.116 and 2.117 into Eq. 2.110 and 2.111

$$\hat{E}_x = \sum_i \mathcal{E}_i (\hat{a}_i e^{-i\omega_i t} + \hat{a}_i^\dagger e^{i\omega_i t}) \sin(k_i z), \quad (2.123)$$

$$\hat{H}_y = -i \varepsilon_0 c \sum_i \mathcal{E}_i (\hat{a}_i e^{-i\omega_i t} - \hat{a}_i^\dagger e^{i\omega_i t}) \cos(k_i z), \quad (2.124)$$

where  $\mathcal{E}_i = \sqrt{\frac{\hbar \omega_i}{\varepsilon_0 V}}$  and has units of the electric field. So far, we have only considered a one dimensional cavity, but we now extend this for a three dimensional cavity. We expand the

electric field in terms of plane waves [23]

$$\hat{E}_x = \sum_i \mathcal{E}_i (\hat{a}_i e^{i(\vec{k}_i \cdot \vec{r} - \omega_i t)} + \hat{a}_i^\dagger e^{-i(\vec{k}_i \cdot \vec{r} - \omega_i t)}), \quad (2.125)$$

$$\hat{H}_y = -i\varepsilon_0 c \sum_i \mathcal{E}_i (\hat{a}_i e^{-i(\vec{k}_i \cdot \vec{r} - \omega_i t)} - \hat{a}_i^\dagger e^{i(\vec{k}_i \cdot \vec{r} - \omega_i t)}), \quad (2.126)$$

Now that we have our quantized fields, we treat different distributions of light. In the Fock state basis, also known as the number basis, we track the number of photons in a specific mode by using the number operator ( $\hat{n}$ ) and add and subtract excitations using the creation and annihilation operators

$$\hat{a}|n\rangle = \sqrt{n}|n-1\rangle, \quad (2.127)$$

$$\hat{a}^\dagger|n\rangle = \sqrt{n+1}|n+1\rangle, \quad (2.128)$$

$$\hat{a}^\dagger \hat{a}|n\rangle = \hat{n}|n\rangle = n|n\rangle. \quad (2.129)$$

However, for a coherent source we use the eigenstate of the annihilation operator with eigenvalue  $\hat{a}|\alpha\rangle = \alpha|\alpha\rangle$ , known as the coherent state. It is written as a combination of the Fock states

$$|\alpha\rangle = e^{-|\alpha|^2/2} \sum_{n=0}^{\infty} \frac{\alpha^n}{\sqrt{n!}} |n\rangle, \quad (2.130)$$

It is also useful to write the coherent state in terms of the displacement operator [23]

$$|\alpha\rangle = \hat{D}|\alpha\rangle = e^{\hat{a}^\dagger \alpha - \hat{a} \alpha^*} |0\rangle, \quad (2.131)$$

which states that the coherent state is generated by displacing the harmonic oscillator ground state, the vacuum state.

### 2.5.1 Quantum Limit of Optical Measurements

The coherent state has special noise properties when compared to classical light. The intensity or number of photons in the coherent state are given by

$$\langle \alpha | \hat{n} | \alpha \rangle = \langle \alpha | \hat{a}^\dagger \hat{a} | \alpha \rangle = |\alpha|^2, \quad (2.132)$$

Furthermore, the photon number variance in the signal gives us our limits on measurement. The variance in the photon number is given by

$$\Delta \hat{n}^2 = \langle \hat{n}^2 \rangle - \langle \hat{n} \rangle^2 = |\alpha|^2, \quad (2.133)$$

which shows that the photon number variance scales with the number of photons. These are the fluctuations for a poissonian distribution and this noise limit is called the shot noise limit. This noise comes from the fact that the photons are not spaced evenly in time and arrive at the detector in bunches. This results in the variance of the photon number (or intensity) measurement.

It is also possible to measure the electric field directly in terms of its amplitude and phase. For this we would move to the quadrature notation

$$\hat{E}_x = \sum_i \mathcal{E}_i (\hat{X}_i \cos(kz - \omega t) + \hat{Y}_i \sin(\vec{k}_i \cdot \vec{r} - \omega_i t)), \quad (2.134)$$

where  $X$  is the amplitude quadrature and  $Y$  is the phase quadrature,

$$\hat{X} = \frac{1}{2}(\hat{a} + \hat{a}^\dagger), \quad (2.135)$$

$$\hat{Y} = \frac{1}{2i}(\hat{a} - \hat{a}^\dagger). \quad (2.136)$$



These quadratures follow the commutation relations

$$[X_k, Y_j] = \delta_{kj} \frac{i}{2}, \quad (2.137)$$

$$[X_k, X_j] = [Y_k, Y_j] = 0, \quad (2.138)$$

Since  $X$  and  $Y$  don't commute with each other. The uncertainty of these quadratures for a coherent state is given by [23, 158]

$$\Delta X^2 = 1/4, \quad (2.139)$$

$$\Delta Y^2 = 1/4, \langle \Delta X \rangle^2 \langle \Delta Y \rangle^2 \geq 1/16. \quad (2.140)$$

However, there are other states of light which have the same minimum uncertainty relationship, but the uncertainties of individual quadratures are tunable [23, 158]. By operating the squeezing operator on the coherent state, we can produce this new squeezed state

$$\hat{S}|\alpha\rangle = e^{\xi(\hat{a}\hat{a} - \hat{a}^\dagger\hat{a}^\dagger)}|\alpha\rangle = |\xi\rangle, \quad (2.141)$$

which has uncertainties

$$\Delta X^2 = 1/4e^{-2\xi}, \quad (2.142)$$

$$\Delta Y^2 = 1/4e^{2\xi}, \quad (2.143)$$

$$\Delta X^2 \Delta Y^2 \geq 1/16, \quad (2.144)$$

where we observe reduced fluctuations in the amplitude quadrature and increased fluctuations in the phase quadrature as a function of  $\xi$ , all the while the minimum uncertainty is maintained. Eq. 2.143 and 2.144 are the expected noise quadratures are for single-mode squeezer. A detailed derivation on squeezing and the noise quadratures follows in the next

section. We briefly introduce them here to whet the appetite. The next section deals with two-mode squeezed states which are generated by FWM.

## 2.5.2 Squeezed light from FWM

Now that we have our tool-set for analysis, we turn back to FWM and the propagation equations. By drawing analogy from the classical propagation equations Eq. 2.80, we find the propagation equations for the quantum operators which represent our fields [23]. The new differential equations describing the propagation are

$$\frac{d\hat{a}}{dz} = ik_a \hat{b}^\dagger, \quad (2.145)$$

$$\frac{d\hat{b}}{dz} = ik_b \hat{a}^\dagger, \quad (2.146)$$

where  $\hat{a}$  and  $\hat{b}$  represent the probe and conjugate fields, respectively. The solutions to these equations are [23, 159, 160]

$$\hat{a}(L) = \hat{a}(0) \cosh(\xi) + i\hat{b}^\dagger(0) \sinh(\xi), \quad (2.147)$$

$$\hat{b}(L) = \hat{b}(0) \cosh(\xi) + i\hat{a}^\dagger(0) \sinh(\xi). \quad (2.148)$$

where  $\xi = |k_a||k_b|L$  is the squeezing parameter (the  $r$  seen in the prior section) and  $L$  is the length of the medium. The parameter  $\xi$  depends on the strength of the pump field and the optical depth of the medium. The FWM transformation can be written as a unitary operator, the squeezing operator

$$\hat{S} = e^{\xi(\hat{b}^\dagger \hat{a}^\dagger - \hat{a} \hat{b})}, \quad (2.149)$$

which operates on the coherent state to produce a squeezed state

$$\hat{S}|\alpha\rangle = |\xi\rangle. \quad (2.150)$$

From here, we look at some properties of the two-mode squeezed state. We find the total number of photons after the gain [23, 24, 159]

$$\langle \hat{n}_a \rangle = \langle \hat{S}^\dagger \hat{a}^\dagger(L) \hat{S} \hat{S}^\dagger \hat{a}(L) \hat{S} \rangle = \cosh^2(\xi) |\alpha|^2 + \sinh^2(\xi) \approx G |\alpha|^2, \quad (2.151)$$

$$\langle \hat{n}_b \rangle = \langle \hat{S}^\dagger \hat{b}^\dagger(L) \hat{S} \hat{S}^\dagger \hat{b}(L) \hat{S} \rangle = \cosh^2(\xi) |\alpha|^2 + \sinh^2(\xi) \approx (G - 1) |\alpha|^2, \quad (2.152)$$

$$\langle \hat{n}_a + \hat{n}_b \rangle \approx (2G - 1) |\alpha|^2 \quad (2.153)$$

where  $G = \cosh^2(\xi)$  is the gain, and we have applied the initial condition of the unseeded conjugate field  $\hat{b} = \hat{b}^\dagger = 0$ . We also look at the noise present in the quadratures, like before. But we first transform the quadratures according to the Eq. 2.148 and 2.148

$$\hat{X}_a(L) = \frac{1}{2}(\hat{a}(L) + \hat{a}^\dagger(L)) = \hat{X}_a(0) \cosh(\xi) - \hat{Y}_b(0) \sinh(\xi), \quad (2.154)$$

$$\hat{Y}_a(L) = \frac{1}{2i}(\hat{a}(L) - \hat{a}^\dagger(L)) = \hat{Y}_a(0) \cosh(\xi) + \hat{X}_b(0) \sinh(\xi), \quad (2.155)$$

$$\hat{X}_b(L) = \frac{1}{2}(\hat{b}(L) + \hat{b}^\dagger(L)) = \hat{X}_b(0) \cosh(\xi) - \hat{Y}_a(0) \sinh(\xi), \quad (2.156)$$

$$\hat{Y}_b(L) = \frac{1}{2i}(\hat{b}(L) - \hat{b}^\dagger(L)) = \hat{Y}_b(0) \cosh(\xi) - \hat{X}_a(0) \sinh(\xi). \quad (2.157)$$

We now find the variance of these quadratures

$$\Delta \hat{X}_a(L)^2 = \Delta \hat{Y}_a(L)^2 = \Delta \hat{X}_b(L)^2 = \Delta \hat{Y}_b(L)^2 = \frac{1}{4}(2G - 1), \quad (2.158)$$

$$\Delta \hat{X}_a(L)^2 \Delta \hat{Y}_a(L)^2 = \Delta \hat{X}_b(L)^2 \Delta \hat{Y}_b(L)^2 = \frac{1}{16}(2G - 1)^2, \quad (2.159)$$

which are larger than the quadrature noise in the coherent state and is seen to increase

linearly with the gain. The comparison of the noise quadratures for coherent light and squeezed twin-beams is shown in Fig. 2.9 (a) and (b). The reason this noise is larger is due to the process used to amplify the beams. In FWM, the conjugate and probe photons are randomly added in a pairwise fashion. Thus, the variances of the quadratures for the individual fields are larger than shot noise, but the pair generation makes it so the joint-noises in the two beams are correlated. We observe this by looking at the joint-quadrature variance and the corresponding uncertainty.

$$\Delta\hat{X}_{\pm}(L)^2 = \Delta(\hat{X}_a(L) \pm \hat{X}_b(L))^2 = \frac{1}{4}e^{\pm 2\xi}, \quad (2.160)$$

$$\Delta\hat{Y}_{\pm}(L)^2 = \Delta(\hat{Y}_a(L) \pm \hat{Y}_b(L))^2 = \frac{1}{4}e^{\mp 2\xi}, \quad (2.161)$$

$$\Delta\hat{X}_{\pm}(L)^2\Delta\hat{Y}_{\pm}(L)^2 = \frac{1}{16}, \quad (2.162)$$

where we see that the minimum uncertainty is maintained and that we have two squeezed joint-quadratures,  $\hat{X}_-$  and  $\hat{Y}_+$ , with noise below the shot noise limit. We also have the  $\hat{X}_+$  and  $\hat{Y}_-$  joint-quadratures, which are anti-squeezed with noise greater than shot noise. The joint-quadratures are plotted in Fig. 2.9(c) and (d). The FWM process increases the power of the fields used for detection, while keeping the relative fluctuations between the two beams at the same level. The result is the noiseless amplification of the signal.

### 2.5.3 Balanced Homodyne Detection for Squeezing Quadrature Measurements

We look more carefully at the experimental geometry and compare classical measurements using coherent light to quantum enhanced measurements using squeezed light. In optics, it is common to amplify a weak optical signal with the use of a local oscillator or use a beam cube for differential measurements [81, 161]. By doing this, common mode-noise

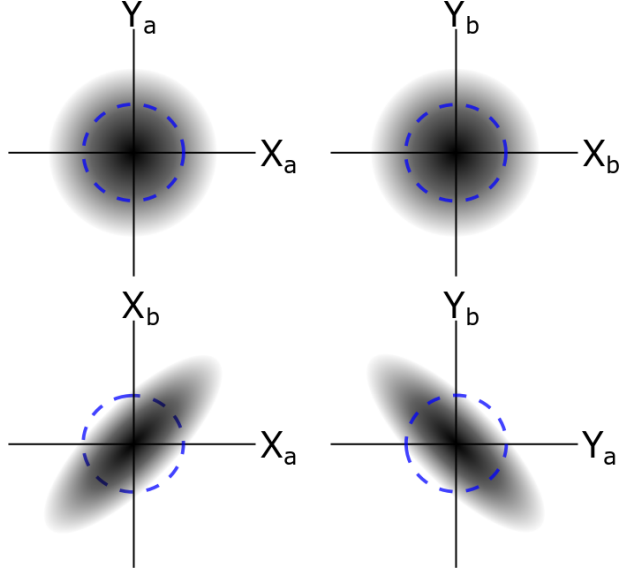


FIG. 2.9: (a) shows the noise as a fuzz for the probe beam after amplification and the blue dashed lines are shot noise for a beam of equivalent power. (b) shows the noise as a fuzz for the conjugate beam after amplification and the blue dashed lines are shot noise for a beam of equivalent power. (c) shows the joint-amplitude quadrature with squeezing along the difference and anti-squeezing along the sum. (d) shows the joint-phase quadrature with squeezing along the sum and anti-squeezing along the difference.

can be removed and the signal is amplified by the strength of the local oscillator. We show how balanced homodyne detection can be useful and how using squeezed light gives further enhancement.

Here, we introduce the beam splitter formalism in a semi-classical framework, as done in [81]. We will first look at the mixing of a vacuum fields with a local oscillator which will show the measurement of shot noise. Then we consider a squeezed vacuum mixed with a local oscillator. This allows us to measure the different noise quadratures.

We begin by separating the field into its noise and amplitude portions

$$\alpha_1 = (|\alpha| + \delta\hat{X}_\alpha + i\delta\hat{Y}_\alpha)e^{i\phi}, \quad (2.163)$$

$$\alpha_0 = \delta\hat{X}_{\alpha_0} + i\delta\hat{Y}_{\alpha_0}, \quad (2.164)$$

where  $\delta X_\alpha$  and  $\delta Y_\alpha$  are the amplitude and phase noise of the coherent beam. We have

also described vacuum fluctuations ( $\delta X_{\alpha_0}$  and  $\delta Y_{\alpha_0}$ ) in the same mode as our field. We implement a balanced detector with a 50/50 beam splitter, as shown in Fig. 2.10 (a). The operation of the beam splitter is written as

$$\hat{B} = \frac{1}{\sqrt{2}} \begin{pmatrix} 1 & i \\ i & 1 \end{pmatrix}. \quad (2.165)$$

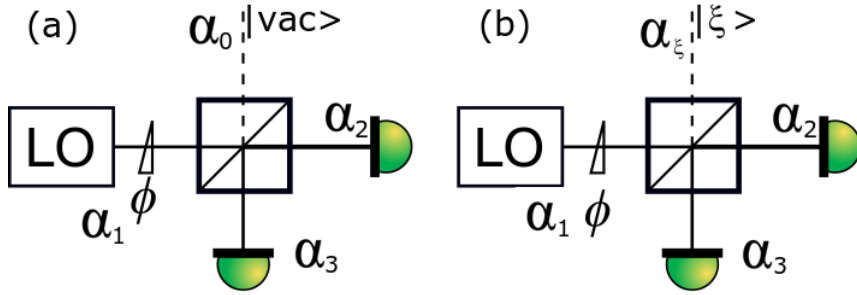


FIG. 2.10: (a) shows the detection using homodyne detection of a local oscillator (LO) mixed with a vacuum. (b) shows homodyne detection, but with a squeezed vacuum input.

For this balanced detection, we are splitting the coherent LO into two and detecting each beam and then taking the difference. Take note that the dark port introduces vacuum fluctuations into the system. For this, our new state is

$$|\alpha_2, \alpha_3\rangle = \frac{1}{\sqrt{2}} \begin{pmatrix} 1 & i \\ i & 1 \end{pmatrix} \begin{pmatrix} \alpha_1 \\ \alpha_0 \end{pmatrix} = \frac{1}{\sqrt{2}} \begin{pmatrix} \alpha_1 + i\alpha_0 \\ i\alpha_1 + \alpha_0 \end{pmatrix}, \quad (2.166)$$

where we find the differential current of the balanced detector as

$$\begin{aligned} i_- &= \langle \alpha, \alpha_3 | \hat{a}_2^\dagger \hat{a}_2 - \hat{a}_3^\dagger \hat{a}_3 | \alpha_2, \alpha_3 \rangle = \alpha_2^* \alpha_2 - \alpha_3 \alpha_3^*, \\ &= 2|\alpha|(\delta X_{\alpha_0} \sin(\phi) - \delta Y_{\alpha_0} \cos(\phi)), \end{aligned} \quad (2.167)$$

where we have made the assumption that the contributions of order  $\delta X^2 \ll |\alpha| \delta X$  are negligible. We already see that the noise contribution from the coherent field drops out

entirely and the differential signal is purely based on the noise of the vacuum amplified by the coherent field amplitude. Here, we find the variance as [81]

$$\begin{aligned}\Delta i_-^2 &= \langle i_-^2 \rangle = 4|\alpha|^2(\delta X_{\alpha_0}^2 \sin^2(\phi) + \delta Y_{\alpha_0}^2 \cos^2(\phi)), \\ &= |\alpha|^2,\end{aligned}\tag{2.168}$$

where  $\delta X_{\alpha_0}^2 = \delta Y_{\alpha_0}^2 = 1/4$  for the vacuum. Terms containing  $\cos(\phi)\sin(\phi)$  have also been removed by averaging over time. Here, we see that the noise scales with the number of photons in the local oscillator (LO- $\alpha'_1$ ), just like before. Additionally, it has no dependence on the phase of the LO. This is the noise expected for a coherent state.

Balanced homodyne detection can be extended to using squeezed light input rather than vacuum, as shown in Fig. 2.10 (b). The sole requirement for this is that the LO must be much larger than the signal input. For simple demonstration, we look at the case of a squeezed vacuum. In the case of this squeezer, we insert a squeezed vacuum into the dark port in place of the coherent vacuum

$$\alpha_0 \rightarrow \alpha_\xi = \delta X_{\alpha_\xi} + i\delta Y_{\alpha_\xi},\tag{2.169}$$

where the noise in the amplitude and phase are squeezed and anti-squeezed, respectively. Following the same calculations, we find that the variance of the differential current is

$$\Delta i_-^2 = 4|\alpha|^2(\Delta X_{\alpha_\xi}^2 \sin^2(\phi) + \Delta Y_{\alpha_\xi}^2 \cos^2(\phi))\tag{2.170}$$

where  $X_{\alpha_\xi}^2 = 1/4e^{-2r}$  and  $Y_{\alpha_\xi}^2 = 1/4e^{2r}$  are the noise quadratures described in Eqs. 2.143 and 2.144. Additionally, homodyne measurement allows for tuning between the different noise quadratures which is useful for reducing specific noises in a system. In chp. 7, we extend this homodyne detection for two-mode squeezed light generated through FWM

which has two squeezed joint-quadratures.



# CHAPTER 3

## Suppression of FWM in Quantum Memory

In this chapter, we demonstrate the suppression of FWM which arises in EIT and Raman quantum memories due to the nonlinear response of Rb to the strong pump field (control field for memories). We utilize Raman two-photon absorption in a ladder configuration to absorb the conjugate (called Stokes in this chapter) field as it is generated, as discussed in sec. 2.4.2. We show that the conjugate absorption also leads to similar levels of gain suppression in the signal field. This gain in the signal leads to data corruption through the addition of noise photons.

### 3.1 Experimental arrangements

In this chapter we tested two interaction configurations widely used in quantum memory experiments. In the first case a strong control field and a weak probe field form a resonant  $\Lambda$  system, the configuration commonly used to realize EIT based quantum

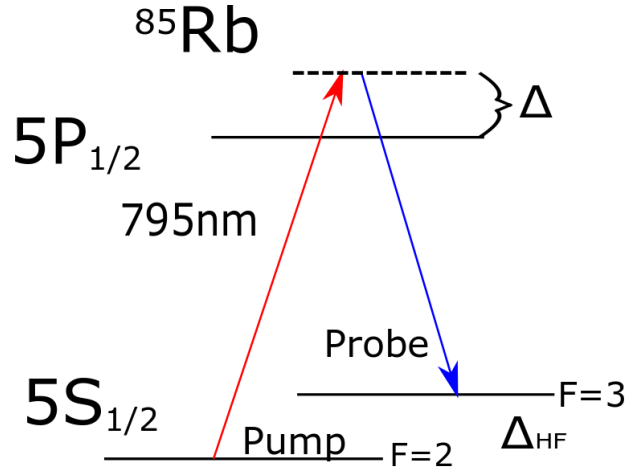


FIG. 3.1: Level diagram of Rb atom based quantum memory.

memory [147, 162, 163]. In the second case, two optical fields are far-detuned from any optical resonances, while remaining in a two-photon resonance. Both are shown by the level diagram in Fig. 3.1 for different values of  $\Delta$ . This arrangement closely resembles the interaction scheme used for the off-resonant Raman memory experiments [164]. In both cases the additional scattering of the strong control field off the ground-state coherence at the probe field's optical transition results in the generation of a new Stokes optical field in a double- $\Lambda$  four-photon resonance. As it was shown before, both theoretically and experimentally, this additional FWM interaction results in the incoherent amplification of the original probe field, leading to uncorrelated excess quantum noise in the quantum memory channel. An in situ resonant absorption for the newly-generated Stokes field suppresses the four-wave mixing. In both configurations, we rely on the Raman transition to the second excited electronic state, enabled by an additional Raman pump optical field in a ladder configuration, to create a strong absorption exclusively for the Stokes field. Simultaneously, we pay particular attention so that this additional laser field does not modify the optical propagation of either the control or the probe fields, so its potential effect on

quantum memory performance is avoided.

Since both interaction schemes are quite similar, we can use the same basic experimental setup to test both of them. The schematic of the experimental setup is shown in Fig. 3.2.

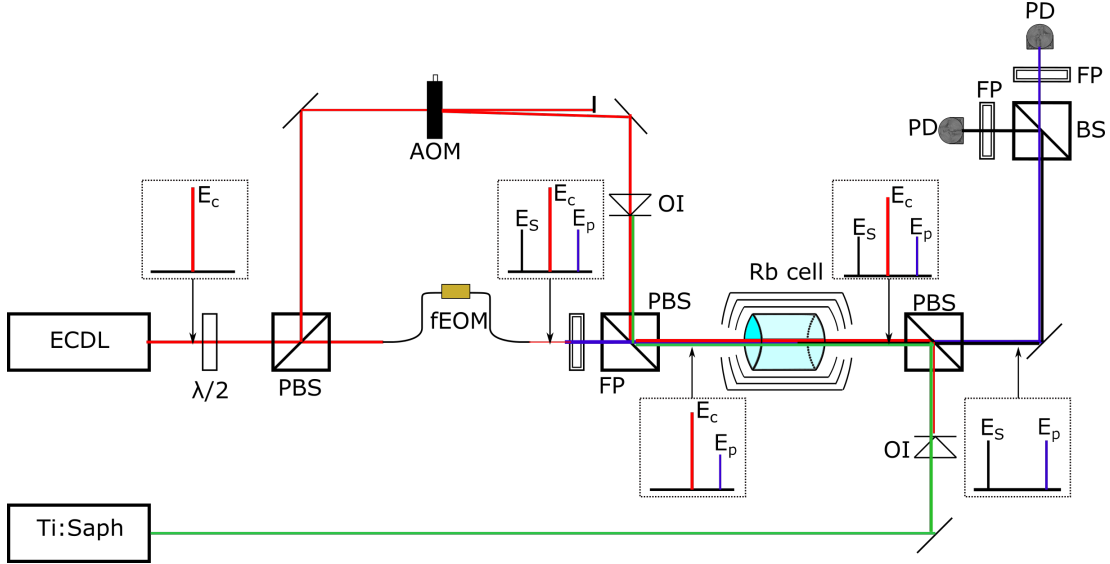


FIG. 3.2: Optical schematic of setup. ECDL and Ti:Sapph denote the two independent lasers used in the experiment (external cavity diode laser and Ti:Sapph cw laser, correspondingly). Optical path of the control field is shown in red, the Raman pump laser in green, and the probe and Stokes fields are correspondingly blue and black. See text below for abbreviations.

Since the relative phase coherence between the control and probe fields is crucial for the quality of two-photon resonances, we derive both of these fields from a single laser (external cavity diode laser, or ECDL) tuned to the  $D_1$  line of Rb (wavelength 794.6 nm). The probe field is produced by phase-modulating a fraction of the laser output by a fiber electro-optical modulator (fEOM) and filtering out one of the first-order modulation sidebands using a tunable fabri-perot etalon (FP) with 20 GHz free spectral range. The remaining laser output passed through an acousto-optical modulator (AOM), and the +1 modulation sideband was used as a control field and then passed through an optical isolator (OI). The control and the probe field were recombined at a polarizing beam splitter (PBS)

before interaction with atoms. Maximum available control power was  $\approx 30$  mW, and the power of the probe field was  $140 \mu\text{W}$ . After the cell, the control field was filtered out by another PBS, and the remaining optical beam was sent to a non-polarizing beam splitter (BS), two outputs of which were directed into two independent fabri-perot etalons, tuned to transmit correspondingly the probe and stokes fields. A cw Ti:Sapphire laser (Ti:Sapph) tuned to the  $5P_{1/2} \rightarrow 5D_{3/2}$  transition of Rb (wavelength 762.1 nm) was used as a Raman pump field. It was combined with the rest of the optical fields at the second polarizing beam splitter and traversed the cell in a counter-propagating direction to minimize the Doppler broadening of a two-photon resonance. All laser beams were weakly collimated inside the cell to the diameter of 1 mm. Since all the optical fields were nearly collinear inside the cell, two optical isolators (OI) were placed to protect both lasers from the incoming strong pump beams.

For these experiments, described below, we used a Pyrex cylindrical cell (diameter 25 mm, length 75 mm) containing natural abundance Rb isotope mixture. It was placed inside a three-layer magnetic shielding to suppress stray magnetic fields. The temperature of the cell was actively stabilized at  $90^\circ\text{C}$  using an electrical heater wrapped around the innermost layer of the magnetic shielding. The corresponding atomic densities were  $1.7 \cdot 10^{12} \text{ cm}^{-3}$  for  $^{85}\text{Rb}$  and  $0.7 \cdot 10^{12} \text{ cm}^{-3}$  for  $^{87}\text{Rb}$ .

## 3.2 Resonant EIT case

EIT configuration corresponds to both control and probe fields' frequencies tuned near optical resonances. For pure EIT we would expect to observe an increase in the probe's transmission when the two-photon detuning matched the hyperfine splitting between two Rb ground states [165]. The width of this resonance, as well as the residual absorption, was determined by the strength of the control field and the decoherence rate of the ground-

state coherence. The co-existing four-wave mixing typically increases the height of the probe field transmission due to additional gain. Simultaneously, it enables the generation of an additional stokes optical field at the optical frequency shifted down by the hyperfine splitting from the control field, as shown in Fig. 3.3. If the residual probe absorption under the pure EIT conditions is negligible, under the combined EIT and FWM effects, the probe output amplitude at the peak may exceed its initial value. Successful FWM suppression, in this case, should eliminate this additional gain; in the ideal case scenario, the output stokes field should completely disappear, while the probe transmission would diminish to the level determined only by the two-photon EIT resonance [42]. Under the realistic conditions of limited control power, even at maximum EIT, the probe transmission is insignificant and FWM gain does not elevate the signal level above its input value, so it is hard to distinguish the two processes as both add up coherently in the probe propagation [166–168]. However, the appearance of the stokes field in the same range of two-photon detunings when no input stokes field was present is a clear sign of the four-wave mixing process. The exact values of the FWM gain for both the probe and stokes fields depended on the mutual spatial alignment of the control and probe beams. We normally adjusted the beams' positions to achieve higher powers and similar sensitivities to the control beam alignment for both probe and stokes outputs.

For the EIT experiments the ECDL frequency was locked to the  $5S_{1/2}F = 3 \rightarrow 5P_{1/2}F' = 3$  transition of  $^{85}\text{Rb}$  using a separate reference cell (not shown in Fig. 3.2), due to the +80 MHz AOM-induced frequency shift the control field was tuned 80 MHz above the  $5S_{1/2}, F = 3 \rightarrow 5P_{1/2}F' = 3$  optical transition. To ensure that the frequency difference between the control and the probe match the  $^{85}\text{Rb}$  hyperfine splitting  $\Delta_{HF} = 3035$  MHz, the rf modulation frequency for fEOM was set on  $\approx 3115$  MHz. By varying the frequency difference between the control and probe optical fields by sweeping the modulation frequency of the fEOM, we observed clear transmission peak in the probe field

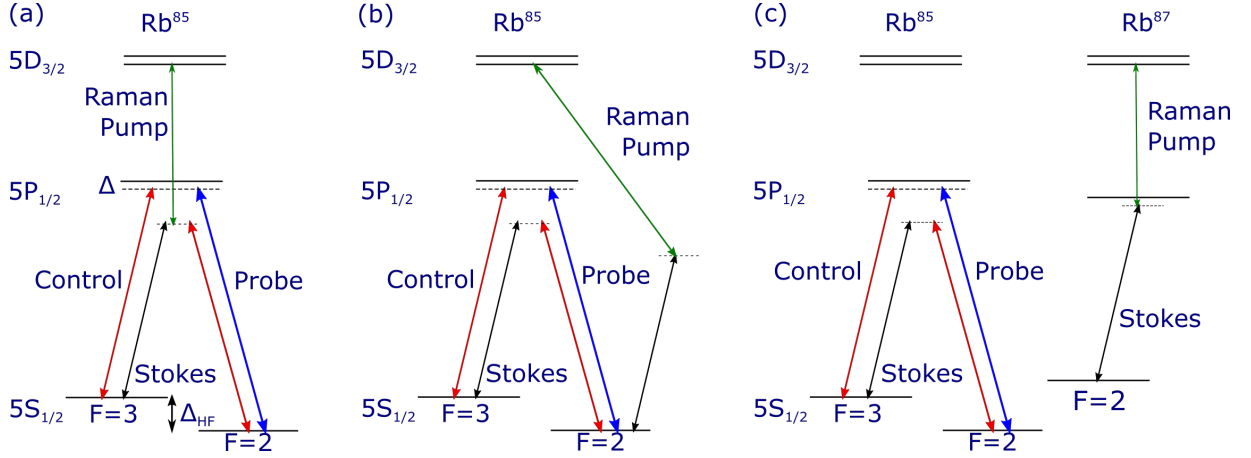


FIG. 3.3: Possible realizations of a ladder Raman absorption resonance for the stokes field in EIT configuration using only  $^{85}\text{Rb}$  atoms (*a,b*), or using  $^{85}\text{Rb}$  for EIT and  $^{87}\text{Rb}$  for Raman absorption (*c*).  $\Delta$  is 80 MHz, and  $\Delta_{\text{HF}}$  is 3035 MHz.

around two-photon resonance conditions, as well as generation of the stokes field, marking the presence of the FWM effect.

Possible realizations of the Raman absorption resonance for the stokes field in this configuration are shown in Fig. 3.3. If only one Rb isotope is involved, there are two possible arrangements. One is when the stokes field and the Raman pump field form a “ladder” from  $5S_{1/2}$ ,  $F = 3$  ground state to  $5D_{3/2}$  second excited state, as shown in Fig. 3.3(a). In this case, the wavelength of the Raman pump field is  $\lambda_{\text{pump}} = 762.0976$  nm and produces the desired strong absorption resonance for the stokes field. Unfortunately, in this configuration the control field and the Raman pump field also form a ladder system, resulting in two-photon absorption of the control field. For instance, under the conditions when we observed 60% stokes absorption, we also measured 20% control field absorption, as shown in Fig. 3.4(a). In principle, if sufficient control field power is available, such additional control absorption may not strongly affect the EIT interaction. However, a noticeable longitudinal variation of the control field power can lead to additional inhomogeneous broadening of the EIT resonance and, for example, negatively affect the memory performance.

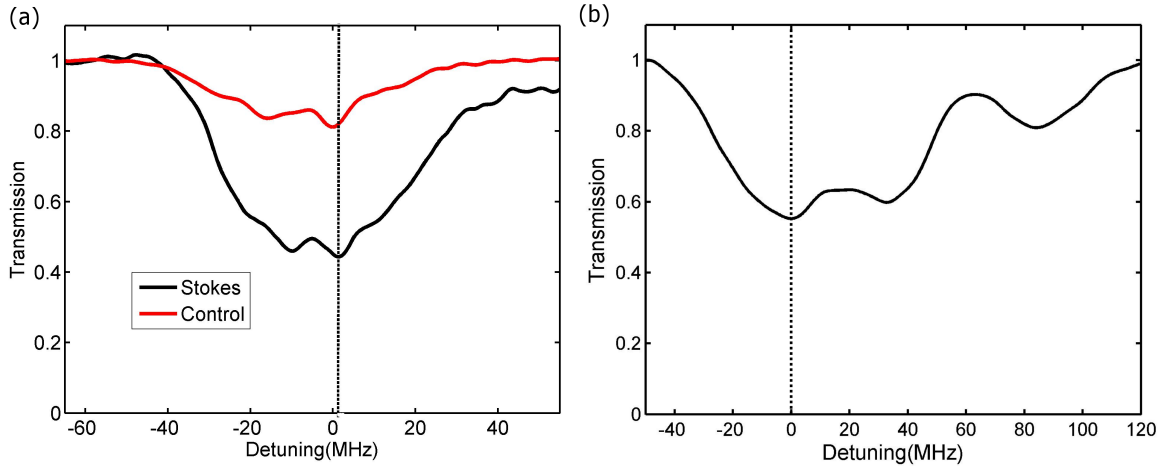


FIG. 3.4: (a) Measured transmission for stokes (black) and control (red) optical fields as the Raman pump frequency is scanned across the two-photon absorption resonance in the level configuration shown in Fig. 3.3(a). Both control and stokes fields experience absorption since they are simultaneously in a two-photon resonance with the pump. (b) Stokes field transmission vs Raman pump frequency using  $^{87}\text{Rb}$  resonances, as shown in Fig. 3.3(c). The control field has no absorption in this case, and thus not shown. All curves are normalized to the transmission value without Raman pump. Vertical dashed lines indicate the optimal operational frequency. Raman pump power was 180 mW for (a) and 220 mW for (b).

In principle, it is possible to avoid the control absorption completely by arranging the frequencies of the stokes field and the Raman pump field to form a two-photon resonance between the  $5S_{1/2}, F = 2$  and  $5D_{3/2}$  levels, as shown in Fig. 3.3(b). However, due to larger detuning from the intermediate excited level, this configuration leads to weaker Raman absorption. We were not able to observe more than 15% stokes absorption even at maximum available pump power ( $\approx 250$  mW).

Thus, we had to use a two-isotope configuration shown in Fig. 3.3(c), using  $5S_{1/2}, F = 2 \rightarrow 5P_{1/2}, F' = 2 \rightarrow 5D_{3/2}$  levels in  $^{87}\text{Rb}$  for stokes absorption. This transition corresponds to the Raman pump wavelength of 762.0995 nm. The sample stokes field absorption is shown in Fig. 3.3(b) for the Raman pump power 220 mW. It is easy to observe multiple absorption resonances, due to the hyperfine structure of the  $5D_{3/2}$  excited state, unresolved under the Doppler broadening. Typically, we tuned to the strongest Raman absorption peak.

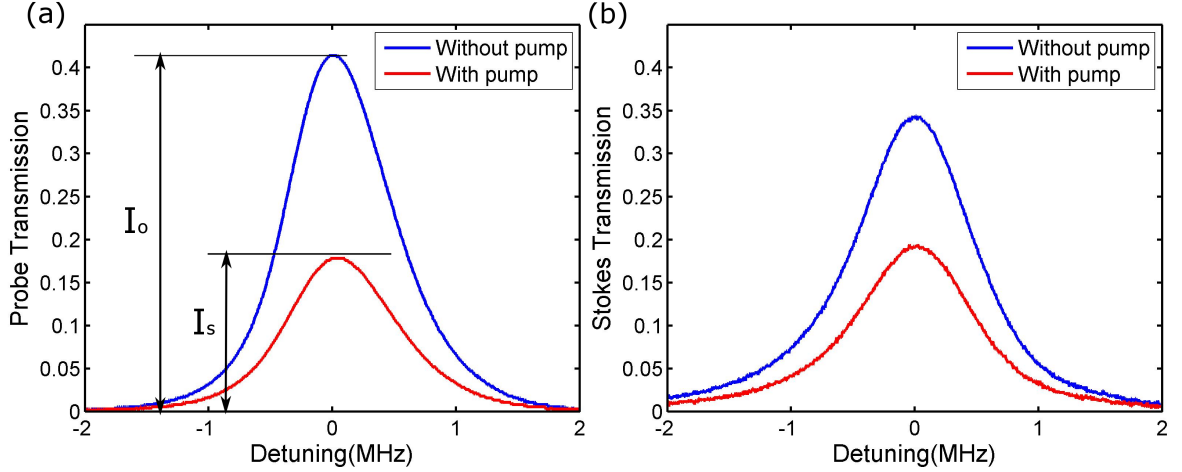


FIG. 3.5: Transmission of (a) probe field and (b) stokes field as functions of two-photon frequency difference between the control and probe field with (red) and without (blue) Raman pump-induced stokes absorption. All curves are normalized to the input probe field power. Raman pump power for both graphs is 220 mW. Here  $I_0$  and  $I_S$  are the heights of the probe transmission peak without and with the Raman pump, correspondingly.

To study the effect of the stokes field absorption on the EIT/FWM, we recorded the variation in the output probe and stokes field when Raman pump laser was introduced. The example of its effect on the output probe field is shown in Fig. 3.5. As expected, we see the reduction of the probe transmission peak when the stokes field is absorbed (we have verified that Raman pump field does not directly affect probe propagation). Note that the stokes absorption did not affect the width of the transmission resonances, indicating that the observed peak reduction was not due to the deterioration of the ground-state coherence.

To quantitatively characterize the effect of the Raman pump field, we calculated the suppression factor, defined as  $1 - \frac{I_S}{I_0}$ , where  $I_S$  and  $I_0$  are the heights of the probe transmission peaks values with and without Raman pump, correspondingly (see the exact definitions in Fig. 3.5(a)). Ideally, we would like to achieve unity suppression for the stokes field (i.e., no output stokes even at the two-photon resonance). Since we ran the exper-



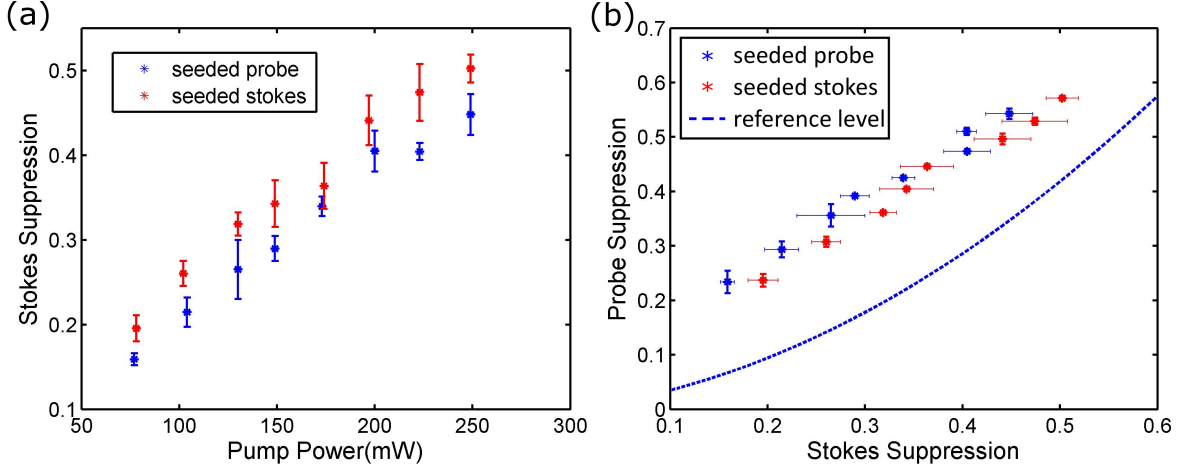


FIG. 3.6: (a) Suppression factor for stokes output field as a function of Raman pump power for EIT configuration. (b) Probe field suppression as a function of the stokes field suppression. The data shown in blue correspond to seeded probe field (no input stokes), while the red data points correspond to the seeded stokes fields (no input probe). Each data point corresponds to the average of five independent measurements, with the error bar equal one standard deviation. Dashed blue line corresponds to the reference reduction factor for the output probe field, if the input stokes field was attenuated *before* entering the vapor cell.

iment at rather high Rb density, we expect only weak transmission under the imperfect EIT conditions without FWM gain, and thus the probe suppression factor is expected to approach a value close to one.

The measured suppression factors for probe and stokes field as functions of Raman pump power are shown in Fig. 3.6. We see that stokes absorption increases (roughly linearly) with the Raman pump power and the probe attenuation was linearly proportional to the stokes attenuation. In addition to standard EIT arrangements, when a strong control field and a weak but nonzero probe field were injected into the Rb cell (no input stokes field), we also tested a configuration in which an optical field on the stokes frequency was injected, without any input probe field. In the latter case, only FWM contributed toward the probe field observed after the interaction with the atoms. For this configuration we observed qualitatively similar behavior, although for the same pump power the stokes

absorption was somewhat stronger. The limited available Raman pump power ( $< 250$  mW) did not allow us to reach the stokes field absorption beyond 50%, and corresponding probe suppression better than 60%. However, if we extrapolate the absorption data to the region of the higher pump powers, we can extrapolate that at a Raman pump power of  $\approx 380$  mW we should be able to achieve optical depth  $> 1$  for the stokes field.

In addition to inducing stokes absorption via Raman resonance inside the vapor cell, we also measured the reduction in the output probe field as function of the input seeded stokes attenuation. These measurements are shown as a reference in Fig. 3.6(b). It is easy to see that smaller probe suppression occurred in this case. The observed results can be explained by pointing out that in case of the seeded stokes its absorption can have two effects on probe. First, since the probe field is generated, its amplitude is proportional to the seeded stokes field, so weaker stokes is expected to produce less probe. This type of probe suppression should occur independently if the stokes field is attenuated before entering the cell or inside the interaction region. At the same time, additional stokes absorption can reduce the efficiency of the four-wave mixing, resulting in additional probe gain suppression, which maybe responsible for observed stronger suppression factor values in case of Raman absorption.

### 3.3 Off-resonant Raman case

Another configuration identified as a promising candidate for quantum memory applications is coherent Raman absorption of a probe field in a far-detuned  $\Lambda$  system [164, 169, 170]. This scheme also suffers from the effects of four-wave mixing noise [28, 36]. While our limited laser power and cw regime of laser operation did not allow us to test the exact range of parameters used in the Raman memory experiments, we replicated their experimental arrangements as closely as possible. In particular, we have detuned both control

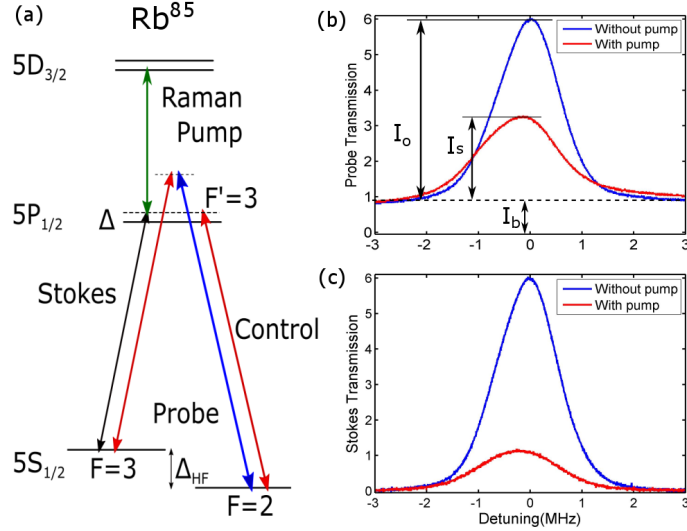


FIG. 3.7: (a) Level configuration used for the FWM suppression in the Raman configuration. The control field one-photon detuning from the  $F = 3 \rightarrow F' = 3$  transition is  $\Delta = 200$  MHz, and the Raman pump field wavelength is 762.1038 nm. (b, c) Examples of the two-photon resonances for the probe and stokes fields with and without Raman pump of 80 mW, correspondingly. All curves are normalized to the input probe field power. Here again  $I_0$  and  $I_S$  are the heights of the probe transmission peak without and with Raman pump, correspondingly, and  $I_b$  is the background level, corresponding to the probe transmission away from the two-photon resonance.

and probe fields away from the atomic resonances, adding a one-photon detuning on the order of the hyperfine splitting between the ground state levels, as shown in Fig. 3.7(a). In this configuration the control field frequency approached the  $F = 2 \rightarrow F' = 3$  transition, and the stokes field was generated near the  $F = 3 \rightarrow F' = 3$  transition. Unlike in the EIT case, discussed above, there was very little ( $< 10\%$ ) resonant absorption for the probe field. At the same time, the stokes field experienced a rather strong resonant absorption due to the proximity to the optical resonance. If only seeded stokes field was interacting with atoms, it was nearly completely absorbed. However, due to large FWM gain a significant generation (or enhancement) of the stokes field was observed after the Rb cell near the two-photon resonant conditions.

This configuration also allowed us to take advantage of the hyperfine structure of

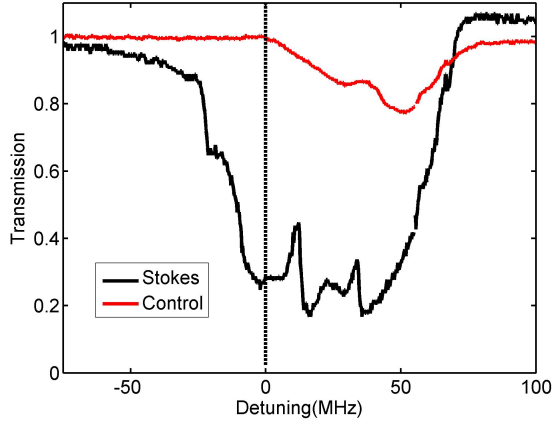


FIG. 3.8: Measured transmission for the stokes and control optical fields as the Raman pump frequency is scanned across the absorption resonances. Raman pump power is 80 mW. Vertical dashed line indicates the optimal operational frequency.

the  $5D_{3/2}$  state to fine-tune the Raman pump frequency to absorb the stokes field with minimal control absorption. Example absorption profiles for the control and generated stokes field under the two-photon resonance conditions are shown in Fig. 3.8. It is easy to see that the stokes absorption resonance, corresponding to the lowest pump frequency provides near-maximum stokes signal reduction, while keeping the control absorption less than 5%.

In this regime we were able to achieve much more significant levels of FWM suppression: nearly 95% attenuation for the output stokes field at the highest Raman pump power. This more efficient absorption was likely due to the closer proximity of the stokes frequency to that of the optical resonance. As a result, much higher suppression was observed for lower powers, reaching the absorption saturation near half of the maximum power level. In this configuration, we saw roughly the same amount of suppression for the stokes field when either probe or stokes were seeded. The suppression factor for the seeded probe was somewhat lower ( $\approx 60\%$ ) compare to the seeded stokes case ( $> 75\%$ ). This reduction was somewhat expected: in case of the seeded stokes field, any output

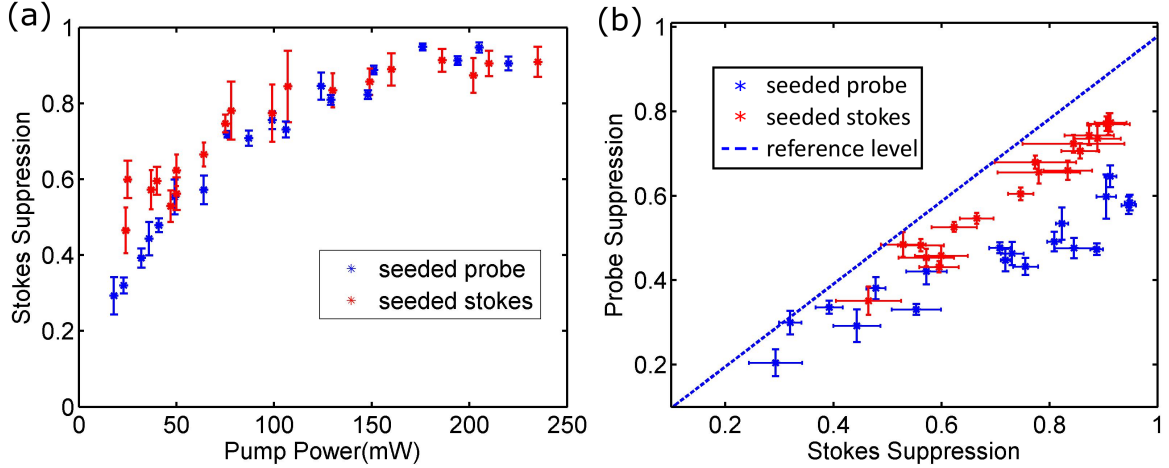


FIG. 3.9: (a) Suppression factor for stokes output field as a function of Raman pump power for far-detuned Raman configuration. (b) Probe field suppression as a function of the stokes field suppression. The data shown in blue correspond to seeded probe field (no input stokes), while the red data points correspond to the seeded stokes fields (no input probe). Each data point corresponds to the average of five independent measurements, with the error bar equal one standard deviation. Dashed blue line corresponds to the reference reduction factor for the output probe field, if the input stokes field was attenuated *before* entering the vapor cell.

probe field is generated via the four-wave mixing process, and in case of perfect FWM suppression should vanish completely, resulting in the unity suppression factor. However, for seeded probe we expect to see a non-vanishing two-photon EIT resonance even if FWM completely eliminated, leaving the final suppression factor value below one. We also note that in this Raman regime, the attenuation of the seeded stokes field either before or inside the cell gave similar generated probe suppression.

### 3.4 Conclusion

In this chapter, we demonstrated the possibility to use a ladder two-photon Raman absorption resonance to suppress four-wave mixing amplification of the probe field in a double- $\Lambda$  system under near-resonant EIT or far-detuned Raman conditions, the two interaction systems often considered for quantum memory experiments. We identified

several configurations in which a strong optical field tuned in the vicinity of  $5P_{1/2} \rightarrow 5D_{3/2}$  optical transition (762 nm) can produce narrow absorption resonances for the stokes optical field, generated in the four-wave mixing process. We showed substantial reduction in the output probe field when such resonances are introduced. Maximum four-wave mixing suppression in the EIT configuration, based on  $^{85}\text{Rb}$  atoms, was approximately 40% using the Raman resonance in  $^{87}\text{Rb}$  atoms. This value was limited by the available laser power. Same-isotope configurations were found as well, but either resulted in additional control field absorption, or required a significantly stronger Raman pump field. In case of the far-detuned Raman double- $\Lambda$  system, we achieved four-wave mixing suppression up to 85% in the same  $^{85}\text{Rb}$  isotope, thanks to the stronger achievable stokes absorption.

# CHAPTER 4

## Comparison of collimated blue light generation in $^{85}\text{Rb}$ atoms via the D1 and D2 lines

In this chapter, we report on the investigation of collimated blue light (CBL) generation in the two-photon transition reaching the  $5D_{3/2}$  state. By utilizing the four-wave mixing process (FWM), we can investigate the interference between competing excitation channels, spontaneous decays, and nonlinear processes [171]. It is important to understand this interplay to maximize the efficiency of a nonlinear processes, especially for coherent information transfer between systems [152]. It has potential for an alternative, more symmetric, four-wave mixing diamond scheme involving only near-IR optical fields [172–174]. Here, we experimentally compared the two excitation pathways to the  $5D_{3/2}$  level through either  $5P_{1/2}$  or  $5P_{3/2}$  intermediate levels and examine the interplay of a repumping field to identify the optimal conditions for the collimated blue light generation in each case.

## 4.1 Experimental arrangements

The schematic of the experimental apparatus is shown in Fig. 4.1. We employed three individual lasers. Two external cavity diode lasers – ECDL- $D_1$  and ECDL- $D_2$  – that are tunable in the vicinity of the Rb  $D_1$  line (wavelength 795 nm) and Rb  $D_2$  line (wavelength 780 nm). Each ECDL, depending on the stage of the experiment, can serve as either lower pump or re-pump laser while the upper pump optical field is generated using the continuous wave (cw) Titanium Sapphire (Ti:Sapph) laser. The first stage utilizes the  $D_1$  laser as the lower pump, the  $D_2$  as the re-pump, and the Ti:Sapph tuned to 762 nm (for  $5P_{1/2} \rightarrow 5D_{3/2}$  transition) while the second stage involves the  $D_1$  and  $D_2$  lasers swapping roles and the Ti:Sapph being tuned to 776 nm (for the  $5P_{3/2} \rightarrow 5D_{3/2}$  transition).

The two fields generated by the ECDLs were combined first so they could be adjusted together before combining with the Ti:Sapph laser. In order to further increase the laser intensities, the laser beams were weakly focused inside the Rb cell using a 1000 mm (L1) lens and then collimated using a 500 mm (L2) lens. All beams had gaussian intensity profiles with diameters 230  $\mu\text{m}$ , 250  $\mu\text{m}$ , and 840  $\mu\text{m}$  at the center of the Rb cell, for the  $D_1$ ,  $D_2$ , and Ti:Sapph laser beams, respectively.

For maximum flexibility in setting the pump field polarizations, all optical fields were combined using edge mirrors. We found that the polarization of the re-pump field relative to the lower pump field had very little effect on CBL generation, and thus we always matched the repump laser polarization to that of the lower pump field. The polarizations of the lower and upper pump fields, before entering the cell, were controlled independently using half- and quarter -wave plates. The polarizations of the individual beams were cleaned using beam splitters before they were combined. However, polarization imperfections could have risen from the use of zero-order waveplates designed for 795 nm light.



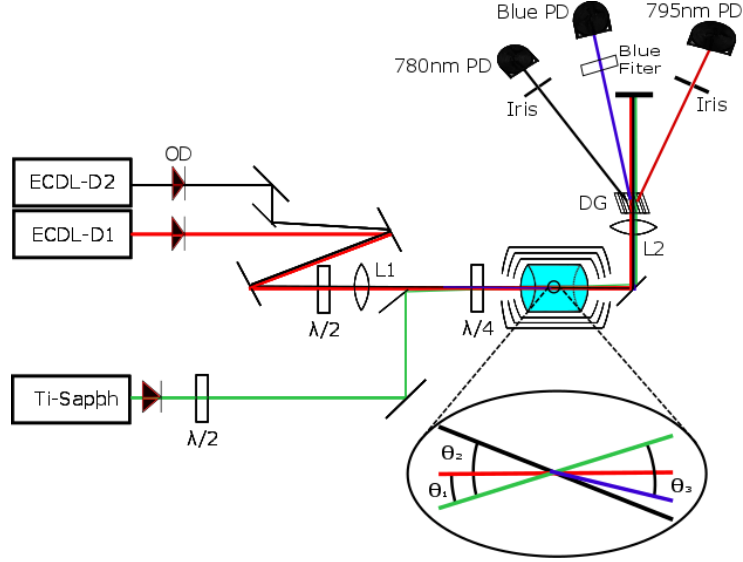


FIG. 4.1: The optical layout of the experimental setup. ECDL- $D_1$ , ECDL- $D_2$ , and Ti:Sapph denote three independent lasers used in the experiment. The optical paths of the  $D_1$ ,  $D_2$ , and Ti:sapph pump lasers and the generated blue light are show in, red, black, green, and blue, respectively. Inset shows relative orientation of the optical beams. See text for the abbreviations.

In the experiment we used a 75 mm - long cylindrical Pyrex cell (diameter 22 mm), containing isotopically enriched  $^{85}\text{Rb}$  vapor. The cell was tilted by approximately  $6^\circ$  to avoid the retroreflection effects from the cell's windows on the generated CBL [74]. For all the measurements the cell was maintained at a relatively low temperature of  $88^\circ\text{C}$ , corresponding to the  $^{85}\text{Rb}$  density of  $\approx 1.7 \cdot 10^{12} \text{ cm}^{-3}$ . The cell was housed in three layer magnetic shielding, with the innermost layer wrapped in a heating wire. Thermal insulation was placed between each layer of the magnetic shield to help with temperature stability.

Under these conditions we observed the emergence of collimated blue light. To maximize its power, we adjusted the relative angles between the two co-propagating pump laser fields and the repump laser as shown in the inset of the Fig. 4.1: all three beams were arranged in the same plane, with the angles between the Ti:Sapph laser and  $D_1$  and  $D_2$  laser beams being  $\theta_1 = 2.1 \text{ mrad}$  and  $\theta_2 = 7.5 \text{ mrad}$  correspondingly. The output

CBL beam then emerged at the angle of  $\theta_3 = 3.3$  mrad from the Ti:Sapph beam. We found that for both intermediate  $5P$  states, the generated blue light was produced at a wavelength of 421.7 nm (measured using an Ocean Optics spectrometer with spectral resolution  $\pm 0.2$  nm) corresponding to the  $6P_{1/2} \rightarrow 5S_{1/2}$  optical transition. We were not able to detect any directional radiation at the  $5D_{3/2} \rightarrow 6P_{1/2}$  and  $5D_{3/2} \rightarrow 6P_{3/2}$  transitions, since the glass cell is not transparent in the mid-IR spectral range. We also did not observe optical fields corresponding to the alternative relaxation pathways through the  $6S_{1/2}$  state [70, 71, 79] or  $5P$  states [173, 174].

To separate the CBL beam from the pump fields after the Rb cell, the output beams passed through a diffraction grating (DG) which directed  $\approx 46$  % of the total power of each field into the first diffraction order. We then used irises to isolate individual laser fields before the photodetectors (PD). To avoid contamination of the CBL measurements by any scattered IR laser light, we placed a blue spectral filter (transmission  $\approx 40\%$  at 421.7 nm) before the corresponding photo-detector.

## 4.2 CBL generation via the $D_1$ line

In this section we present the measurements in which the  $D_1$  transition ( $5S_{1/2} \rightarrow 5P_{1/2}$ ,  $\lambda_{D_1} = 795$  nm) served as the first step of the excitation scheme; the second pump laser with the wavelength 762 nm was used to further excite atoms into the  $5D_{3/2}$  excited state, as shown in Fig.4.2. In this configuration the  $D_2$  laser, acting as a repump, was tuned to the transition between the excited  $5P_{3/2}$  level and the ground-state hyperfine sublevel, not coupled by the  $D_1$  pump laser ( $F = 2$  in this case). Unless otherwise noted, all the reported data are recorded with the repump laser on, as it produced a uniform increase in the recorded CBL power, regardless of polarizations and powers of the pump lasers.

CBL generation was analyzed for four pump polarization configurations, in which

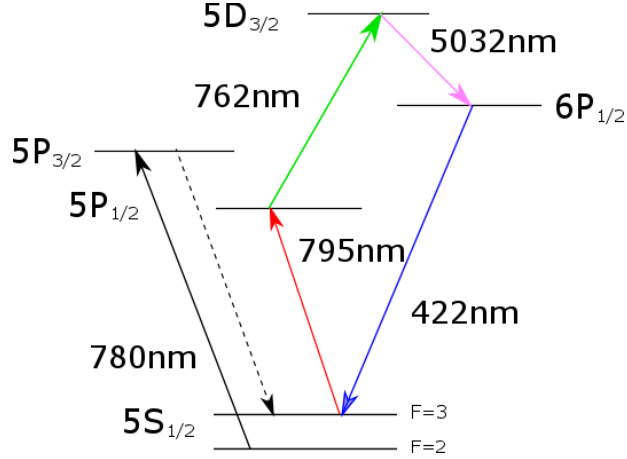


FIG. 4.2: Interaction configuration through the  $5P_{1/2}$  intermediate level: lower pump (795 nm) and the upper pump (762 nm) excite Rb atoms to the  $5D_{3/2}$  level, followed by the emission of  $5.032 \mu\text{m}$  (not detectable) and collimated blue light at 422 nm. The repump field is tuned to the  $5S_{1/2}, F = 2 \rightarrow 5P_{3/2}$  transition.

the two pump fields had either parallel or orthogonal linear or circular polarization. The resulting observations are shown in Fig.4.3, in which we plotted the CBL power for each polarization configuration as the function of the lower pump frequency (the upper pump frequency was fixed). We have considered three cases in which the lower pump laser was scanned across each hyperfine transition of the  $D_1$  line [Fig.4.3(a,b)], as well as when it was detuned by  $\approx +1.2$  GHz from the  $5S_{1/2}, F = 2 \rightarrow 5P_{1/2}$  [Fig.4.3(c)]. This detuning was chosen to be large enough to avoid resonant absorption for the lower pump field while still providing strong CBL output. Moving the pump frequencies farther from the optical resonances led to gradual decrease of the CBL power, without changes in its other characteristics.

We found that the polarization configuration leading to the maximum blue light generation was different, depending on the laser frequency. We detected the strongest CBL generation at the lower frequency transition ( $5S_{1/2}, F = 2, 3 \rightarrow 5P_{1/2}$ ) when the two pump field were linearly polarized, with parallel arrangement results in slightly higher CBL power. However, the circularly polarized pump fields produced a similar amount of

blue light for both the lower and higher-frequency transitions ( $5S_{1/2}, F = 3 \rightarrow 5P_{1/2}$ ), but since the blue output for the linearly polarized pumps dropped significantly in the latter case, the circular parallel pumps maximized the CBL generation. Finally, the circular orthogonal configuration led to the smallest generation of CBL. The variations in CBL output between different polarization arrangements originate, most likely, from the difference in Zeeman levels involved in the interactions and their transition strength, and will be further discussed in Sec. 4.4.

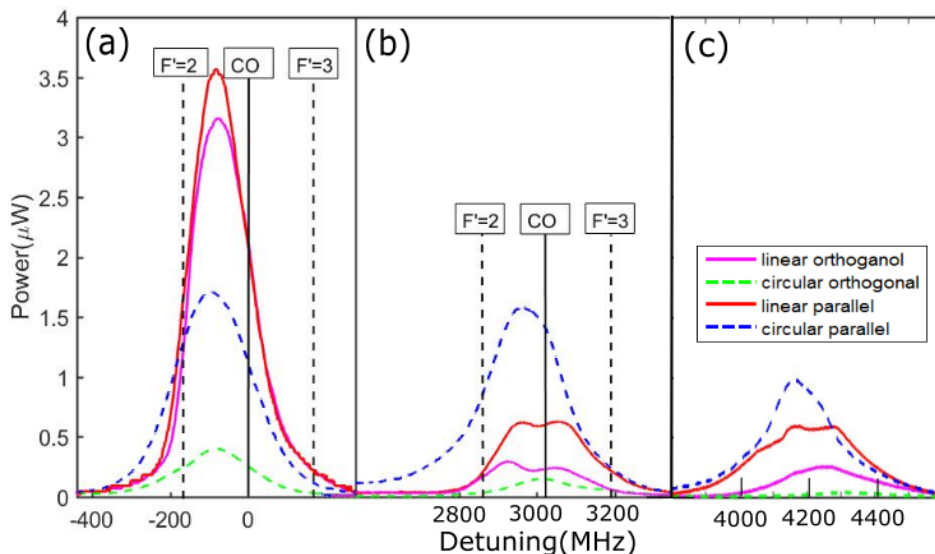


FIG. 4.3: Power of the generated blue light as the lower pump was swept across: (a)  $5S_{1/2}, F = 3 \rightarrow 5P_{1/2}$  transition, (b)  $5S_{1/2}, F = 2 \rightarrow 5P_{1/2}$ , and (c) 1.2 GHz above  $5S_{1/2}, F = 2 \rightarrow 5P_{1/2}$  transitions. The upper pump was tuned to 762.1036 nm for (a,b), and 762.1054 nm for (c). Four different polarization configurations of the two pump lasers are shown: linear parallel (red, solid line), linear orthogonal (magenta, solid line), circular parallel (blue, dashed line), and circular orthogonal (green, dashed line). The powers of both lower pump ( $D_1$  laser) and the repump ( $D_2$  laser) were kept at 16 mW, and the power of the upper pump (Ti:Sapph laser) at 200 mW. The zero detuning of the  $D_1$  pump corresponds to the cross-over transition of the  $5S_{1/2}, F = 3 \rightarrow 5P_{1/2}$  state.

We also analyzed the CBL polarization for linearly polarized pump lasers. We found that for all investigated laser detunings the polarization of the generated blue light matched the polarization of the lower pump field, even for orthogonally polarized laser fields. Unfortunately, we were not able to carry out the CBL polarization analysis for the circularly

polarized pumps since a quarter-wave plate for blue light was unavailable.

## On-resonant $D_1$ -line excitation

To investigate the power dependence of the generated blue light on all three involved laser fields, we considered on- and off-resonant tuning of the pump fields. In the first case, both pump fields were tuned near the centers of the corresponding optical resonant absorption peaks ( $5S_{1/2} \rightarrow 5P_{1/2}$  and  $5P_{1/2} \rightarrow 5D_{3/2}$ ). As CBL is the product of parametric wave mixing of two pump laser fields and the internally generated mid-IR field [44, 66], the maximum of the blue spectral profile did not always occur exactly at the two-photon resonance (in which the sum of the two laser frequencies exactly matched the frequency difference between the ground state and the excited  $D$  state), but was shifted toward the frequency corresponding to the maximum lower pump absorption and often resembled two poorly-resolved peaks. For the power dependence studies, seen in Fig. 4.4, we chose the lower pump detuning near the  $5S_{1/2}, F = 3 \rightarrow 5P_{1/2}$  transition and parallel linearly polarized pump fields which produced the highest CBL output.

At maximum power for all three fields, we measured  $3.5 \mu\text{W}$  of the generated blue light. As we decreased the power of the upper pump field, the CBL power dropped more or less linearly, as expected for the optically-driven population of the  $5D_{3/2}$  excited state [175]. The reduction of the repump power resulted in a similar nearly linear drop in CBL until leveling off at 30% of the repump power. It is likely that the effect of the repumping became negligible for lower repump laser powers due to its strong absorption, since the measured CBL power output (500 – 700 nW) matched the blue light generated in the complete absence of the repump field.

However, the lower pump power dependence is more complicated: as the  $D_1$  laser power increases, the CBL power grew steadily until it reached its plateau at  $4.25 \mu\text{W}$

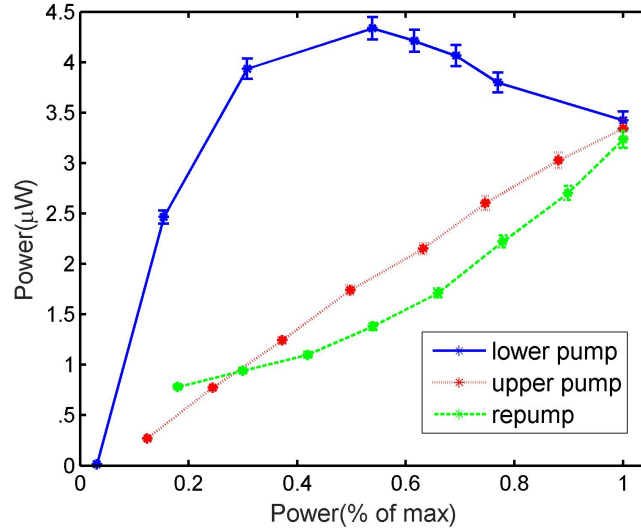


FIG. 4.4: Generated CBL power as a function of normalized power of each pump and repump fields. For each individual dependence the power of one laser was varied between zero and its maximum value, while the other two lasers were kept at their maximum powers: 65 mW for the lower pump (795 nm), 200 mW for the upper pump (762 nm), and 17 mW for the repump laser (780 nm). The laser detuning corresponded to the conditions for the maximum CBL power as shown in Fig. 4.3(a).

at  $\approx 50\%$  of the maximum available laser power ( $\approx 30$  mW), and then began to slowly decrease. The origin of such behavior is related to the optimization of excitation and relaxation rates from and to the ground state via stimulated processes, as will be discussed later in Sec. 4.4. We have verified that the resonant absorption of the  $D_1$  laser field displayed no similar trends, steadily decreasing from 70% to 40% with the growing laser power.

It also should be noted that the reduction in the generated CBL power at higher pump power occurred only when the repump field was present. Without the repump, the CBL reached saturation at the  $D_1$  field power of  $\approx 35$  mW, and then stayed roughly at the same level with further laser power increase. This can be interpreted as the shift of the CBL maximum toward higher pump power values, although we were not able to verify that due to the power limitation.

## Off-resonant $D_1$ -line excitation

CBL power dependences were also analyzed for the pump fields detuned by approximately +1.2 GHz from the  $5S_{1/2}, F = 2 \rightarrow 5P_{1/2}$  transition [Fig. 4.3(c)]. At this detuning the lower pump field experienced almost no resonant absorption making the contribution of the step-wise excitation process significantly smaller compared with the direct two-photon excitation. Thus, we observed the maximum blue light generation at the two-photon resonance conditions for the  $5S_{1/2} \rightarrow 5D_{3/2}$  transition. We chose to use the linear parallel polarizations arrangement for direct comparison with the resonant case. As one can see in Fig. 4.5, in this case the blue light power displays fairly linear dependence on each pump laser field, without reaching saturation or maximum. The repumping power dependence is also qualitatively similar to the resonant case, although it is important to note significantly higher enhancement for the same repump power ( $\times 10$  CBL power increase) compare to the resonant case ( $\times 4$  CBL power increase).

## 4.3 CBL generation via the $D_2$ line

The alternative excitation pathway to the  $5D_{3/2}$  level is through the  $5P_{3/2}$  intermediate level. In this case, the two-photon transition was executed using the  $D_2$  (780 nm) laser and the Ti:sapph laser, tuned to the 776 nm, while the  $D_1$  (795 nm) laser served as the repump, as shown in Fig. 4.6. This pump configuration is traditionally used for the excitation of Rb atoms into the  $5D_{5/2}$  state [65–67, 69–71]. Under the identical experimental conditions, we have obtained up to 120  $\mu\text{W}$  of blue light using the  $5S_{1/2} \rightarrow 5P_{3/2} \rightarrow 5D_{5/2}$  excitation scheme, while in the case of the  $5S_{1/2} \rightarrow 5P_{3/2} \rightarrow 5D_{3/2}$  pathway the maximum obtained CBL power was just  $\leq 450$  nW.

Fig.4.7 demonstrates the measured CBL output power as a function of the lower pump

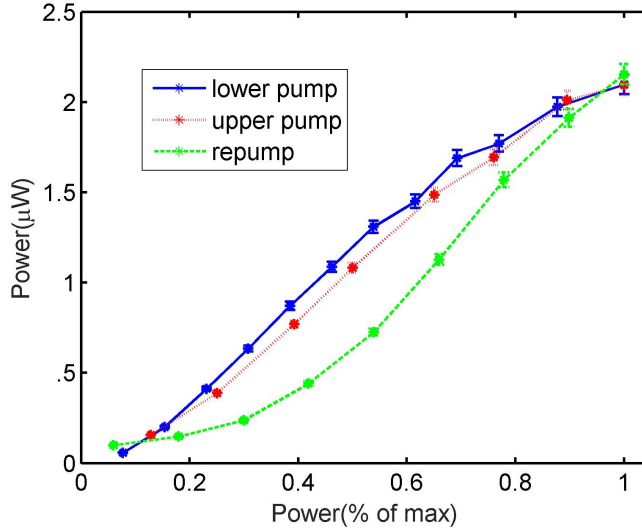


FIG. 4.5: Generated CBL power as a function of normalized power of each pump and repump field. As in Fig. 4.4, for each individual measurement the power of one laser was varied between zero and its maximum amount, while the other two lasers were kept at their maximum powers: 65 mW for the lower pump (795 nm), 200 mW for the upper pump (762 nm), and 17 mW for the repump laser (780nm). The laser detuning corresponded to the conditions for the maximum CBL generation in Fig. 4.3(c), approximately +1.2 GHz blue of the  $5S_{1/2}, F = 2 \rightarrow 5P_{1/2}$  transition.

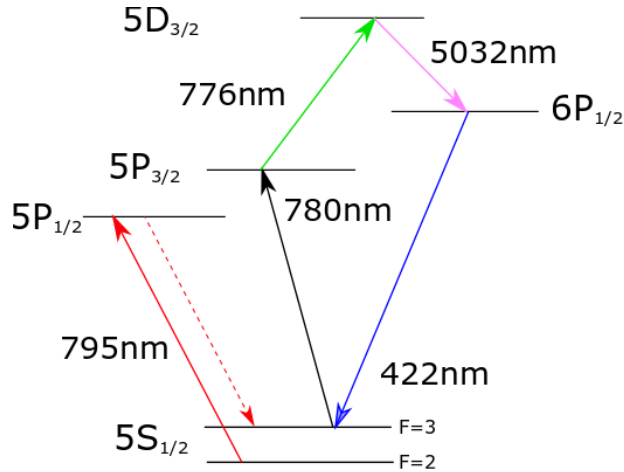


FIG. 4.6: Interaction configuration for CBL generation via the  $5P_{3/2}$  intermediate state, that uses the lower pump (780 nm) and the upper pump (776 nm) to excite Rb atoms into the  $5D_{3/2}$  state, resulting in emission of  $5.032 \mu\text{m}$  (not experimentally observed) and collimated blue light (422 nm). The repump (795 nm) field is tuned to the hyperfine ground state opposite of the lower pump.



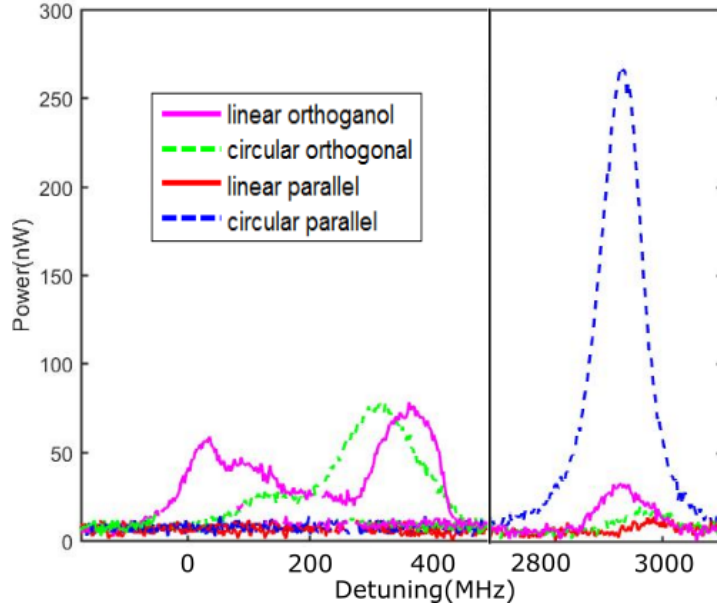


FIG. 4.7: Measured CBL power for varying polarizations of lower pump (780 nm) and upper pump (776.1568 nm) as the lower pump is swept across the hyper-fine split ground states. The considered polarization arrangements for the two pumps are: linear parallel (red, solid line), linear orthogonal (magenta, solid line), circular parallel (blue, dashed line), and circular orthogonal (green, dashed line).

( $D_2$ ) laser detuning, from the  $F = 3$  ground state, for the previously tested four polarization combinations, shown in Fig. 4.3. We observed an even more pronounced dependence of the blue light power on the pump polarizations than in the  $D_1$  excitation scheme. For the two-photon  $5S_{1/2}, F = 2 \rightarrow 5D_{3/2}$  transition, the parallel circularly-polarized pump fields yielded CBL output that was stronger than the other three configurations by at least an order of magnitude. Remarkably, the same pump polarization arrangement produced no CBL when the lower pump was tuned to the other hyperfine ground state  $5S_{1/2}F = 3$ . At that frequency the blue light was detected only for the circular orthogonal and linear orthogonal polarizations. The observed polarization dependence, as well as the variation of the pump frequency corresponding to the maximum CBL for different polarization arrangement, is most likely due to rich Zeeman structure of multiple hyper-fine excited states.

Overall, we found significantly weaker (approximately by a factor of 10) blue light generation, compare to the  $D_1$  excitation scheme. Also, the blue light power dropped very rapidly with the laser detuning away from the resonance, so that no detectable CBL output was found at +1.2 GHz detuning used for the off-resonant case in previous section.

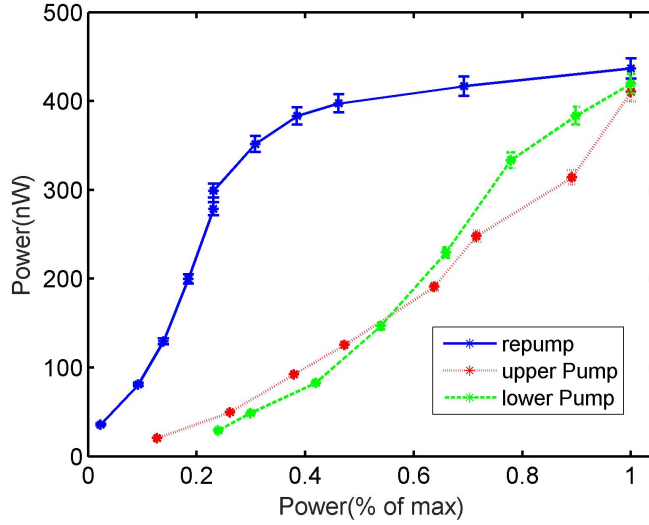


FIG. 4.8: Generated CBL as a function of normalized power of the pump and repump fields. As in Fig. 4.4, for each individual dependence, the power of one laser was varied between zero and its maximum value, while the other two lasers were kept at their maximum powers: 17 mW for the lower pump (780 nm), 200 mW for the upper pump (776 nm), and 65 mW for the repumper (795 nm). The laser detuning corresponded to the conditions for the maximum CBL generation in Fig. 4.7(b), near  $S_{1/2}F = 2 \rightarrow 5P_{3/2}F'$  transition. The upper pump wavelength was fixed at 776.1568 nm.

Fig. 4.8 shows the dependences of the CBL power on the power of the pump and the repump lasers, measured for parallel circular polarization of the pumps, the configuration yielding the highest CBL powers. When either pump power was varied, we observed a roughly linear dependence for the blue light output. Unlike the resonant excitation using the  $D_1$  optical transition shown in Fig. 4.4, no signs of saturation or peaking was observed at the available range of the lower pump ( $D_2$  laser) power. It is important to note, however, that we operated with less available laser power. In the case of the  $D_1$  excitation channel, the CBL power started to saturate at around 12 mW of the lower pump power, reaching

the maximum value at 35 mW. Since the maximum available  $D_2$  laser power was only 17 mW, it is possible that nonlinear power dependence can be observed at higher pump powers.

The repump power dependence shows clear saturation for the  $D_1$  laser powers above  $\approx 20$  mW, the power level necessary to provide efficient depopulation of the  $5S_{1/2}F = 3$  ground state. Unsurprisingly, further repump power increase did not provide any additional advantages. We confirmed this by the additional measurements of the  $D_2$  laser resonant absorption, observing an increase in absorption from 30% without the repump to a plateau of  $\approx 50\%$  with repump power above 20 mW.

## 4.4 Simplified theoretical simulations

To gain some qualitative understanding of the observed experimental behavior, we built a simplified theoretical model of the blue light generation using the methodology described in Ref. [176] adopted for in a four-level diamond scheme. To reduce the complexity, we have neglected the nuclear spin, eliminating the hyperfine structure. To account for alternative spontaneous decay paths and the optical pumping of atoms in the second ground hyperfine state, we introduced an additional fictional non-degenerate ground state. Lifetime and branching ratios of which, match those of the corresponding Rb states. We also do not account for the Doppler broadening of the optical transition due to the thermal motion of the atom, but incorporate the ground-state decoherence rate of 1 MHz, mimicking the transient relaxation.

Despite many simplifications, the calculations qualitatively match the experimental observations and provide explanation for the observed behaviors. Fig. 4.9(a) demonstrates the dependences of the CBL gain on the powers of the pump lasers in the range of Rabi frequencies comparable with those used in the experiment. The simulated trends are

similar to the experimental dependencies, shown in Fig. 4.4, in which the CBL power grows with the upper pump, but reaches a maximum and then declines when the lower pump power is increased. However, if we allow either pump power to vary at a larger range, as shown in Fig. 4.9(b), we see that the maximum CBL output occurs when the upper to lower pump Rabi frequencies ratio is roughly 2.3. An increase of either pump power leads to a reduction of the populations of the atomic levels, involved in blue light generation and consequently to the reduction of CBL output. In particular, we observe that too powerful lower pump laser leads to the gradual population of the uninvolved ground state sublevels, the process only partially amendable with the optical repumping. In contrast, increase of the upper pump beyond the optimal value depopulates the intermediate excited state, reducing the  $5D$  state population and consequently the FWM amplification.

This understanding also helps in explaining the difference in the CBL output dependence on the lower pump power at  $D_1$  and  $D_2$  lines, shown in Figs. 4.4 and 4.8. Since the  $D_1$  laser output is higher, we were able to realize the optimal power ratio for the lower and upper pumps and observed the CBL maximization. However, if the maximum value of the  $D_1$  pump was used, we were not able to reach the optimal CBL conditions due to power limitation of the Ti:Sapph laser. However, when we tested the alternative configuration through the  $5P_{3/2}$  state, the mismatch between the available powers of the two pumps restricted the CBL generation to the lower part of the theoretical curve.

We also calculated the dependence of CBL yield on the repump laser strength. As expected, efficient repumping of atomic population from uncoupled ground state magnifies the CBL gain significantly, reaching saturation. This is qualitatively the same behavior as observed experimentally in Fig. 4.8, when the more powerful  $D_1$  laser served as a repumper. Because of the lower maximum available output of the  $D_2$  laser and its stronger resonant absorption, we did not achieve such saturation when it was used for repumping, and the corresponding line at Fig. 4.4 resembles the lower end of the simulated curve.

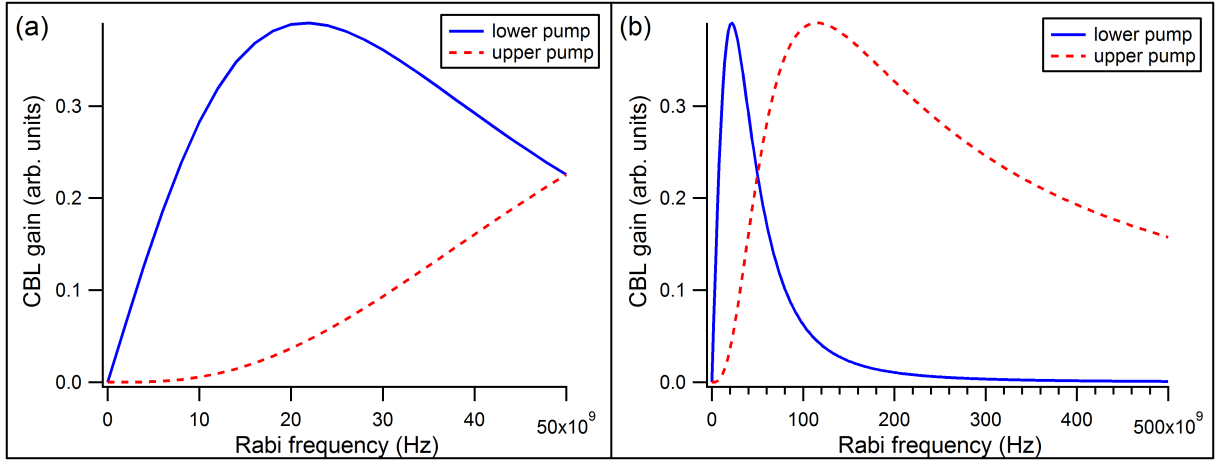


FIG. 4.9: Calculated CBL gain as a function of either pump Rabi frequency. While the Rabi frequency of one of the pump fields is varied, the other is maintained at its maximum value of  $5 \times 10^{10}$  Hz. In (a) the Rabi frequencies change in the range similar to those used for experimental data in Fig. 4.4. In (b) the range of variation is increased by a factor of 10 to display the more complete power dependence. For these simulations we used parallel circular polarizations for all optical fields; however, the same general behavior is observed for other polarization configurations.

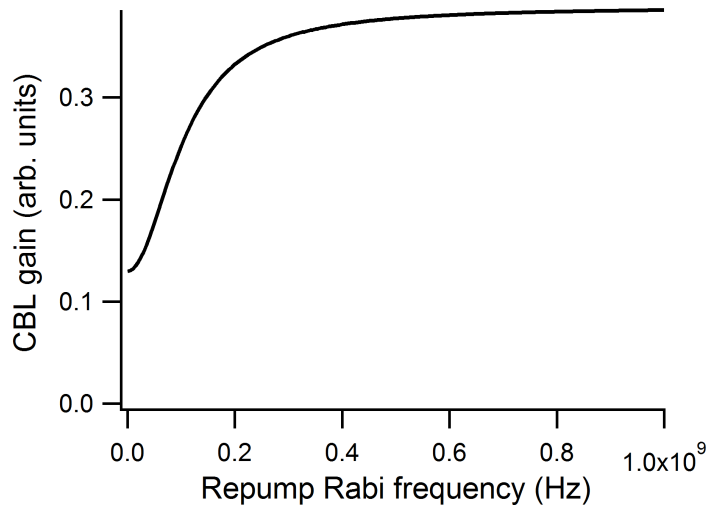


FIG. 4.10: Calculated CBL gain as a function of repump Rabi frequency. For these simulations we used parallel circular polarizations for all optical fields, and the Rabi frequencies of the lower and upper pump fields of  $2 \times 10^{10}$  Hz and  $5 \times 10^{10}$  Hz, corresponding to the calculated maximum CBL gain.

Finally, we can check the effect of the polarizations of the pump fields. Fig. 4.11 presents the results of the simulations of CBL gain for the four polarization configurations tested in the experiment. While inclusion of accurate Zeeman and hyperfine atomic structure is necessary to match the experimentally measured dependences, the simplified simulations still display some general features, characteristic to the observations. For example, in the simulations for both linearly and circularly polarized pump fields, larger CBL gain is observed when the two pumps have parallel, rather than orthogonal. We also verified that the observed changes in CBL strength for different polarizations is general, and not specific for particular values of pump powers. For that we replicated the CBL gain dependence on the lower pump Rabi frequency, shown in Fig. 4.11(b).

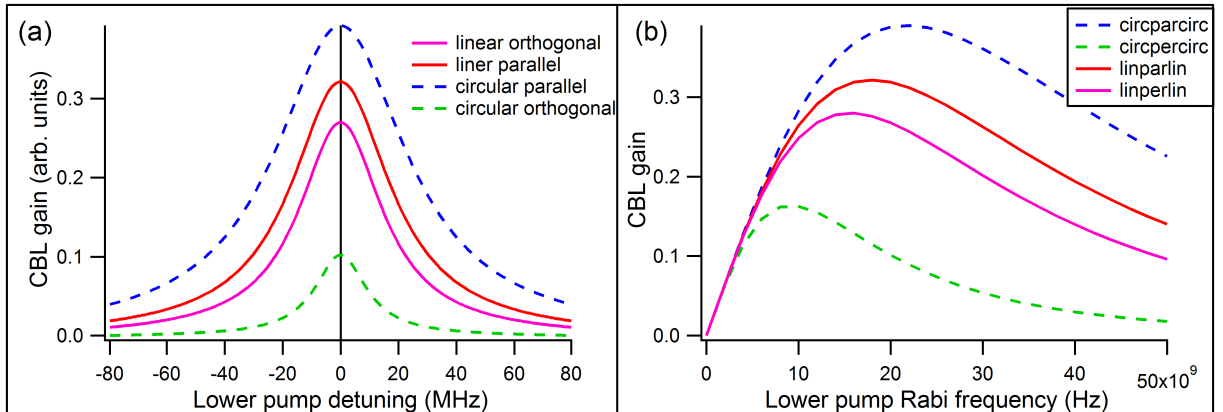


FIG. 4.11: (a) Calculated CBL gain as a function of lower pump frequency for the four polarization arrangements tested in the experiment. For these simulations the Rabi frequencies of the lower and upper pump fields of  $2 \times 10^{10}$  Hz and  $5 \times 10^{10}$  Hz, and the upper pump was resonant with the corresponding optical transition. (b) Modification of the CBL gain lower power dependence for different polarization arrangements. The simulation parameters are identical to those using in Fig. 4.9.

## 4.5 Conclusion

In conclusion, we report on characterization of the collimated blue light generation via two-photon excitation from the  $^{85}\text{Rb}$   $5S_{1/2}$  ground state to the  $5D_{3/2}$  excited state

through either  $5P_{1/2}$  or  $5P_{3/2}$  intermediate levels. We have studied the characteristics of the generated blue light for various pump laser frequencies, and found that the polarization arrangement leading to the maximum CBL power output strongly depends on the optical transitions used. This indicates the importance of selection rules and individual Zeeman transition probabilities. The experimental results shared various qualitative characteristics with the theoretical simulation. We found that under the optimized experimental conditions the blue light output was noticeably stronger when the  $D_1$  optical transition was used as the first excitation step. In the case of the  $D_1$  resonant excitation we demonstrated the existence of the optimal pump powers that led to maximum blue output. For other situations (off-resonant  $D_1$  excitation or resonant  $D_2$  excitation) a linear dependence of output CBL power on the lower pump power was detected. Theoretical simulations allow us to explain this behavior: for each set of experimental parameters there seems to be an optimal ratio between the lower and upper pumps that lead to maximum CBL yield. Any deviations from this value result in sub-optimal population redistribution between the involved atomic transitions, and in the reduction of blue light generation. In case of the  $D_1$  resonant excitation we were able to realize such optimal conditions for the lower pump power. For the other configurations, however, we were limited to the initial rising power dependence, before the CBL maximum was reached. Our measurements and simulation also demonstrated the importance of the repumping of atomic population from the uncoupled ground state sublevels, that led to an order of magnitude increase in blue light generation in all tested configurations. A more detail simulation and further study may shed light on the specific temperatures, powers, and polarizations for a better optimized and efficient CBL generation.

# CHAPTER 5

## Experimental Generation of FWM Squeezing

In this chapter, we will discuss the different experimental components which go into generating two-mode squeezed light via FWM. This will be the central focus for the remaining experiments in this thesis and the following chapters will build upon the experimental principles defined here. There are some key aspects to consider when generating squeezed light. In sec. 5.1, we will begin by discussing the preparation of the pump and probe fields necessary to produce FWM. The method is similar to the one in Ch. 3, but with a different laser system and parameters. In sec. 5.3, we will discuss the propagation of the beams in the cell and phase matching conditions which govern the FWM process. Finally, in sec. 5.4, we will discuss the filtering of the pump field and the detection of intensity difference squeezing. The schematic is shown below in Fig. 5.1



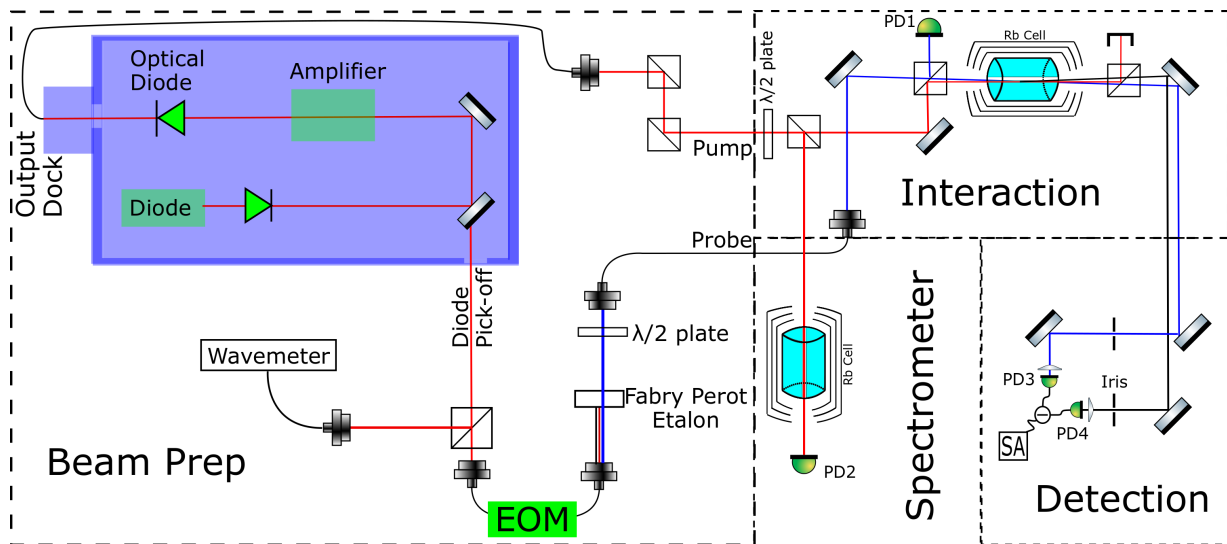


FIG. 5.1: Full schematic for the generation and detection of squeezed light via FWM

## 5.1 Beam Preparation

The probe and pump beams are generated by using a single continuous wave diode laser system, the Toptica TaPro795. The output of this system is tunable between 775 nm and 805 nm and has two output ports. One is a pick-off from the laser diode (will become the probe) and the other is the output from the tapered amplifier (will become the pump), shown in Fig. 5.2. Generating both the probe and pump from the same system will ensure the phase coherence between the two beams necessary to generate squeezed light from FWM.

The pick-off from the diode is first split into two parts using a polarizing beamcube, the vertical polarization is fed into a Bristol wavemeter to monitor the frequency of the pump and the horizontal polarization (4.5 mW) is coupled into a fiber electro-optical modulator (EOM) and modulated at 3035 MHz (hyper-fine splitting of  $^{85}\text{Rb}$ ). We use a Marconi Instruments 2031 RF source to control the EOM and supply it with a frequency output of 1517.5 MHz at -1.5 dB which is then frequency doubled and amplified. The output of the EOM is then filtered using a Fabry-Perot etalon set to transmit the low frequency side-

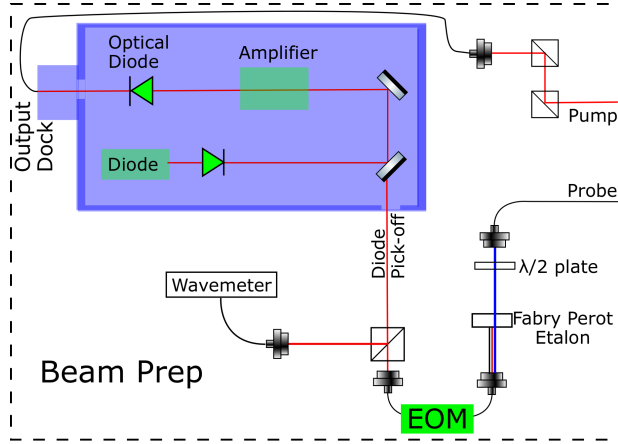


FIG. 5.2: This is the cutout of the beam prep which generates the probe and pump fields.

band (3.035 GHz shifted down from the frequency of the pump field). This is the probe optical field, which is then passed through a fiber to clean the transverse intensity profile and then output to the interaction portion of the experiment with a power of  $70 \mu\text{W}$ , as shown in Fig. 5.1. We can monitor the probe signal using a photodetector (PD1) in Fig. 5.1, with appropriate filtering of the leaked pump field. The pump is the direct output from the tapered amplifier, coupled into the Toptica fiber-dock system. The fiber output polarization is cleaned further using two polarizing beam splitters (PBS). The amplifier is driven at a current of 1.5 A and results in a power of 380 mW, laser schematic shown in Fig. 5.2.

## 5.2 Beam Monitoring

We monitor the frequency of our beams by using a Bristol wave meter and ensure that the pump frequency is set to 794.9725 nm. This frequency was selected by optimization the incident angle of the beams, single- and two-photon detunings, pump field power, and cell temperature [8, 98]. These various parameters control the amplification of the probe field and the generation of the conjugate field and are optimized for maximum gain and

squeezing.

The single-photon detuning sets the proximity from the atomic transition. The optimal condition for this parameter does not align with maximum gain [98]. This is due to the absorption of the probe field by the atoms, as it is generated, which results in the correlations between it and the conjugate field being destroyed and leading to additional noise. For this reason, we set to 1 GHz away from the atomic transition. We confirm the absence of probe absorption with the spectroscopy setup, shown in Fig. 5.3 (a). By tuning the etalon and EOM in Fig. 5.2, we can tune the probe frequency until we do not see an absorption. The output signal of the etalon is shown in Fig. 5.3 (b) and monitored by PD1. The absorption spectroscopy signal is monitored by PD2 and shown by the blue curve in Fig. 5.3 (b). Both are obtained by sweeping the pump laser.

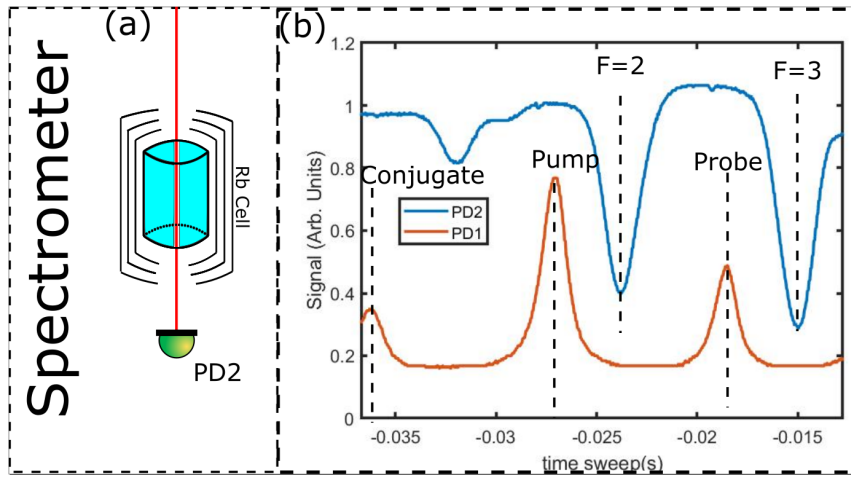


FIG. 5.3: (a) The absorption spectroscopy setup. (b) The oscilloscope trace, blue is signal for the absorption spectroscopy of an Rb natural abundance cell and red is the output of the EOM filtered by the etalon as the laser frequency is swept.

These measurements are also useful for monitoring our equipment. The absorption spectroscopy signal can point to the mode characteristics of the laser. If it is operating in a multi-mode regime or if the alignment into the amplifier for the pump is incorrect, the absorption features shown in Fig. 5.3 (b) by the blue curve begin to wash out with noise and unexpected sharp features will appear. PD1 is used to monitor the probe signal

while the pump is in use. It gives the same signal as PD3 with the pump blocked. This is necessary to monitor the operation and stability of the EOM. In the event the RF source is malfunctioning, the sidebands shown by the red trace in Fig. 5.3 (b), will vanish and only one peak will be seen.

### 5.3 FWM and the Phase Matching Conditions

In the interaction portion, the pump and probe optical fields were combined at an angle of  $\approx 0.4^\circ$  using a polarizing beam splitter (PBS) before entering a 25-mm long Pyrex cell filled with isotopically enriched  $^{85}\text{Rb}$  vapor, shown in Fig. 5.4 (a). The cell was mounted inside of a three-layer magnetic shielding and maintained at  $106^\circ\text{C}$  corresponding to the atomic density of  $7 \cdot 10^{12} \text{ cm}^{-3}$ .

After the cell, we observe the amplified probe field and the newly generated conjugate field. This interaction has two main features that we track, the gain and squeezing from FWM. The optimization for this was discussed in Sec. 5.2. The two features are tracked by measurement of the differential intensity using the balanced detection shown in Fig. 5.6 (a). By blocking one of the ports of the balanced detector, we can measure the power in of either the probe or conjugate beam in the DC coupled output of the detector. By not blocking either beam, we make a measurement of the differential intensity noise and thus squeezing via the AC coupled output of the balanced detector to a spectrum analyzer (SA). A sample SA signal is shown in Fig. 5.6 (b).

The gain from FWM and the level of squeezing are optimized by three main parameters; the single-photon detuning  $\Delta$  (pump frequency), two-photon detuning  $\delta$  (EOM modulation), and the relative angle of the probe and pump ( $\theta_1$ ), shown in Fig. 5.4 (a). The general settings were determined by the conditions in [8] and are as follows: an angle of  $0.4^\circ$  between the pump and the probe beam, a two-photon detuning of -1 MHz

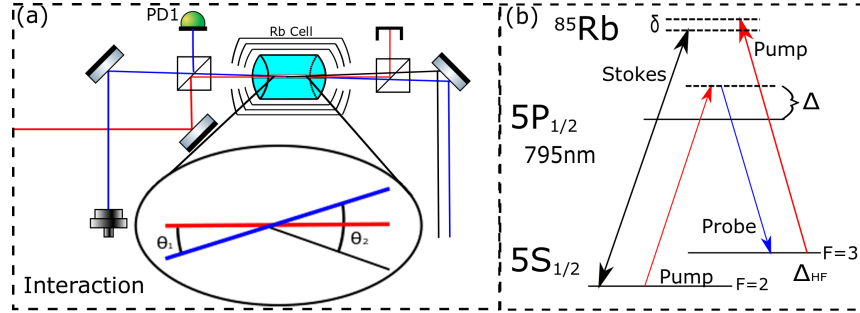


FIG. 5.4: (a) is the interaction in the cell with phase matching angles shown and (b) is the FWM level diagram for generating squeezed light where  $\Delta_{HF}$  is the hyper-fine splitting.

(EOM modulation 3035 MHz), and a single-photon detuning of  $\Delta \approx 800\text{MHz}$  from the  $^{85}\text{Rb}$   $5P_{1/2}$  resonance. However, the optimization requires simultaneous adjustment of all parameters and the tuning of a single parameter is not enough.

The effect the multiple parameters in play becomes clear when the beams have a more complicated mode structure, shown in Fig. 5.5. In this case, we impart optical angular momentum onto the input probe field and observe that the amplification is spatially dependent on the two-photon detuning. As we tune this, the shape of the probe (left) and the conjugate (right) beams also change due to the phase matching conditions. Consequentially, the squeezing also becomes worse. However, as will be shown in Ch. 6, we can adjust the angle of incidence of the probe relative to the pump to supplement the phase matching conditions to restore the shape and help improve the squeezing. This shows that the profile of the amplification can give insight to finding a good alignment for squeezing.

## 5.4 Pump Filtering and Intensity Difference Squeezing Detection

While alignment and frequency play an important role in generating squeezed light, the detection might be even more vital. The first demonstration squeezing, by Slusher

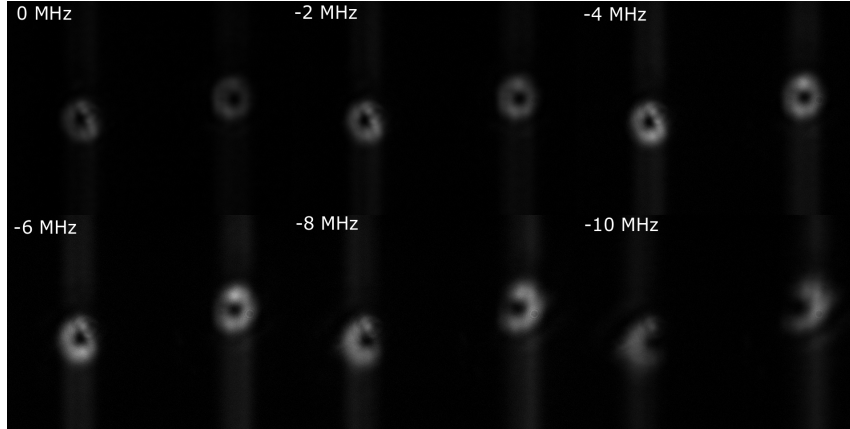


FIG. 5.5: The probe (left) and conjugate (right) OAM mode structures as a result of FWM and the effects as the two-photon detuning is changed.

et.al. [82], showed that squeezing was drastically limited by losses. To avoid them, we minimize the number of optical elements en route to detection. Losses are detrimental since they remove photons from the probe and conjugate fields at random and introduce vacuum fluctuations into the two beams, resulting in squeezing reduction. This squeezing is defined by the beam splitter model [156]

$$SqV_{out} = 10 \cdot \log_{10}[T \cdot 10^{SqV_{in}/10} + (1 - T)] \quad (5.1)$$

where  $T$  is the transmission through the elements.

After interaction in the cell, the pump is filtered using a polarizing beam cube with an extinction coefficient of  $\approx 10^3$ . The probe and conjugate fields are then separated using an edge mirror and then each beam passes through an iris to spatially filter any remaining pump. This filtering seems like a small step, however it is one of the most crucial to observe squeezing and the setting of the iris plays a large role in squeezing quality.

At the final stage, small focus lenses are used to focus the beams onto PD's 3 & 4. This is done to make sure the entirety of the beam is being detected since any loss would further limit squeezing. In addition to this, the lenses allow for slight adjustments to

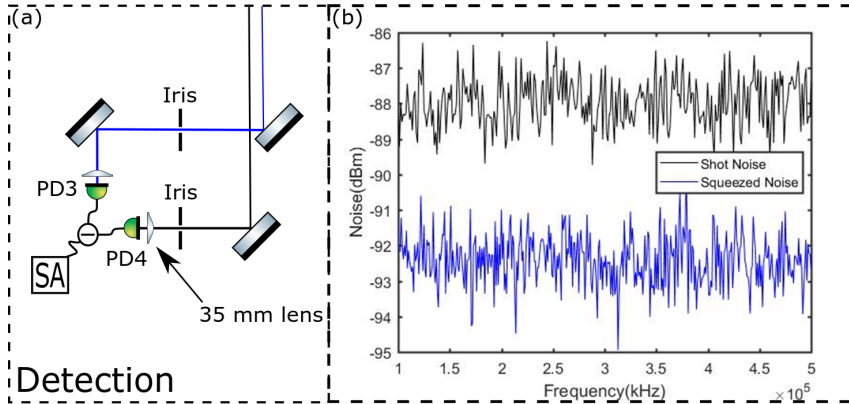


FIG. 5.6: (a) The detection portion of the schematic. (b) The output from the spectrum analyzer.

probe and pump alignment while not needing to adjust the alignment into the detection apparatus. The noise in the differential intensity is monitored by using the AC output coupling of the differential detector fed to a HP 8596 B spectrum analyzer.

The experiments in Ch. 6 and 7 use settings (a). Settings (b) are used for the experiment in Ch. 8. The readout from the spectrum analyzer is usually acquired for detection frequencies in the range of 100 kHz to 500 kHz, shown in Fig. 5.6 (b). We measure the differential noise of the squeezed twin-beams as the detection frequencies are scanned. In this graph, shot noise is plotted as black and the noise from the squeezed light is plotted in blue. The shot noise is obtained by using a portion of the pump beam split in two with a polarizing beam displacer and a half-wave plate, as shown in Fig. 5.7 (a). This sends half the pump to each port of the balanced detector, from which we can measure the classical noise for different powers of the pump field. Rather than doing this for every measurement, we make a calibration of signal to noise, shown in Fig. 5.7 (b). The calibration will change depending on the spectrum analyzer settings.

In Fig. 5.6 (b), we see that the noise of the squeezed fields is 4 dBs lower than that of shot noise. This is a factor of 2.5 reduction in the noise power. In the proceeding experiments, to obtain squeezing values, we measure trace from the SA five consecutive

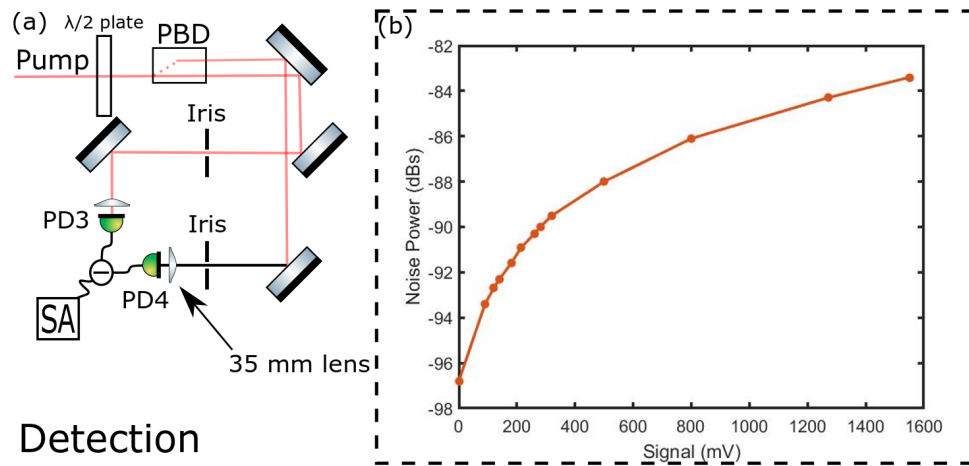


FIG. 5.7: (a) The shot noise measurement method for the apparatus. (b) The calibration of the spectrum analyzer noise.

times and average to obtain our value and take the standard deviation to obtain our error-bars.



# CHAPTER 6

## Optical Angular Momentum manipulations in a Four Wave Mixing process

In this chapter, we utilize the FWM process to extend the parameter space of accessible OAM modes by independently implanting OAM on both the pump and probe optical fields. We demonstrate that, despite considerable differences in spatial profiles of the generated probe and Stokes fields, we observed comparable levels of quantum intensity correlations.

To achieve high four-wave mixing gain and a high level of intensity correlations between the probe and Stokes fields, the two input optical fields must cross inside the Rb cell at the proper angle. The Stokes field is then generated symmetrically with respect to the output pump beam, following the phase matching conditions  $\vec{k}_{\text{probe}} + \vec{k}_{\text{Stokes}} = 2\vec{k}_{\text{pump}}$ . If either input optical field carries optical angular momentum, the OAM phase-matching con-

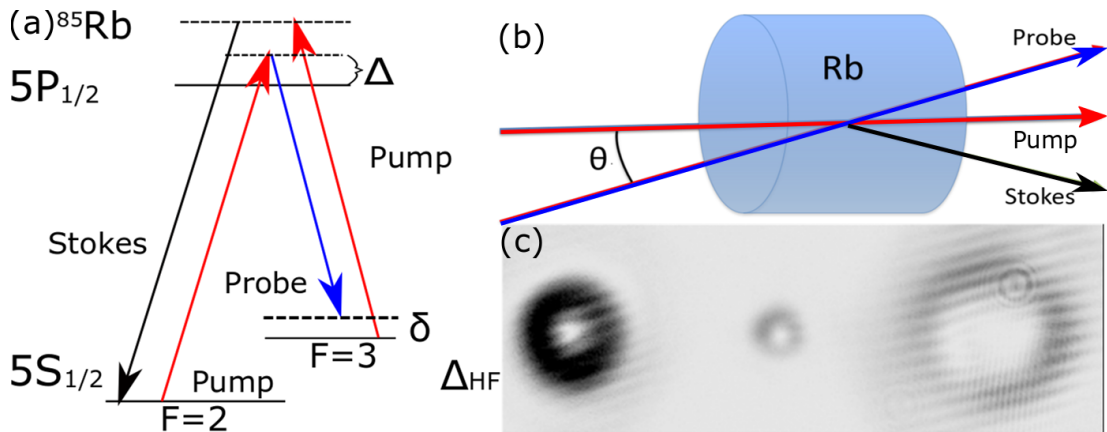


FIG. 6.1: Realization of the four-wave mixing in  $^{85}\text{Rb}$  vapor: (a) level diagram and (b) geometrical arrangement. (c) Example of the output probe (left) and generated stokes (right) field with mutual difference of  $\Delta\ell = 4$ .

dition dictates the topological charge of the generated Stokes field, as defined in sec. 2.4.3:

$$\ell_{\text{Stokes}} = 2\ell_{\text{pump}} - \ell_{\text{probe}}. \quad (6.1)$$

Thus, it should be possible to produce the Stokes field carrying OAM in a significantly broader range than if only one of the input beams carried OAM [8]. As an example, Fig. 6.1(c) shows the Stokes field with  $\ell_{\text{Stokes}} = -3$  that is generated using probe and pump fields carrying the unit topological charges of the opposite sign ( $\ell_{\text{probe}} = +1$  and  $\ell_{\text{pump}} = -1$ ). This results in the topological charge difference of  $\Delta\ell = 4$  between the two quantum correlated optical fields. Yet, as we will show in the following sections, such manipulations of the spatial beam profiles do not cause significant deterioration of the quantum correlations between the two fields. Moreover, we found that the four-wave mixing process allows for the usage of an optical field with a composite vortex structure to increase the total effective topological charge of a beam. Specifically, we used a phase mask, which added two closely-separated, but clearly distinguishable, unit charge vortices to the input pump field. By analyzing the generated Stokes field, we unambiguously demonstrate that its OAM value is consistent with the total OAM carried by the pump field, rather

than with that of an individual vortices. These observations suggest that FWM can be used as a mechanism for effectively merging separate topological defects, thus realizing a new tool for OAM manipulations.

## 6.1 Experimental arrangements

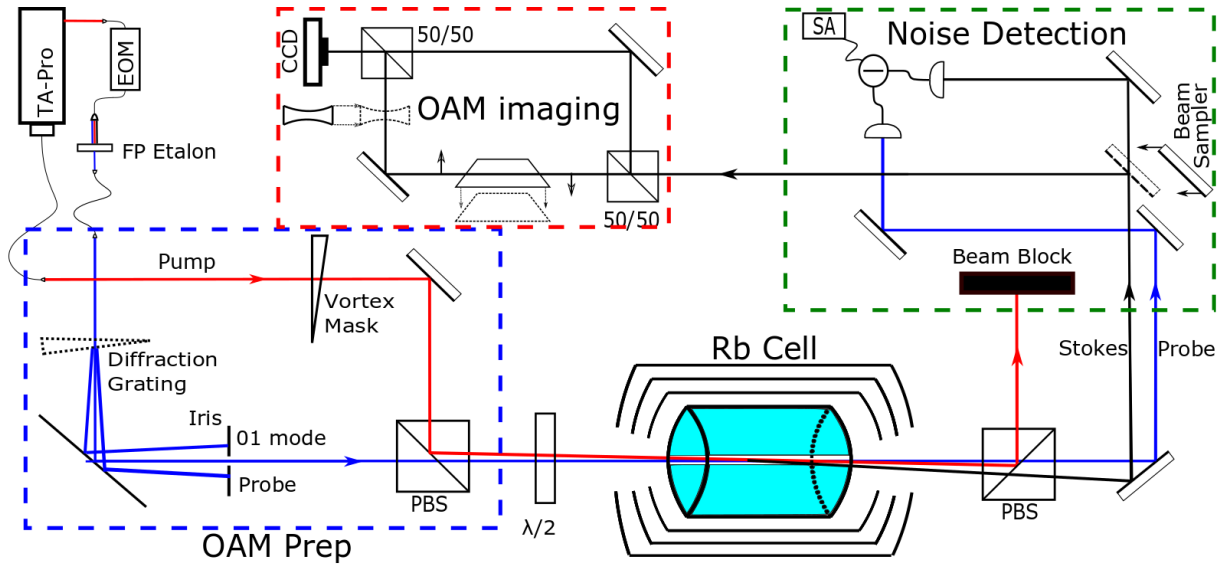


FIG. 6.2: The optical layout of the experimental setup. A single laser is used to generate all outputs. The high-power pump (red) is output through a fiber dock system while the lower power pump output is in free space and later used to generate the probe (blue). The Stokes (black) optical field is generated through FWM in the cell. The set-up has four main sections; probe prep, OAM prep, interaction, noise detection, and imaging. Abbreviations and explanations are given in the text.

The schematic of the experimental setup is shown in Fig. 6.2. We follow the same beam preparation described in Ch. 5. However, we implant spatial modes to our pump and probe before the FWM interaction in the cell. We use two different methods to control the topological charges of the two input optical fields. For the probe field, we used a forked diffraction grating that directed  $\approx 50\%$  of the input intensity into the first diffraction maximum, thus preparing the probe field with the spatial charge of  $\ell = 1$ . For the pump field, we used a transparent spiral vortex phase mask to add  $\ell = \pm 1$  OAM

charge, depending on the mask orientation without significant optical power losses.

The OAM-carrying pump and probe optical fields were then combined at a proper phase-matching angle ( $\approx 0.4^\circ$ ) using a polarizing beam splitter (PBS). At the location of the cell, the pump and probe beams had diameters of  $250 \mu\text{m}$  and  $300 \mu\text{m}$  and powers of  $410 \text{ mW}$  and  $60 \mu\text{W}$ , respectively. After the cell, the pump beam was filtered out using a second PBS, and the amplified probe and generated Stokes fields were spatially separated using an edge mirror and sent to the two inputs of a balanced photodetector for differential intensity measurements.

To analyze the vortex structure of the output beams, we deployed two interference methods. In the first one, either the probe or Stokes beam was individually passed through a Mach-Zehnder interferometer with a divergent lens placed in one of its arms, such that at the output, the original vortex beam overlapped with a constant phase section of the expanded beam. Their interference pattern produced a traditional forked interferogram. This method allowed us to easily identify the position(s) and number of vortices in the original beam by simply counting the number of forked fringes in the resulting interferogram, best seen on the probe beam in Fig. 6.1 (c). For a more accurate analysis of the OAM beam composition, we alternatively replaced the lens with a Dove prism in one of the arms that transposed the beam. The interference of the original and the transposed optical fields resulted in a petal interferogram, in which the azimuthal phase difference between the beams in two interferometer arms produced a flower-like structure with the number of petals equal to the double of the input beam topological charge [177], shown in Fig. 6.6.

## 6.2 Optical angular momentum conversion with single vortex beams

In the first series of measurements, we independently prepared both the pump and probe optical fields in pure LG modes with unit topological charge, as described above. During all of the measurements, the probe was kept in the same ( $\ell_{\text{probe}} = +1$ ) LG mode. However, by flipping the orientation of the phase mask, we set the topological charge of the pump field to be either  $\ell_{\text{pump}} = \pm 1$ . Two configurations were tested: when the pump and probe optical fields had the same ( $\ell_{\text{probe}} = \ell_{\text{pump}} = 1$ ) or opposite ( $\ell_{\text{probe}} = -\ell_{\text{pump}} = 1$ ) OAM charges. For each configuration, our goal was to test the OAM phase matching in Eq. (6.1) by analyzing the intensity and phase profile of all optical fields after the cell. At the same time, we measured the intensity correlations between the output probe and stokes fields to confirm that the intensity squeezing is preserved, even if the two fields are in different transverse modes.

In the first configuration, the identical topological charges in the probe and pump fields  $\ell_{\text{probe}} = \ell_{\text{pump}} = 1$  resulted in the Stokes beam being generated in the same mode,  $\ell_{\text{Stokes}} = 1$ , in Fig. 6.3(a) (right). The identical unit charge for both amplified probe and the generated stokes field was confirmed by the interferogram: when interfered with the plane wave, one clear fork in the interference fringes was observed for both beams. When the phase mask in the pump field was reversed, the pump beam was implanted with a negatively charged vortex and the Stokes was generated in the  $\ell_{\text{Stokes}} = -3$  mode, shown in Fig. 6.3(b)(right). This observation was in excellent agreement with the OAM phase-matching condition.

To achieve the maximum intensity squeezing, great care had to be taken to adjust the waists and the convergence of the pump and probe fields to increase their spatial overlap

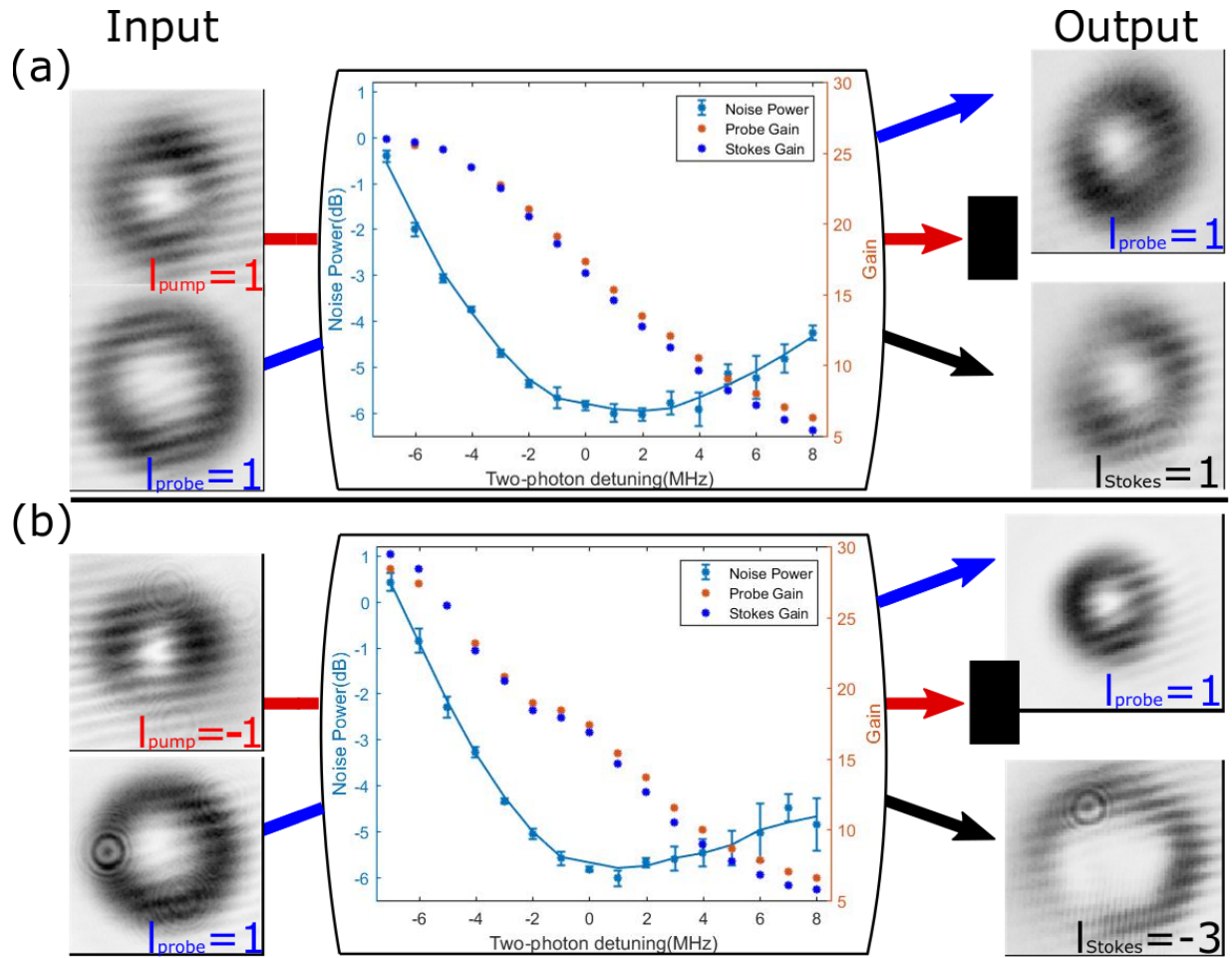


FIG. 6.3: *Left:* Intensity squeezing (left axis) and the FWM amplification for the probe and Stokes fields (right axis) as functions of the two-photon detuning, measured for (a)  $l_{\text{probe}} = +1$ ,  $l_{\text{pump}} = +1$ , and (b)  $l_{\text{probe}} = +1$ ,  $l_{\text{pump}} = -1$  configurations. Images on the left show the flat-front interferograms of the input pump and probe fields at the cell's position, and on the right — the interferograms of the output probe and Stokes fields for each configuration.

inside the Rb cell. The input pump and probe beams are shown on the left of Fig. 6.3(a) and 6.3(b). In these configurations, we saw substantial FWM gain and were also able to maintain a large two-mode intensity squeezing ( $-5.8 \pm 0.1$  dB) whether the pump and probe beams carried the same or opposite charge [see Figs. 6.3(a) and 6.3(b)]. This value was within the standard error of our measurements when comparing to squeezed beams without OAM.

The dependence of the measured gain and two-mode intensity squeezing, on the two-photon detuning (between the probe and pump fields), is shown in Figs. 6.3(a) and 6.3(b). It is similar to the previously reported measurements with conical beams [98]. We defined gain, for both probe and Stokes fields, as the ratio of the output intensity to the intensity of the input probe field. One can see that the FWM gain peak is shifted from the exact hyperfine splitting frequency, due to the power broadening. At the same time, the best quantum-noise suppression occurs not at the maximum gain frequency, but on its wing closer to the two-photon resonance.

The two-photon detuning also affects the transverse profile of the output fields, likely due to the effect of the nonlinear dispersion on the angular phase-matching conditions. Under the conditions for best squeezing, the intensity profiles of both the Stokes and probe fields most closely resembles those expected from a pure LG mode. However, closer to the region of maximum gain, the intensity distributions become uneven: typically, the portion of the output beam that is closer to the pump beam is more amplified. For the positive values of the two-photon detuning, the outer parts of the probe and Stokes fields become more intense.

### 6.3 Optical angular momentum conversion for a composite vortex pump field

In the next series of experiments, we inserted a different phase mask, containing two spiral features separated by  $100 \mu\text{m}$  [178] to produce a pump beam with two spatially separated vortices of charge  $\ell = 1$ , as shown in Fig. 6.4(a). To model a composite vortex structure theoretically, we assumed that the center of a spiral feature was located at  $(r_0, \phi_0)$  with respect to the beam axis. Then we could express the  $\phi$  coordinate of the phase mask as  $\phi' = \arctan(y'/x')$ , where  $x' = r \cos \phi - r_0 \cos \phi_0$  and  $y' = r \sin \phi - r_0 \sin \phi_0$ . With this in mind, we modeled the modified pump beam as

$$u_{\text{pump}}(\mathbf{r}) = \sum c_{l,p} u_{l,p}(\mathbf{r}), \quad (6.2)$$

where

$$c_{l,p} = \int r dr d\phi u_{0,0}(r, \phi, z_{\text{mask}}) e^{i\phi'_1} e^{i\phi'_2}, \quad (6.3)$$

and the  $\phi'_i$  coordinates correspond to the two spiral features. The intensity and phase distributions are shown in Figs. 6.4(b) and 6.4(c), respectively, and the experimentally observed pump intensity distribution matched the theoretical one quite accurately.

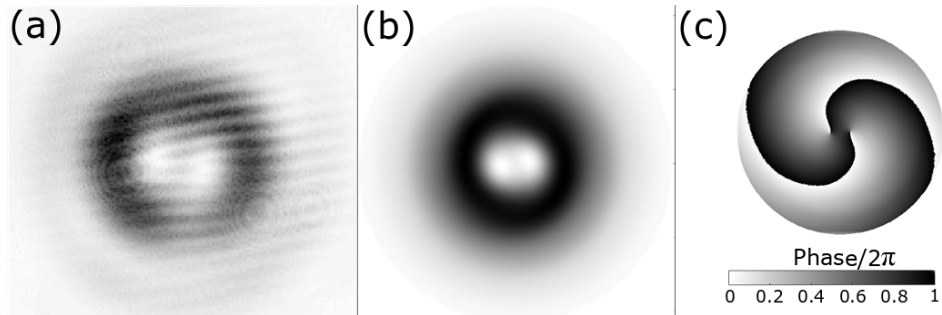


FIG. 6.4: Composite vortex pump beam: (a) experimentally measured interferogram of the pump beam at the location of the Rb cell, (b) simulated pump beam transverse intensity distribution, described by Eq. (6.2), and (c) a phase map of the simulated pump field.



It has been shown that such composite vortex beams can be decomposed into a superposition of pure LG modes, which allow the generation of high-dimensional entangled states [179, 180]. Thus, our goal was to study how the composite nature of the pump beam topological charge and the OAM conservation affect the structure of the generated Stokes field. For example, according to Eq.(6.1), two individual pump vortices with  $\ell_{\text{pump}} = \pm 1$  should result in the generation of a Stokes field with a similar composite vortex structure, containing two vortices of either  $\ell = 1$  or  $\ell = -3$ , depending on the mask orientation. Thus, when the total Stokes topological charge is measured, we would expect it to be either 2 or  $-6$ . However, this is not what we observed experimentally. For one orientation of the phase mask, the Stokes optical field was produced in the  $\ell = 3$  mode, seen in Fig. 6.5(a1). In the second configuration, we observed the Stokes field generated in the  $\ell = -5$  mode, seen in Fig. 6.5(a3). Such behavior is consistent with the pump field contributing its total topological charge into the four-wave mixing phase matching conditions, thus behaving as a simple beam carrying  $\ell_{\text{pump}} = \pm 2$  OAM. The corresponding theoretical simulations, shown in Figs. 6.5(b2) and 6.5(b4) confirm this observation.

The modal analysis seen in Ref. [177] allowed us to more precisely quantify the distribution of  $\ell$  values in the generated Stokes fields. Using the spectral interferograms produced in the interferometer with the inserted Dove prism [see Figs. 6.5(b1)–6.5(b4)], we carried out the Fourier analysis of the azimuthal intensity distribution and confirmed that the observed petal structure consist of mainly either  $\ell = 3$  or  $\ell = -5$  LG mode with over a 90% confidence, both experimentally and numerically [Figs. 6.5(c1)–6.5(c4)]. Small contamination of correspondingly  $\ell = 1$  and  $\ell = 3$ , especially noticeable in the theoretical simulations, can be explained by the asymmetry of the Stokes beam caused by the spatial separation of the multiple vortices.

As in the case of simple vortex beams, we saw that the intensity squeezing between the probe and Stokes was maintained in these cases as well, and followed the same general

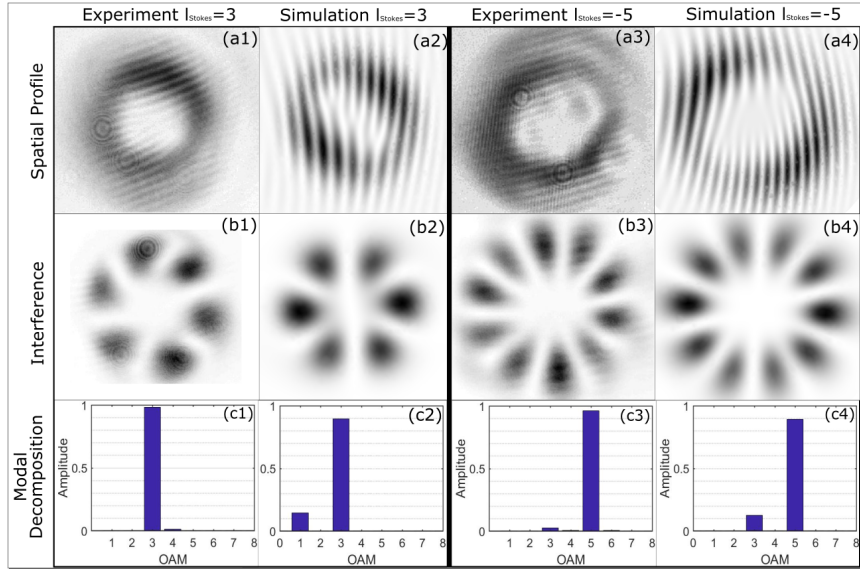


FIG. 6.5: Top row: (a1, a3) experimentally measured and (a2, a4) numerically simulated intensity profiles of the generated Stokes field for the composite pump field, containing two  $\ell = \pm 1$  spatially-separated optical vortices, correspondingly. Middle row: spiral interferograms of each beam. Bottom row: Fourier mode decomposition of the radial intensity distributions of the spectral interferograms for different LG mode indices  $\ell$ .

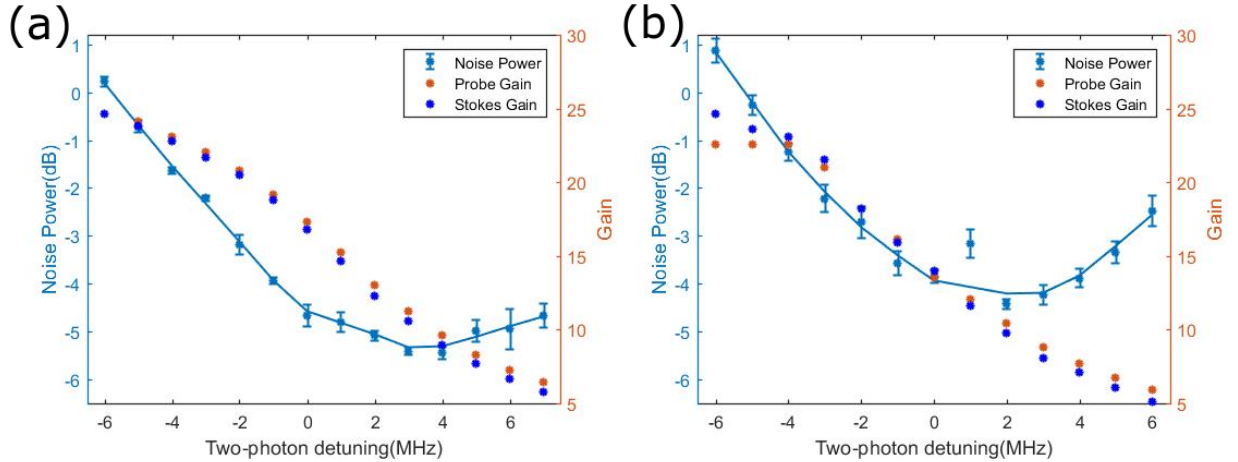


FIG. 6.6: Measured intensity squeezing (left axis) and the FWM amplification for the probe and stokes fields (right axis) as functions of the two-photon detuning, measured for (a)  $\ell_{\text{probe}} = +1$ , composite pump  $\ell_{\text{pump}} = 2 \times 1$ , and (b)  $\ell_{\text{probe}} = +1$ ,  $\ell_{\text{pump}} = 2 \times (-1)$  configurations.

trend. However, due to larger sizes of both Stokes and pump beam, the spatial filtering of the pump field was less efficient, resulting in small leakage of the pump signal into the detection scheme, thus reducing the detected squeezing. Nevertheless, in the case of Stokes generated in  $\ell = 3$ , we measured up to nearly  $-5$  dB of intensity difference squeezing [Fig. 6.6(a)]. For the other mask orientation, in which the Stokes field was generated with the total topological charge of  $\ell_{\text{stokes}} = -5$ , the measured squeezing level was worse, roughly  $-4.3$  dB, mostly due to even larger Stokes beam size [see Fig. 6.6(b)]. However, we believe that with the optimized detection geometry we should be able to regain the same amount of squeezing even for the beams with large topological charge difference, as in this case.

## 6.4 Conclusion

In this chapter we have demonstrated control of the Stokes-field spatial-mode structure by means of shaping the input pump and probe fields using independent phase elements. We found that the Stokes-field OAM can be controlled in a much wider range without degrading the two-mode intensity squeezing between the amplified probe and generated Stokes field, regardless of their spatial mode mismatch. We also found that closely positioned phase singularities in the pump field can be effectively added in the four-wave mixing process, resulting in topological charge of the Stokes field being dependent on the total OAM of the pump, not the sum of two independent vortices. This opens an interesting avenue for the manipulation of the complex spatially separated LG modes, and generation of OAM-enabled hyperentanglement.

# CHAPTER 7

## Implementation of

## Polarization-Based Truncated SU

## (1,1) Interferometer in Hot Rb Vapor

### 7.1 Introduction

In this chapter, we analyze the performance of a recently proposed modification [16] of a so-called truncated SU(1,1) interferometer [5, 119, 122, 123], that takes advantage of polarization manipulations of the involved optical fields. As a reminder, the conventional SU(1,1) interferometer is akin to the Mach-Zhender interferometer which uses two nonlinear beam splitters rather than linear ones, resulting in the noiseless amplification of the fields and interference after phase accumulation for enhanced phase sensing [26, 181–183], shown in Fig. 7.1 (a). Four-wave mixing in a Rb vapor cell can serve as the nonlinear beam splitter to produce noiseless amplification and then interfere the amplified probe and newly generated conjugate field in a second cell by tuning of the phase matching conditions. How-

ever, the practical difficulties of experimental realization of two identical nonlinear beam splitters greatly reduces the practicality of traditional SU(1,1) interferometers [119].

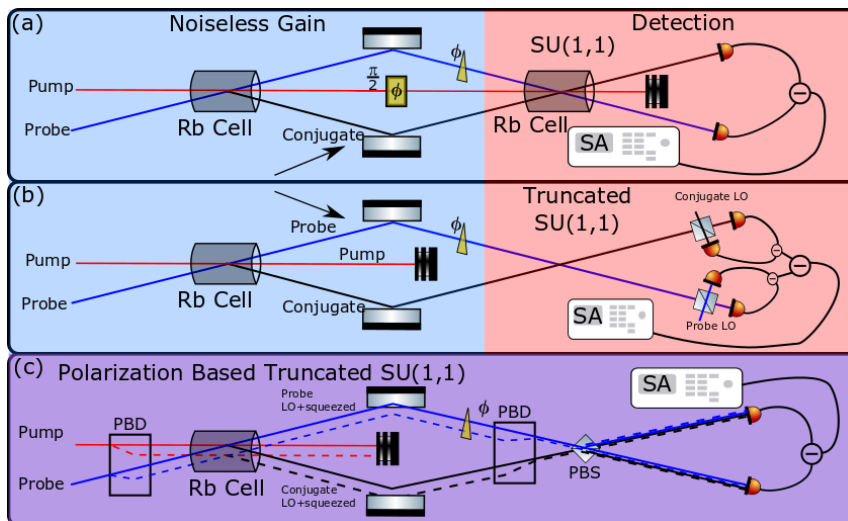


FIG. 7.1: (a) Traditional SU(1,1) interferometer: the first cell acts as a noiseless amplifier (shown in blue) while the second cell and the balanced photodiodes serve as a detector (shown in pink). (b) A truncated SU(1,1) interferometer, in which the second cell is replaced with balanced homodyne detectors with external local oscillators (LOs) (shown in pink). (c) A polarization-based truncated SU(1,1) interferometer. Here the amplifier cell is also used to generate local oscillators and combined with the quantum fields using polarization optics, and then final detection is carried out by a single balanced photodiode.

Fortunately, similar enhancement in sensitivity can be achieved without the use of the second vapor cell, but rather by performing a proper joint quadrature measurements to both output twin beams [119]. In such so-called truncated SU(1,1) interferometer the second beam-splitter is replaced by a pair of homodyne detectors that use a pair of reference fields to act as local oscillators (LO) for the squeezed twin beams [5, 119, 122, 123], shown in Fig. 7.1 (b). In this case the phase stability between all four optical fields becomes critical; if separate lasers are used as LOs, they must be phase-locked to the generated quantum fields. Alternatively, a dual-rail construction can be used to generate both the squeezed twin beams and the LOs simultaneously, using the same laser. The polarization-based truncated SU(1,1) interferometer, discussed here, goes a step further, as we demonstrate that it is possible to retrieve the information in the phase and amplitude joint quadratures

with a single balance homodyne detector, shown in Fig. 7.1 (c). Moreover, by manipulating relative phases between the two quantum beams and their respective LOs, we realize all-optical tuning to any desired joint quadrature. We can also use our results to confirm the quantum inseparability of the two squeezed beams. Furthermore, we should be able in principle to adjust our device so that it will generate two pairs of entangled beams rather than the entangled beams with their LOs [13, 14].

These modifications to the truncated  $SU(1,1)$  interferometer enable some very beneficial properties for practical applications in quantum communications and quantum metrology by increasing the stability and reducing the technical complexity. For example, since only a single balanced photodiode is required, the problem of detectors disbalance is automatically eliminated. The intrinsic symmetry of the system results in a better stability and balancing of powers in the two ports of the detector. This enhanced stability and balance allows for sub-shot noise detection at frequencies ranging from a few MHz to as low as 200 Hz. Lastly, this same setup can be used for the generation of polarization entangled beams [13, 14].

This chapter is structured as follows. In section 2, we discuss the experimental arrangement for the proposed interferometer and its key features and technical challenges. In section 3, we provide the analytic description of the system, derive expressions for the expected noise measurements and discuss the cases of importance. In section 4, we present experimental data showing squeezing of joint quadratures in wide range of detection frequencies, as well as, confirming that the system indeed produces entangled beams. Finally, we conclude with section 5.

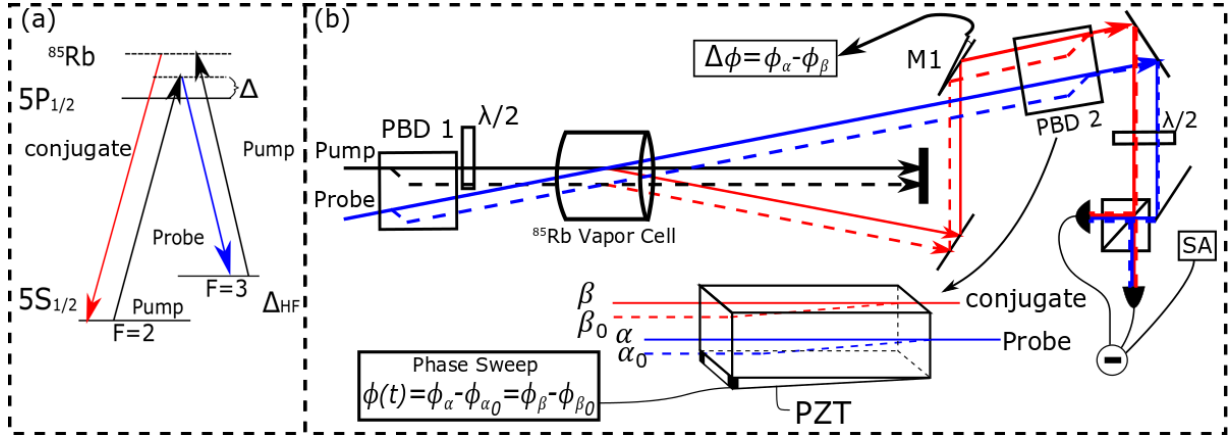


FIG. 7.2: (a) The level diagram of  $^{85}\text{Rb}$  and the corresponding FWM process where the probe (blue), pump (red), and conjugate (black) form a four-photon resonance and couple the two hyperfine ground states through a virtual level detuned  $\approx +1$  GHz from the  $5P_{1/2}$  excited state. The pump frequency was fixed at 794.9727 nm. (b) The schematics of the experimental apparatus for the polarization based truncated SU(1,1) interferometer (see text for abbreviations). Images are taken from Ref.16.

## 7.2 Experimental Arrangements

The experimental apparatus for the polarization based truncated SU(1,1) interferometer is shown in Fig. 7.2 (b). The beam preparation for the probe and pump optical fields follows same as seen in Ch. 5. However, rather than simple interaction in the cell of the two beams, we generate a dual rail system. This is done to LOs and squeezed fields in identical spatial and spectral modes, both input probe and pump beams are split using a polarizing beam displacer (PBD1) which vertically displaces the horizontally-polarized components by 4 mm (in the vertical direction) with respect to the vertically-polarized ones. The polarization of the pump beam is rotated by  $45^\circ$  before the PBD so that it is split evenly between the lower (dashed) and upper (solid) rail, approximately 160 mW each. This is necessary so that the nonlinearity is the same for the two rails for better mode structure matching [184]. The probe is split unevenly where the lower, squeezed rail can either be completely unseeded (i.e., the input probe is in a coherent vacuum state), or is seeded by a very weak ( $< 1 \mu\text{W}$ ) probe beam. In either case, the upper LO rail has a

majority of the power ( $\leq 30 \mu\text{W}$ ). In Sec. 7.4, we will demonstrate that the quantum noise reduction is similar for when the lower squeezed rail is seeded or not, but the presence of the seeded fields allows observation of intensity interference that we can use for sub-shot noise phase measurement [122].

Thus, before the Rb cell, we created four optical beams arranged in a roughly box configuration. The probe and pump channels, shifted down by the PBD1 (the lower rail) are designated for the quantum signals, and the unshifted beams (upper rail) are used to generate strong local oscillators. In each rail the probe and pump fields are mutually orthogonally polarized. The pump field in the lower/upper rail has vertical/horizontal polarization while the probe field in the lower/upper rail has horizontal/vertical polarization, correspondingly. Then, all four beams are directed into a 22-mm long Pirex  $^{85}\text{Rb}$  vapor cell, mounted inside a three layer magnetic shield, such that each pair of pump and probe beams crosses inside the cell. The temperature of the cell is stabilized at  $106^\circ\text{C}$ .

After the interaction with Rb atoms as shown in Fig. 7.2(a), the output consists of three beams – an amplified probe, pump, and generated conjugate beams – for each rail (total of six). The pumps beams in both rails are removed by using an opaque mask. Then the probe and conjugate quantum signals (lower rail) are recombined with their corresponding local oscillators (LOs) from the top rail using a second polarizing beam displacer (PBD2). This is possible since both probe and conjugate beams of the LO rail have orthogonal polarizations with respect to the probe and conjugate beams in the squeezed rail. To make both probe and conjugate beams parallel and to enable the independent control of the relative phase between the probe LO relative and the conjugate LO  $\Delta\phi$ , the conjugate beams are reflected off an additional mirror (M1). The phase of the two LOs relative to the two squeezed fields is controlled synchronously by small tilt of the PBD using a piezo-electric transducer (PZT). After the LOs are combined with their respective squeezed fields, the resulting probe and conjugate beams are mixed by using a half wave



plate set to  $45^\circ$  and a polarizing beam cube, evenly splitting each beam between the two ports of the balanced photodetector (BPhD) for homodyne detection. The differential photocurrent is then analyzed using a spectrum analyzer (SA) across a range of detection frequencies from a few kHz to a few MHz. In majority of the experiment the SA resolution bandwidth was 3 kHz and the video bandwidth was 100 Hz. This detection method allows for measurement of the four joint quadratures of noise, as will be further discussed in Sec. 7.3.

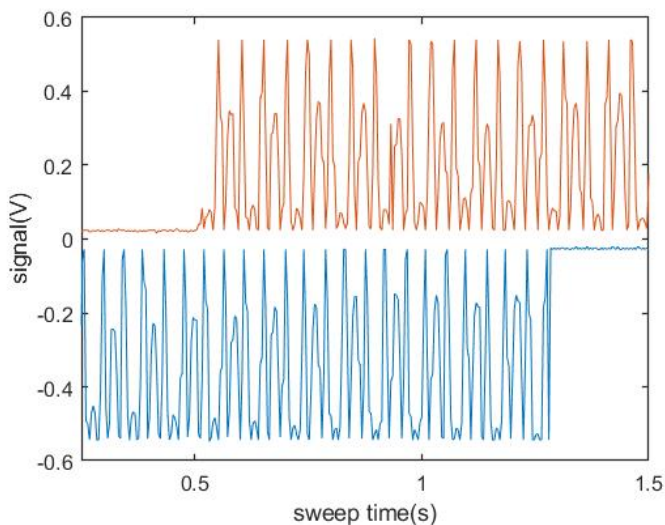


FIG. 7.3: Individual photo-currents of each port of the balanced photodetector as the local oscillator phases are scanned with respect to their squeezed fields to demonstrate the high interference visibility. Flat regions correspond to pump leakage measurements (see text for details).

In order to reliably measure the squeezing between the probe and conjugate fields, there are some technical factors to consider. The sufficient filtering of the two strong pump fields was crucial. Since the two-rail configuration required the two pumps to be orthogonally polarized, the traditional polarization filtering using a single polarizer was not possible. Instead, we used a series of opaque masks and irises to spatially remove as much of pump fields as possible. In order to efficiently use the irises to remove any remnant pump leakage and improve signal stability, we overlapped the four fields going to

the ports of the detectors, shown by overlapped dashed and solid (blue and black) lines in Fig. 7.2(b), after the PBS for the balanced detection. In addition to pump filtering, it was also very important to have proper mode matching between the LOs and the squeezed beams [184]. As a gauge for mode matching and mixing of the fields, the visibility was used as a reference. In order to observe the visibility, the input probe seeds for both rails were balanced at  $15 \mu W$ . Then, we were able to measure a visibility in the interference fringes of over 98%, shown in Fig. 7.3. The interference region of the figure shows the signals in each photodetector channel when the phase of the two fields in the upper rail is dithered with respect to the two fields in the lower rail over a range of  $\approx 2\pi$ . Due to the offset of the phase, we see turning points in the sweep near half-max for both sweeps. The flat region shows the case where both input probe seeds are blocked. In this case, we see an offset in both traces. This offset is due to the pump leakage into the two detector ports, and is also the lower bound on the interference fringes. It can be seen that the pump leakage is small compared to the signal and is the same for both ports, seen by the flat parts of the blue and red traces in Fig. 7.3. Thus, we expect that the excess noise due to the pump field on the spectrum analyzer will also be small.

### 7.3 Analytic Description of the Optical Joint Quadrature Control and Detection

In our calculation, we follow the formalism in Ref.23. There, it is shown that an optical field can be expressed in the semi-classical sense as a mean field amplitude and a respective noise quadratures with an overall phase. In the calculations, we use the following notation: the labels  $\alpha$  and  $\beta$  refer to the parameters of the local oscillators at the probe and conjugate frequencies, correspondingly; similarly, we use  $\alpha_0$  and  $\beta_0$  to describe the

squeezed optical fields.

$$\hat{\alpha} = (|\alpha|' + \delta\hat{X}_\alpha + i\delta\hat{Y}_\alpha)e^{i\phi_\alpha} \quad (7.1)$$

$$\hat{\beta} = (|\beta|' + \delta\hat{X}_\beta + i\delta\hat{Y}_\beta)e^{i\phi_\beta} \quad (7.2)$$

$$\hat{\alpha}_0 = (|\alpha_0|' + \delta\hat{X}_{\alpha_0} + i\delta\hat{Y}_{\alpha_0})e^{i\phi_{\alpha_0}} \quad (7.3)$$

$$\hat{\beta}_0 = (|\beta_0|' + \delta\hat{X}_{\beta_0} + i\delta\hat{Y}_{\beta_0})e^{i\phi_{\beta_0}} \quad (7.4)$$

FWM theory predicts that individual phase and amplitude quadratures for each field are above the shot noise [185]. However, if their joint quadratures are measured, squeezing or anti-squeezing can be observed:

$$\langle(\Delta\hat{X}_-)^2\rangle = \langle\delta^2(\delta\hat{X}_{\alpha_0} - \delta\hat{X}_{\beta_0})\rangle = \frac{1}{4}e^{-2r}; \quad (7.5)$$

$$\langle(\Delta\hat{X}_+)^2\rangle = \langle\delta^2(\delta\hat{X}_{\alpha_0} + \delta\hat{X}_{\beta_0})\rangle = \frac{1}{4}e^{2r}; \quad (7.6)$$

$$\langle(\Delta\hat{Y}_-)^2\rangle = \langle\delta^2(\delta\hat{Y}_{\alpha_0} - \delta\hat{Y}_{\beta_0})\rangle = \frac{1}{4}e^{2r}; \quad (7.7)$$

$$\langle(\Delta\hat{Y}_+)^2\rangle = \langle\delta^2(\delta\hat{Y}_{\alpha_0} + \delta\hat{Y}_{\beta_0})\rangle = \frac{1}{4}e^{-2r}; \quad (7.8)$$

where  $r$  is the squeezing parameter, determined by the FWM gain [23, 185].

To relate the proposed optical method of detection to the joint quadrature measurements, we carry out the matrix operations for the beam splitters while tracking the relevant phases of the two pairs of beams. Immediately after the cell, we begin by combing the probe and conjugate beams with their respective LOs using a polarizing beam displacer PBD2. This element is one of the key elements to control the phase. Since the upper rail (LOs) and the lower rail (squeezed fields) have orthogonal polarizations, the LOs acquire a

different phase shift compared to the squeezed fields. Additionally, this phase for the LOs is more sensitive to the alignment of the beam displacer than that of the squeezed beams since it is aligned to the fast axis. This allows us to set the phases of the squeezed beams constant or even zero ( $\phi_{\alpha_0} = \phi_{\beta_0} = 0$ ). Then we only need to track the phases of the LOs which vary relative to their respective squeezed field and relative to each other. The phase of the LOs with respect to each other are adjust via a mirror (M1), changing the angle of one of the squeezed beams and their LOs, while the phases of the LOs with respect to the squeezed fields are adjusted by adjusting the vertical angle of the PBD which is connected to a piezo-electric modulator, making the phase of the LOs with respect to the squeezed fields a time dependent sweep. With this information, we rewrite Eqs. (7.1-7.4) for the beams as follows:

$$\hat{\alpha} = (|\alpha|' + \delta\hat{X}_\alpha + i\delta\hat{Y}_\alpha)e^{i\phi(t)}, \quad (7.9)$$

$$\hat{\beta} = (|\beta|' + \delta\hat{X}_\beta + i\delta\hat{Y}_\beta)e^{i(\phi(t)-\Delta\phi)}, \quad (7.10)$$

$$\hat{\alpha}_0 = (|\alpha_0|' + \delta\hat{X}_{\alpha_0} + i\delta\hat{Y}_{\alpha_0}), \quad (7.11)$$

$$\hat{\beta}_0 = (|\beta_0|' + \delta\hat{X}_{\beta_0} + i\delta\hat{Y}_{\beta_0}), \quad (7.12)$$

where  $\phi(t)$  is the phase of the LOs with respect to the squeezed fields and  $\Delta\phi$  is the phase of the the LOs with respect to each other.  $\phi(t)$  is controlled by the angle of the PBD (mounted on a PZT) used to overlap the LOs with their respective squeezed fields, while  $\Delta\phi$  is tuned by using M1, shown in Fig. 7.2 (b), which controls the phase of the LOs with respect to each other.

To this point, the fields have not interfered since the two rails have orthogonal polarizations from when they were combined. The key operation is the final mixing of the

fields after the last beam splitter. Here, it is important that each LO and squeezed field are split evenly into the two balanced ports of the balanced photodetector. So, the LOs are combined with their respective squeezed fields, the polarizations of the beams are rotated by 45 degrees in order to evenly mix the beams of orthogonal polarizations on the polarizing beam splitter (PBS) which then interfere and are detected by the two ports of the balanced detector. The current generated at each photodetector port is given by:

$$\hat{i}_1 \propto |\hat{\alpha} + \hat{\alpha}_0 + \hat{\beta} - \hat{\beta}_0|^2 \quad (7.13)$$

$$\hat{i}_2 \propto |\hat{\alpha}_0 - \hat{\alpha} + \hat{\beta} + \hat{\beta}_0|^2 \quad (7.14)$$

Here, we ignore the terms containing the product of  $\alpha$  and  $\beta$  since they will oscillate at a frequency of doubled hyperfine splitting, that is not picked up by our photodetector (with a few MHz detection bandwidth). Since we use a balanced homodyne detector, we take the difference of the two currents and then analyze the noise of the signal in the Fourier domain, for which the noise signature is flat across all detection frequencies, under ideal conditions. By inserting Eqs. (7.9-7.12) into Eqs. 7.13 & 7.14 and taking the differential current ( $i_- = i_1 - i_2$ ), we arrive at:

$$\begin{aligned} \hat{i}_- &= \alpha\alpha_0 \cos(\phi(t)) - \beta\beta_0 \cos(\phi(t) - \Delta\phi) \\ &+ \alpha[\delta\hat{X}_{\alpha_0} \cos(\phi(t)) - \delta\hat{Y}_{\alpha_0} \sin(\phi(t))] \\ &- \beta[\delta\hat{X}_{\beta_0} \cos(\phi(t) - \Delta\phi) - \delta\hat{Y}_{\beta_0} \sin(\phi(t) - \Delta\phi)] \end{aligned} \quad (7.15)$$

Here we made the assumption that the mean amplitudes of the squeezed fields are much smaller than those of the LOs. We also assumed the balanced FWM gain for the probe and conjugate channels, so that the intensity of the two local oscillators are the

same, and the intensities of the two squeezed fields are the same:  $\alpha = \beta \gg \alpha_0 = \beta_0$ . Below, we simplify the expressions for the two cases in which we expect to observe joint quadrature squeezing, according to Eqs.(7.5-7.8) by looking at the specific values of the relative phases of the two LOs.

In case 1, we consider  $\phi_\alpha = \phi_\beta = \phi(t)$  ( $\Delta\phi = 0$ ). This represents the LOs changing in-phase simultaneously relative to the squeezed fields. In this case, Eq. 7.15, for the current reduces to:

$$\hat{i}_- = \alpha[(\delta\hat{X}_-) \cos(\phi(t)) - (\delta\hat{Y}_-) \sin(\phi(t))], \quad (7.16)$$

where

$$X_\pm = \hat{X}_{\alpha_0} \pm \hat{X}_{\beta_0} \quad (7.17)$$

$$Y_\pm = \hat{Y}_{\alpha_0} \pm \hat{Y}_{\beta_0}. \quad (7.18)$$

This shows that no matter how we tune the phase of the LOs, we will not see any fluctuations in the mean intensities. In this case, the intensities of the beams always interfere and change at a rate where both detectors always see the same total intensity of light. We can then find the variance of this differential current in Eq. 7.16,  $\langle \Delta\hat{i}_- \rangle = \langle (\hat{i}_-)^2 \rangle - \langle \hat{i}_- \rangle^2$ :

$$\langle (\Delta\hat{i}_-)^2 \rangle = |\alpha|^2 [\langle \Delta(\hat{X}_-)^2 \rangle \cos^2(\phi(t)) + \langle \Delta(\hat{Y}_-)^2 \rangle \sin^2(\phi(t))] \quad (7.19)$$

Here, we can see that the first term is the variance of the amplitude difference joint quadrature and the second term is the variance of the phase difference joint quadrature.

The prior is squeezed and the latter is anti-squeezed. So as the phase of the LOs  $\phi(t)$  changes, we move between the two joint-quadratures. This is shown in Fig. 7.4(a). The dashed curve represents the differential intensity, that remains constant around 0, measured by the balanced photodetector while the solid curve is the noise power of the differential current measured by the spectrum analyzer, as expected from the analytic calculations. The sweep is done over  $2\pi$  rads to cover the full range of the sweep.

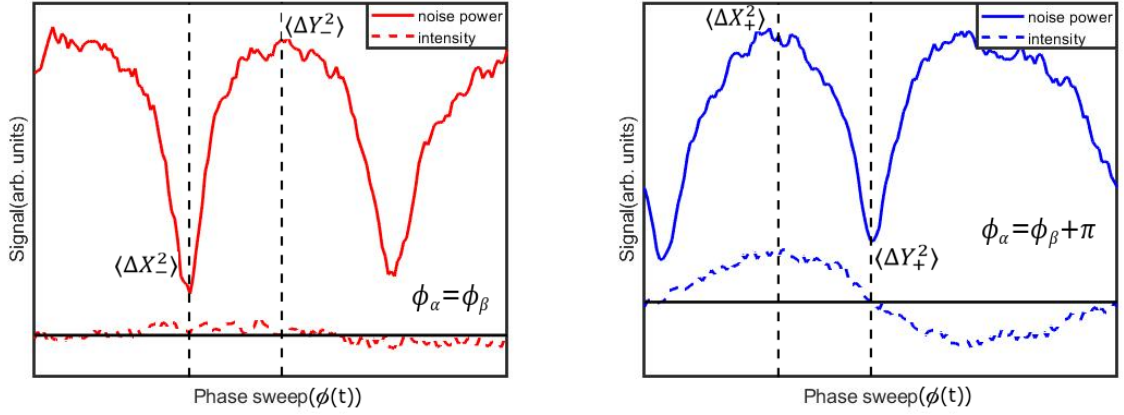


FIG. 7.4: (a) The differential current (red, dashed) and noise power (red, solid) as a function of the phase  $\phi(t)$  swept from 0 to  $2\pi$  for the case  $\phi_\alpha = \phi_\beta$  ( $\Delta\phi = 0$ ). (b) The differential current (blue, dashed) and noise power (blue, solid) as a function of the phase  $\phi(t)$  swept from 0 to  $2\pi$  for the case  $\phi_\alpha = \phi_\beta$  ( $\Delta\phi = \pi$ ).

In case 2, we set the two LOs to be  $\pi$  out of phase with each other  $\phi_\alpha = \phi_\beta + \pi = \phi(t)$  ( $\Delta\phi = \pi$ ), even though they are changing in phase simultaneously relative to their corresponding squeezed fields. In this case, Eq. 7.15 reduces to:

$$\hat{i}_- = 2\alpha\alpha_0 \cos(\phi(t)) + \alpha[(\delta\hat{X}_+) \cos(\phi(t)) - (\delta\hat{Y}_+) \sin(\phi(t))] \quad (7.20)$$

Contrary to case 1, here we see that the terms for the fluctuations in the intensity survive. This likens back to the typical workings of an interferometer. In this case, both beams are interfering in a way that results in the total intensity in the system fluctuating

from one port of the balanced detector to the other. This interferometric operation is also fitting for this case, since it results in the measurement of the squeeze joint-phase quadrature. This will be seen by taking the variance of the differential current in Eq 7.20.

$$\langle(\Delta\hat{i}_-)^2\rangle = |\alpha|^2[\langle\Delta(\hat{X}_+)^2\rangle \cos^2(\phi(t)) + \langle\Delta(\hat{Y}_+)^2\rangle \sin^2(\phi(t))] \quad (7.21)$$

Here, we are now measuring the joint quadratures for the amplitude (first term) and phase sum (second term). For FWM, the amplitude sum is anti-squeezed while the phase sum is squeezed. So as the phase of the LOs relative to the squeezed fields is changed, we sweep through the different joint noise quadratures. A specific point of interest here is the point of maximum squeezing. Unlike case 1, where the intensity was constant regardless of phase, in case 2 it is changing. Here, it happens that the phase ( $\phi(t)$ ) corresponding to maximum squeezing, also corresponds to the point of greatest interferometric sensitivity. The point where the intensity is changing the fastest with the phase. There is an added appeal to this method since there is reduced noise measurement at the point of greatest sensitivity. This is shown in Fig. 7.4 (b) by the blue curves. The dashed curve represents the differential current ( $i_-$ ) while the solid line represents the noise power of the differential current as a function of the phase over a range of  $2\pi$  radians. It can be seen that the point of lowest noise power coincides with the point of maximum interferometric sensitivity, shown by vertical dashed line labeled by  $\langle\Delta\hat{Y}_+^2\rangle$ .



## 7.4 Measurement of Squeezed Joint Quadratures and Entanglement

In the previous section, we introduced the form our noise and intensity signals would take as we moved from one joint quadrature to another. However, the accurate detection of squeezing using such large sweep is nearly impossible when using a reasonable combination of low video bandwidth and not too low sweep time, since there would be smoothing of the signal at the sharp feature where squeezing is present. In order to accurately measure this, we substantially reduced the range of the sweep from  $2\pi$  to  $\pi/4$  around the minima of the joint quadrature noises. Under these conditions, we are able to more accurately determine the squeezing values.

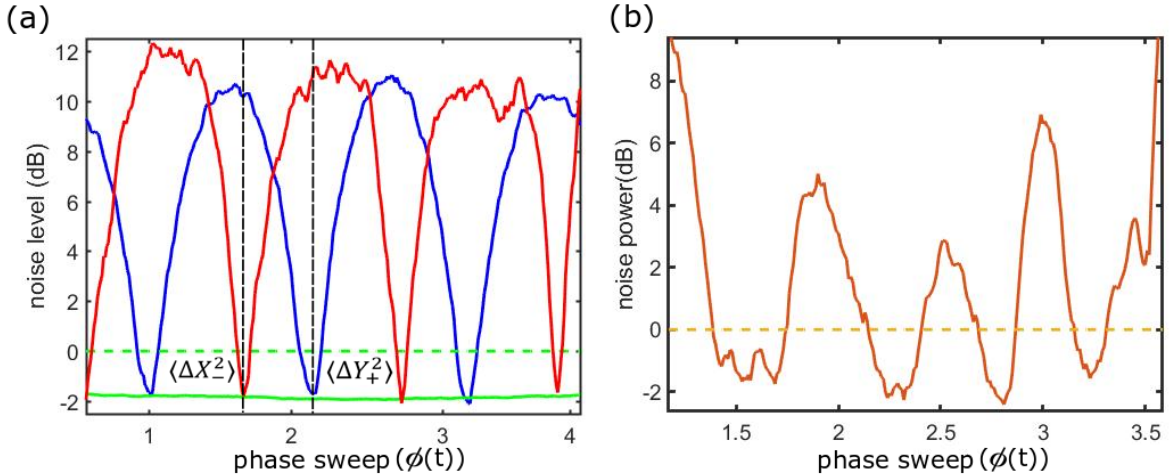


FIG. 7.5: (a) Measured joint quadrature noise power for the cases 1 ( $\Delta\phi = 0$ ) and the case 2 (blue,  $\Delta\phi = \pi$ ) as the phase  $\phi(t)$  of the LOs is swept with respect to the squeezed fields, for the case of seeded squeezed field. Solid green line shows the minimum detected quadrature noise,  $\approx -2dB$  below the shot noise (dashed green line). (b) Analogous measurements performed with the vacuum-seeded input field, showing the joint quadrature noise power as a function of the phase  $\phi(t)$ .

Similar to the solid traces in Figs. 7.4 (a) and (b), Fig. 7.5 (a) shows the noise power as the phase between the LOs and the squeezed fields are swept. Color codes to the previous section, red corresponds to case 1 ( $\phi_\alpha = \phi_\beta, \Delta\phi = 0$ ) and blue corresponds to

case 2 ( $\phi_\alpha = \phi_\beta + \pi = \phi(t)$ ,  $\Delta\phi = \pi$ ), shown in Sec.7.3. The blue curve shows the phase sweep of the LOs relative to the squeezed fields near the squeezed phase sum joint quadrature ( $\langle\langle\Delta\hat{Y}_+^2\rangle\rangle$ ), represented by case 1 (LOs in phase), while the red curve shows the sweep near the squeezed amplitude difference joint quadrature, represented by case 2 (LOs  $\pi$  out of phase). In these two sweeps, we see that the noise power drops below the shot noise level expected of the joint measurements of two uncorrelated laser beams, as shown in Fig. 7.5(a) by dashed line. The level of squeezing for each joint quadrature was roughly -2 dB. The solid green line shows the interferometer, case 2 (LOs out of phase by  $\pi$ ), locked to the point of optimal phase sensitivity and lowest noise.

So far, we have demonstrated operation where a seed field is present for the squeezed rail. We can also show that similar noise reduction is seen with the removal of this seed field (i.e., “seeding” the both probe and conjugate inputs of the first nonlinear beam-splitter with coherent vacuum). This arrangement results in the generation of squeezed vacuum twin beams in the lower rail, which are truly entangled beams since there is no coherent seed to add uncorrelated photons. In this configuration, the resulting noise spectrum as a function of phase (of LOs with respect to the two-mode squeezed vacuum  $\phi(t)$ ) would look the same as what is seen in the Eqs. 7.19 & 7.21, as witnessed in the experimental data shown in Fig. 7.5(b). Here, we see that the squeezing is at the same level independent of the seed input probe field present or not for the squeezed rail. While the noise would look the same, we would lose our operation as an interferometer, now the term for the interference of the squeezed beams and the LOs would vanish. This would result in the intensity profile remaining flat with the phase for both case 1 and case 2. However, we could remove the seed probe for the LOs and the squeezed beams and this would result in the output of the two ports of the beam splitter containing polarization-entangled twin beams. Unfortunately, we did not have the technical means to verify this capability experimentally.

In the implementation of this device, we have shown its function as an interferometer and shown that we can measure squeezing and anti-squeezing for the corresponding joint quadratures in Eqs. (7.5-7.8). By using these joint-noise measurements, we can now characterize the degree of entanglement between the two beams. Since the noise measurements are those of shared fluctuations in phase and intensity of the squeezed beams, the measurement of the variance can be related to the correlations and, correspondingly, the inseparability [7, 186]:

$$I = \langle \Delta \hat{X}_-^2 \rangle + \langle \Delta \hat{Y}_+^2 \rangle \leq 2 \quad (7.22)$$

If we show that  $I < 2$ , we can say we have entangled beams [7, 186]. The measured squeezing values for the two joint quadratures  $\langle \Delta \hat{X}_-^2 \rangle = \langle \Delta \hat{Y}_+^2 \rangle = 0.66 \pm 0.03$  yield the inseparability value of  $I = 1.32 \pm 0.04$ . This shows that our beams are correlated beyond the classical limit and can be said to be entangled. There is also a more rigorous way to quantify entanglement; it is given by the Einstein-Poldolski-Rosen (EPR) criteria, requiring that  $4\langle \Delta \hat{X}_-^2 \rangle \langle \Delta \hat{Y}_+^2 \rangle \leq 1$  for entangled optical fields. The minimum value for this parameter that we were able to achieve was 1.75, failing to confirm the EPR entanglement. However, we believe that our experiment was capable of achieving higher levels of squeezing, since the relatively low value of squeezing in the interferometer (-2 dB) was due to the optical losses at the uncoated surfaces of PBD, imperfect mixing, and phase alignment due to mechanical instabilities. In the case of a single channel, not susceptible to these issues, we were able to measure -4.5 dBs of squeezing, shown in Fig. 7.6 (a). If we were able to carry this level of squeezing through the interferometer, the entanglement parameter would have been well below 1, and we would satisfy the EPR criteria as well.

In addition to possibly being a source of polarization entangled beams, the polarization based truncated SU(1,1) interferometer is also useful for enhancing the squeezing

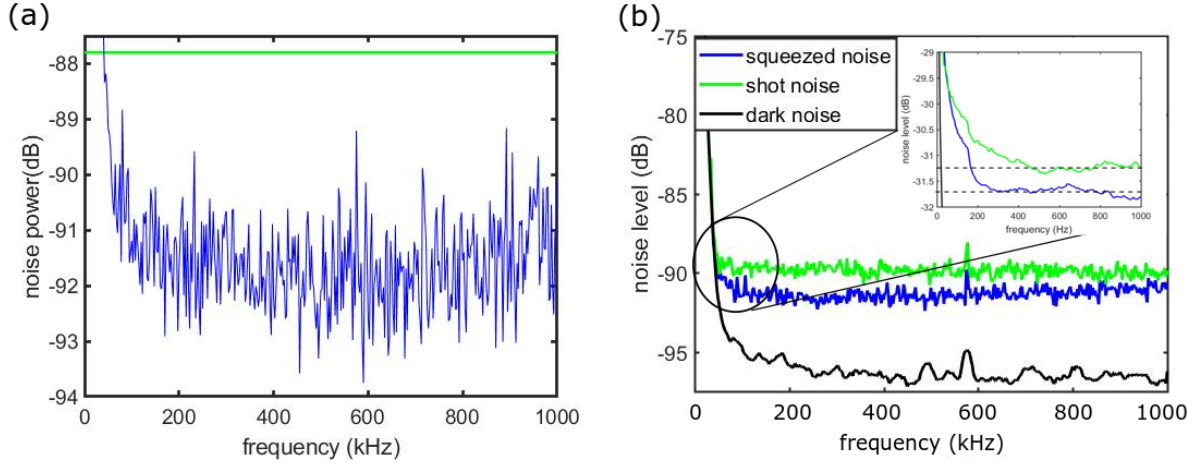


FIG. 7.6: (a) The noise spectrum for intensity squeezing (blue) obtained within a single rail as a function of the detection frequency. Green line represent the shot noise level. (b) Analogous measurements for the noise spectrum of the dual rail interferometer output. The inset zooms on the lower detection frequencies, and was measured using a different spectrum analyzer with less low frequency noise.

detection bandwidth, shown in Fig.7.6 (b). The upper limit, from electronic limitations, is at detection frequencies of a few MHz while on the lower limit, we were able to squeezing at detection frequencies as low as 200 Hz. The operation in this detection regime would be ideal for quantum imaging. Ref. 187 demonstrated the possibility of observation of the spatial correlations between two-mode squeezed bright beams. In this, it required the use of various manipulation on the part of the camera and exposure times, pushing what current camera technologies can handle even with the use of electronic shutters. However, low frequency squeezing allows the use of longer exposure times and more time between frames making quantum imaging electronically easier.

## 7.5 Conclusion

In this chapter, we have demonstrated feasibility and operation of the polarization based truncated  $SU(1,1)$  interferometer. What distinguishes our design from the previous work is its all optical control and tunability, and the simplicity of hardware adjustment

for desired noise regime. For example, with simple phase adjustment it can be tuned to either operate as an interferometer with enhanced sensitivity or as a sensitive differential absorption detector with reduced noise. With this prototype, we were able to achieve nearly  $-2$  dB of noise reduction in both squeezing joint quadratures (limited mainly by uncontrolled phase drift and pump field leakage). Such level of squeezing is sufficient for resulting optical beams to be considered entangled by satisfying the quantum inseparability condition. The level of squeezing can further be improved by using better optics and closed conditions to avoid phase instabilities, likely resulting in even higher entanglement level. The interferometer also had an intrinsic symmetry for detection which allowed for squeezing measurements at detection frequencies from a few MHz to as low as 200 Hz, a trait which has potential applications in quantum imaging and quantum metrology. It also has the added benefit of being a source for polarization entangled Bell states by replacing the probe seeds in both rails with coherent vacuum [13, 14].

# CHAPTER 8

## Enhancement of Raman Two-Photon Spectroscopy using Squeezed Light

### 8.1 Introduction

In this chapter, we discuss the spectral limitations of squeezed light and how they can be overcome. As was discussed in Sec. 2.4, squeezed light can offer a means of noise reduction through more subtle and power efficient means. The ability to make spectroscopic measurements with the aid of squeezed light allows for interesting applications like trace gas detection, bio-sensing, and molecular characterization [120, 126, 128, 129]. However, the frequency of squeezed light is tied to atomic transitions and can only be generated in a narrow range. This limit removes an important extension of using squeezed light for spectral enhancements.

Here, we present a proof of principle concept to couple squeezed light, generated near atomic resonances, to a largely tunable Raman pump laser in a two-photon resonance to enhance the spectral range of application of the FWM process. This has a two fold benefit,

we overcome the spectral limitations of squeezed light generated by FWM and reduce the noise floor for this class of spectroscopic measurements. In this method, the source of squeezed light is not limited to FWM.

This concept can be used to probe both highly excited states [188] or low energy vibrational modes [189]. In a ladder configuration (Fig. 8.1 (b)), one of the correlated twin-beams (probe-blue) is coupled in a two-photon resonance with the Raman pump (green) to a highly excited state. This can be used to investigate the energy structure of an excited state. It may be possible to use this method for sensing applications in Rydberg atoms [11, 12] or multi-photon spectroscopy tools. In the  $\Lambda$  configuration (Fig. 8.1 (c)), the two-photon resonance occurs when the energy difference between the probe and Raman pump beam matches energy differences for low energy states. Such a configuration would be useful for studies of vibrational modes of molecules or crystals [135].

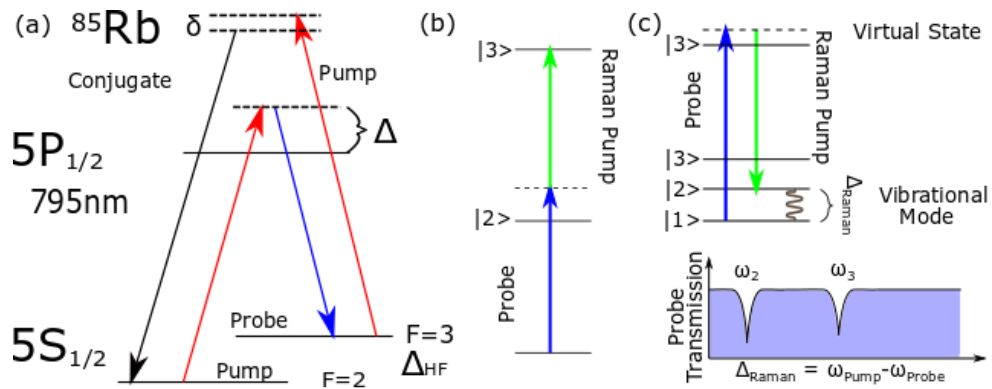


FIG. 8.1: (a) shows the level diagram of the  $^{85}\text{Rb}$  D1 line and the corresponding FWM process where the probe (blue), conjugate (black), and pump (red) optical fields are shown.  $\Delta$  (1GHz) is the two-photon detuning of the probe and pump and  $\Delta_{HF}$  (3036 MHz) is the hyper-fine splitting of the  $5S_{1/2}$  ground state. (b) shows one of the ladder level configurations of this method to probe highly excited states using the Raman pump beam (green). (c) shows the lambda configuration of this method which can be used to probe low energy states and vibrational states of molecules and crystals.

The general limitations for such quantum enhancement arise from the available tuning range of the Raman pump laser. In our case, the Ti:sapph laser is tunable from 700 nm to 800 nm. When coupled in a ladder configuration, this limits the probing of highly excited

states to energies above the ground level corresponding to 3.3 eV-4.1 eV light. While in the  $\Lambda$  configuration, we can potentially probe low energy absorption anywhere from  $5.2 \mu m$  (0.24 eV) to the far IR, and even microwave ( $10^{-3} m$ ). The range is shown by shaded regions in Fig. 8.2 for the two configurations. However, by using Raman pump lasers with different ranges, it would be possible to reach other regions and probe an even broader spectrum with squeezed light for different applications.

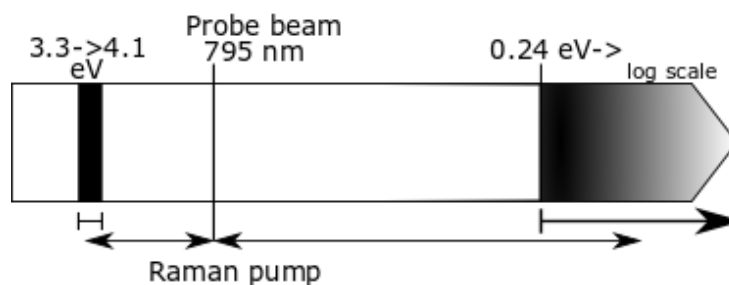


FIG. 8.2: Shaded region shows the possible range of energies probable by the two-photon absorption of the probe field, limited by the range of our Ti:Sapph laser.

Here, we present a proof-of-principle demonstration of this concept by taking measurements of the hyper-fine structure of  $^{87}Rb$ . We coupling the probe optical field to the Raman pump in a two-photon resonance with the  $5D_{3/2}$  state, as shown in Fig. 8.3 (b). In Ch. 3, we utilized the Raman two-photon process to absorb unwanted probe and conjugate photons generated by resonant and off-resonant FWM in Rb vapor. We were able to achieve absorption of the conjugate optical field by coupling it to a Raman pump optical field in a two-photon resonance with the  $5S_{1/2} \rightarrow 5D_{3/2}$  transition. Even though the 5D state is not perceivable to 795 nm light, we were able to probe its level structure. However, the previous study did not utilize squeezed light and had a different directive. Here, we investigate this two-photon transition with the use of squeezed light generated in hot  $^{87}Rb$  vapor.



## 8.2 Raman Resonance Response of $5D_{3/2}$ State

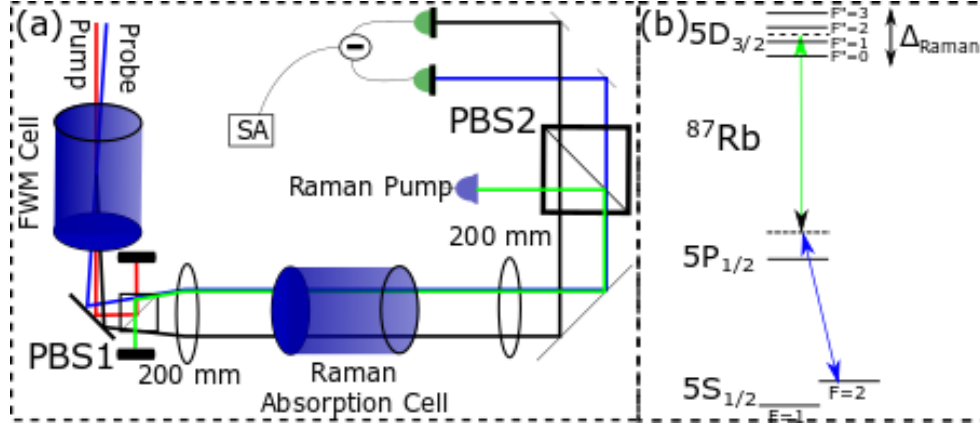


FIG. 8.3: (a) shows the experimental schematic of the experiment, see text for details. (b) shows the two-photon transition ( $5S_{1/2}, F = 2 \rightarrow 5D_{3/2}$ ) of the probe field coupled to the Raman pump field. (c) shows the noise signal produced from absorbing the probe field as the detuning of the Raman pump ( $\Delta_{\text{Raman}}$ ) is swept by 200 MHz. The hyper-fine splitting of the  $5D_{3/2}$  state are labeled accordingly.

The schematic of the setup is shown in Fig. 8.3 (a). Experimental conditions for the squeezed twin-beam generation are the same as those seen in Ch. 5. After generating the correlated twin-beams in the first cell (labeled FWM cell) of  $^{85}\text{Rb}$  atoms, the correlated twin beams are then focused at the center of the second cell of  $^{87}\text{Rb}$  atoms (labeled Raman absorption cell) using a 200 mm lens. The two cells are housed in separate, but identical shields where we fix the temperature of the FWM cell and vary the temperature for the Raman absorption cell for measurements. The second cell, containing  $^{87}\text{Rb}$ , is used as the sample where we probe the  $5D_{3/2}$  excited state using the Raman two-photon absorption of the Raman pump and probe beams, level diagram shown in Fig. 8.3 (b). The Raman pump beam (762.1068 nm) is generated by a Ti:sapphire laser and input into the system via fiber optics and counter-propagating with respect to the probe and combined at a shallow angle over the probe beam using PBS2 to avoid reflections into the detectors. The conjugate field propagates through the cell with no absorption. After the probe absorption in the Raman absorption cell, the twin-beams are detected on balanced detectors and the

AC portion of the signal is picked up by a spectrum analyzer (SA).

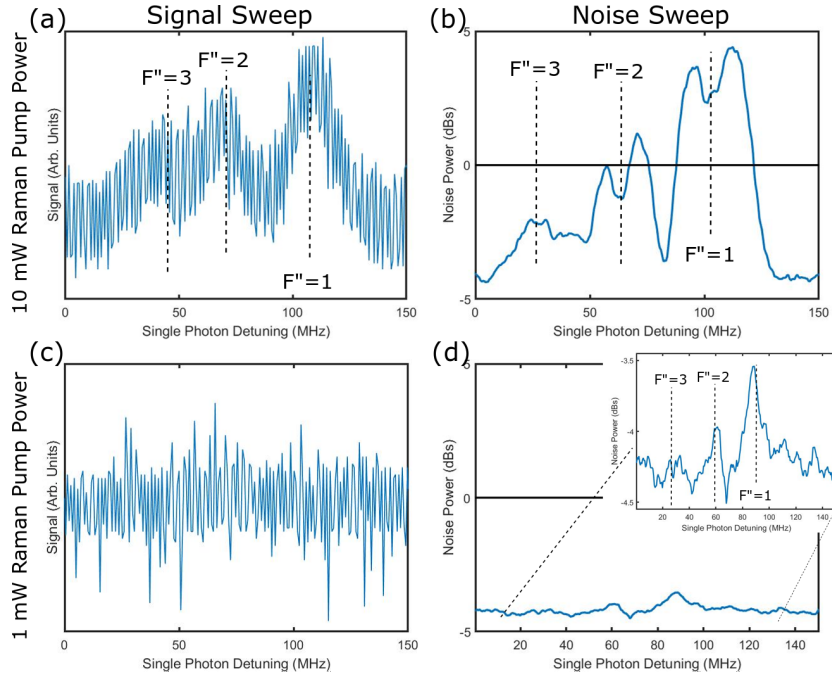


FIG. 8.4: (a) and (c) show the differential intensity of the photodetectors as the pump frequency is tuned through the two-photon resonance with the  $5D$  state for pump powers of 10 mW and 1 mW, respectively. (b) and (d) show the differential noise of the photodetectors picked up by the spectrum analyzer as the pump frequency is tuned through the two-photon resonance with the  $5D$  state for pump powers of 10 mW and 1 mW, respectively. The SA sweep time here is 8 seconds, the resolution bandwidth is 10kHz and the video bandwidth is 10 Hz

Data is taken by sweeping the Raman pump frequency by 200 MHz across the  $5D_{3/2}$  state. The hyperfine splitting between the  $5D_{3/2}$ ,  $F''' = 1$ , and  $F''' = 3$  states is 72 MHz [144]. Each data set maps the resonance structure of the two-photon transition. The sweep in Figs. 8.4 (a) and (c) shows the differential intensity of the probe and conjugate beams as the Raman pump frequency is scanned across the  $5D_{3/2}$  state. Similarly, Fig. 8.4 (b) and (d) shows the noise power of the differential intensity as the frequency of the Raman pump ( $\Delta_{Raman}$ ) is scanned across the  $5D_{3/2}$  state. For 10 mW of Raman pump power, we see 1% absorption, where the hyperfine structure of the  $5D_{3/2}$  state is clearly visible in both the intensity trace (Figs. 8.4 (a)) and the noise trace from the SA (Figs. 8.4 (b)). However, as we decrease the power to 1 mW, the signal vanishes below the noise for

the intensity sweep (Figs. 8.4 (c)), but not the noise sweep (Figs. 8.4 (d)). In the noise traces, the black line is the classical shot noise limit and we see that we can detect the responses as weak as 5 dB below this limit.

Furthermore, past studies have shown that uneven clipping or absorption of the probe and conjugate beams can lead to large increases in the noise [156]. Particularly in this case, the absorption observed in Fig. 8.4 (a) is roughly 1% of the overall signal and the absorption is nearly overshadowed by the noise. However, due to the noise correlations in the twin-beams, this unbalanced loss produces a response in the noise on the order of 10 dBs, shown in Fig. 8.4 (b). This enhanced noise sensitivity is further demonstrated by Figs. 8.4 (c) & (d) for the oscilloscope and SA traces respectively. Here the Raman pump power has been decreased to 1 mW and we see no response from the differential intensity signal. However, we are still able to make out the resonances in the noise in Fig. 8.4 (d). Here, we are able to use these noise measurements as a signal to map out the structure of the resonance. We take successive measurements of this trace for decreasing powers and plot them in a 3-d mesh, shown by Fig. 8.5 (a)-(e) for different temperatures. From here on, we will focus on the differential noise and treat it as our signal since it has a much stronger response.

We experimentally test the coupling of the squeezed probe beam to the Raman pump in a ladder configuration, shown by Fig. 8.1 (b) and Fig. 8.3 (b). By coupling the squeezing field as opposed to a classical coherent field, we expect to see the absorption signals amid a noise floor, 5 dB lower than classical limits would allow. By utilizing the signal observed on the differential noise picked up by the spectrum analyzer, we can measure the response of the probe absorption as a function of power, Raman pump frequency, and temperature (atomic density). Such measurements give us a working range for application of this method and potential to estimate the use in other systems.

The method demonstrated here shows a clear advantage over classical light. By mak-

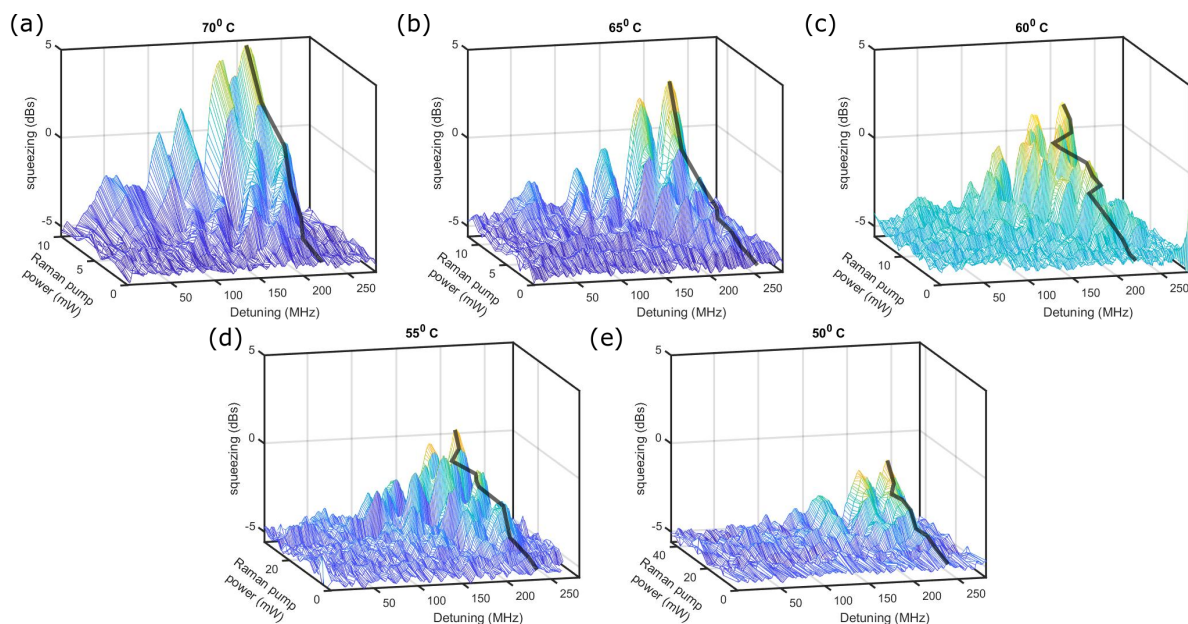


FIG. 8.5: (a)-(e) The mesh plot of noise traces, as the Raman pump power is changed and frequency is scanned. The different plots are for varying temperatures, as labeled. The black trace outlines the power dependence of the absorption signal for the  $5S_{1/2}, F = 2 \rightarrow 5D_{3/2}, F'' = 1$  transition which is extracted for the power dependent traces in Fig. 8.6

ing these power and temperature measurements, we can find a range of operations. Furthermore, it also allows us to how weak of a response the system is sensitive to and how well it operates compared to a similar classical system. The Raman pump power and temperature both have an effect on the optical depth of the medium and the corresponding two-photon resonance strength. In Rubidium, the atomic number density is tied directly to temperature and the amount of atoms in the vapor increases nonlinearly with temperature. So, the absorption also increases in a similar fashion with temperature. Additionally, the absorption decreases linearly with the power. We collect this temperature and power data to find the optimal working conditions with minimum power and atomic density which still allows detection of the Raman absorption response. This allows us to gauge the viability for application to other systems like trace gasses and molecular samples which may have lower concentrations or interaction strengths.

In order to clearly see the behavior and limits, we extracted the data from Fig. 8.5

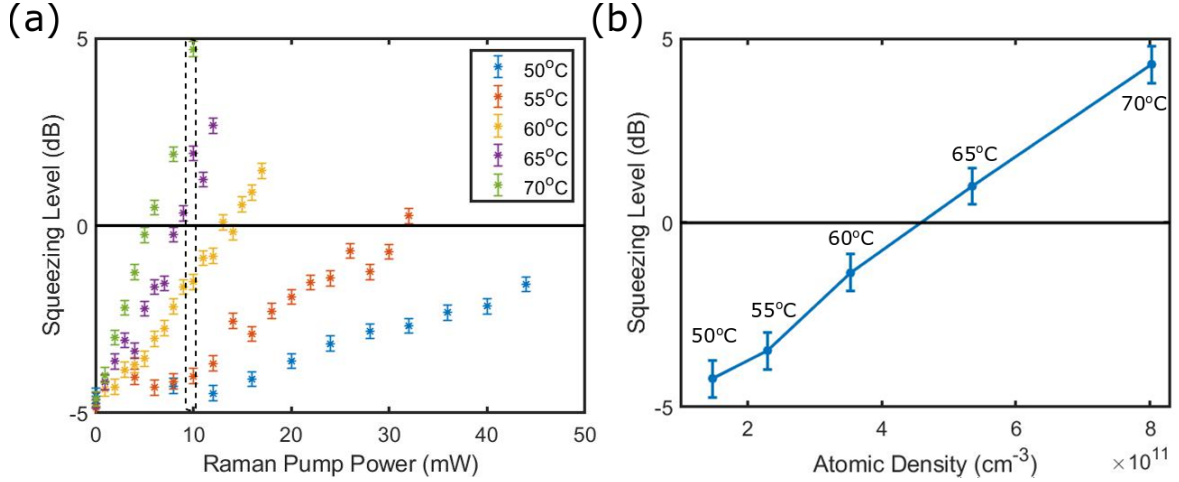


FIG. 8.6: (a) shows the power dependence shown by the black trace in Fig. 8.5 (a)-(e) for the  $5S_{1/2}, F = 2 \rightarrow 5D_{3/2}, F'' = 1$  two-photon transition absorption. In this, the power dependence at different Raman cell temperatures are plotted as different colors, as labeled. (b) shows the atomic density dependence of the two-photon absorption for a Raman pump power of 10 mW, shown by the dashed black outline in (a)

(a)-(e) for the different temperatures and powers, marked by the black line which lays on the peak for the  $5S_{1/2}, F = 2 \rightarrow 5D_{3/2}, F'' = 1$  state. Fig. 8.6 (a) shows the power dependence for each line extracted from the different temperature plots. The classical noise limit is shown by the solid black line at a squeezing value of zero and represents the limit for detection of coherent light. The solid blue line shows the noise limit for detection with the use of squeezed twin-beams. It can be seen that for any temperature lower than 60°C, that classical light would not be able to distinguish the absorption signal, even for larger Raman pump powers. The squeezed light can discern the signal for Raman pump powers as low as 10 mW and powers as low as 1 mW for higher cell temperatures. We also observe how the absorption responds to the temperature by plotting the data in the vertical box in Fig. 8.6 (a) as the noise power plotted against the temperature.

The data shows that we have a wide range of powers and temperatures that are open to exploration when using Raman absorption of squeezed light and are not accessible to classical light sources. In the ladder configuration, we have realized the detection of the

5D state via the detection of squeezed light which normally does not have access to this state. We were able to achieve these signals for weak interaction conditions, where we used low Raman pump powers and atomic densities on the order of  $10^{11} \text{ cm}^{-3}$ . Relating these powers and densities, we can compare the possibility of measuring the Raman response in other samples. Trace gasses are known to have densities in the range of  $10^{18} \text{ cm}^{-3}$  or higher [190]. The concentrations of molecules in solution tend to be on the order of  $10^{23} \text{ cm}^{-3}$  in general. In addition to this, molecular and crystal samples typically exhibit strong Raman responses. Here, we have used  $^{87}\text{Rb}$  vapor with a density of  $10^{12} \text{ cm}^{-3}$  or lower. This is substantially smaller than what we will see for other samples. However, further work will need to be done to gauge the interaction strengths in other media. We hope to see the benefits of squeezed light in these measurements when applied to other samples.

Additionally, since the two-photon process is performed using two narrow-line lasers, the resulting absorption spectrum can also boast an increased spectral resolution. A Raman spectrometer has a resolution of 5-10  $\text{cm}^{-1}$ . Using the ladder configuration in this experiment, we were measuring absorption features separated by 10's of MHz. This corresponds to less than a 10th of a  $\text{cm}^{-1}$ . Such a resolution with the increase applicability of squeezed light for Raman measurements and have broad implications in a range of fields.

### 8.3 Conclusion

In conclusion we have produced a proof-of-principle demonstration of the extension of the spectral range of squeezed light. By measuring the level structure of the  $5D_{3/2}$  state of  $^{87}\text{Rb}$ , we showed that this method can work for resonances far detuned from the optical frequency of either twin beam. In addition to the enhancement of Raman absorption spectroscopy sensitivity, we also see the extension of the range of the twin

beams. The dependence of the noise on the relative losses of the correlated twin beam is larger than would be expected from a simple application of the beam splitter model of loss to squeezed light. This provides an added sensitivity to the absorption measurements. Further testing of this coupling method is necessary, but this is a big first step in increasing the applicability of squeezed light.

# CHAPTER 9

## Conclusion and Outlook

This dissertation has focused on the improvement of various quantum information technologies using multi-photon light-matter interactions in hot Rb vapor. We demonstrate different methods of reducing or utilizing FWM for improving quantum sensing and quantum communication technologies.

We demonstrated the effectiveness of using a Raman two-photon absorption to reduce the effects of FWM as a nonlinear process competing with two-photon Raman transitions. We tested this method for experimental conditions mimicking both resonant EIT and off-resonant Raman memory. In the case of EIT memory, we used the  $^{85}\text{Rb}$  isotope to produce the FWM based amplification. Then we used a Raman pump field coupled to the newly generated conjugate field in a two-photon resonance with the  $5S_{1/2}, 5D_{3/2}$  states of the  $^{87}\text{Rb}$  isotope, in the same cell. In this scenario, we were able to see up to 40% reduction in the conjugate field generation which also limited the amplification of the probe signal field. Further improvement may be possible with optimization of the isotope mixture and increased pump powers. In the case of the Raman memory, we observed nearly 85% conjugate absorption. This case was particularly useful since the two-photon absorption



was performed in the same  $^{85}\text{Rb}$  isotope the FWM was generated in, removing the need for isotope optimization. This increased absorption in the Raman memory case, compared to the EIT memory, is due to the proximity of the newly generated conjugate field to the atomic resonance. Since publication, this work has seen use in Raman memories which used other absorption configurations to generate built in noise suppression [191] and enhancing FWM using stimulated Raman scattering [192].

We also demonstrated frequency conversion using FWM. By using a two-photon excitation from the  $^{85}\text{Rb}$   $5S_{1/2}$  to the  $5D_{3/2}$ , we observed and characterized the generation of blue collimated light. We explored two cases, one where the virtual state of the two-photon coupling was on or near the  $5P_{1/2}$  state and the other where the virtual state was on the  $5P_{3/2}$  state. The proximity of the virtual state to the  $5P_{1/2}$  state resulted in much stronger generation of blue light. We also looked at the effect of polarization and thus the Zeeman level dependence on the transitions and found that the polarization played a large role in the blue light generation. The effects of ground state repumping also played a big role in replenishing the ground state for atoms which used alternative relaxation pathways. We found that the power ratio of the repump field to the pump field played a role in optimum generation of blue light. When the repump power was much lower than the FWM pumps, we observed that the output of blue light would actually begin to decrease, this was also found to be true for simulations as well.

With squeezed twin beams, we demonstrated the transfer of OAM modes of light from the probe and pump fields to the conjugate with the use of FWM. Even under conditions where the conjugate field was generated in an OAM very different  $\Delta\ell = 4$  from the probe OAM, we still observed a strong level of correlations between the twin-beams, nearly -4 dBs of squeezing. By using structured light in FWM, we can utilize this for applications in quantum imaging and quantum communications. The OAM modes offer an orthogonal basis and twin-beams provide entanglement of photons. By utilizing structured light, the

channel capacity can be increased.

We built and demonstrated the operation of a polarization based truncated SU(1,1) interferometer. In this system, we are able to generate the local oscillators at the same time as our squeezed twin beams, giving added phase stability to the system. In addition to this, the symmetry in the interferometer allows for low frequency noise cancellation built into the system. This allowed for the measurement of squeezing of -2 dB at detection frequencies as low as 200 Hz, limited by the dark noise of the detector. This level of squeezing satisfies the criteria for inseparability for continuous variable entanglement. This are ideal operating conditions for quantum imaging since cameras with quantum efficiency are limited to these speeds. It is possible to improve this device by better filtering of the pumping field. A test for the future will be the demonstration of the generation polarization-entangled bell states. This interferometer can be a source of such states, by simply removing the seed field from the LO port. This will generate two sets of two-mode squeezed vacuums, which when combined will yield the polarization-entangled states [13, 14].

We demonstrated the improvement upon two-photon absorption spectroscopy with the use of squeezed twin-beams. By coupling the amplified probe beam with a Raman pumping field, we were able to measure probe absorptions for Raman pump powers as low 1 mW. This was possible due to the nearly 5 dBs of intensity difference squeezing. In the case of classical beams, it required at least 10 mW of power under the same conditions to see a response. In addition to this, we found that monitoring the differential noise of the twin beams makes for a more sensitive signal in response to the absorption than the differential intensity sweep. In the furture, we will modulate the pump frequency to elicit an even stronger response and work with lower powers and temperatures. We will also couple the Raman pump in a  $\Lambda$  configuration in molecular samples and test this method to probe vibration modes.

In addition to this, we can utilize spatial correlations between twin beams for quantum

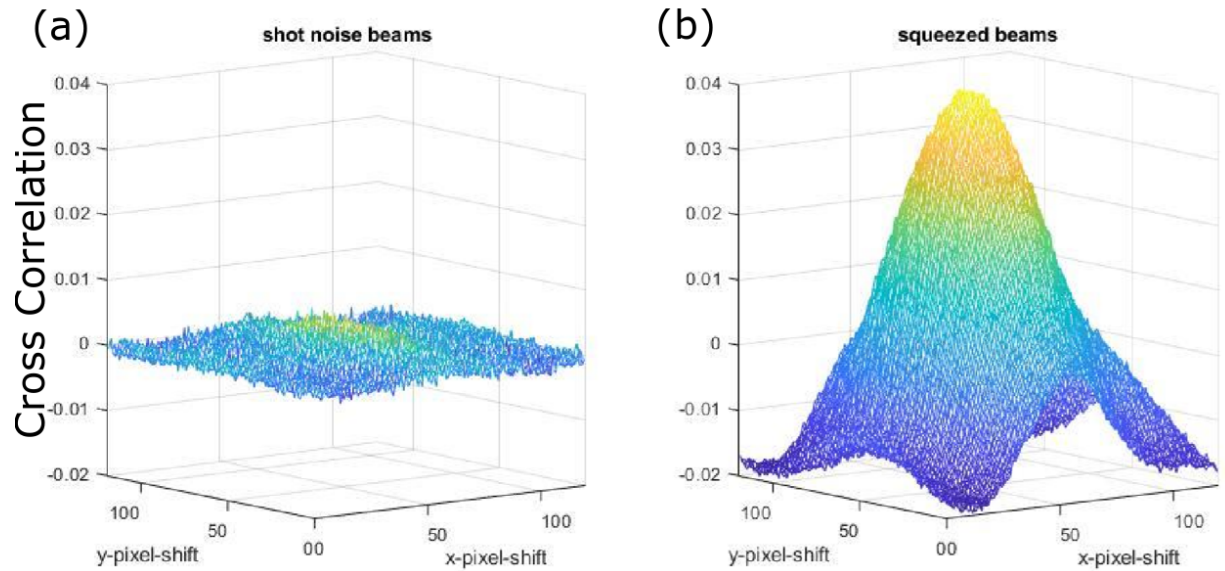


FIG. 9.1: (a) shows the cross correlation of two classical beams. (b) shows the cross correlation between the two-mode squeezed twin-beams.

imaging. Further research and analysis of twin beams with a camera could lead to a better understanding of the mode structure of the squeezed light. Along this path, we have already performed preliminary measurements using a camera to map the correlations of twin-beams, shown in Fig. 9.1 [187, 193]. The next step will be to map the correlations of structured twin beams.

In conclusion, the advancements presented here, on the utility of multi-photon processes, will have applications in the fields of quantum metrology [5, 6, 11, 12], quantum communications [7, 13–16], and quantum imaging. The FWM process is a versatile tool and we used it for the generation of entangled beams applications secure communication protocols, the transfer of orbital angular momentum in light for expanding the bandwidth for communications, and noise reduction for interferometric and spectral sensing. We also present a method using Raman absorption to compliment the spectral range of squeezed light to gain sensitivity for spectroscopic measurements of molecular samples or Rydberg atoms [11, 12]. This technique will also be extendable to other forms of squeezing. We

also used Raman absorption for the suppression of FWM, which is detrimental to quantum memories. The advancements presented have a potential impact diverse and broad range of fields not only in quantum optics, but also in biology and chemistry [5, 6].

## BIBLIOGRAPHY

- [1] V. Chickarmane and S. V. Dhurandhar, *Phys. Rev. A* **54**, 786 (1996).
- [2] E. E. Mikhailov, K. Goda, T. Corbitt, and N. Mavalvala, *Phys. Rev. A* **73**, 053810 (2006), [gr-qc/0508102](https://arxiv.org/abs/gr-qc/0508102), URL <http://link.aps.org/doi/10.1103/PhysRevA.73.053810>.
- [3] J. Aasi, J. Abadie, B. P. Abbott, R. Abbott, T. D. Abbott, M. R. Abernathy, C. Adams, T. Adams, P. Addesso, R. X. Adhikari, et al., *Nature Photonics* **7**, 613–619 (2013), URL <http://www.nature.com/nphoton/journal/v7/n8/full/nphoton.2013.177.html>.
- [4] S. S. Y. Chua, B. J. J. Slagmolen, D. A. Shaddock, and D. E. McClelland, *Classical and Quantum Gravity* **31**, 183001 (2014), URL <https://doi.org/10.1088/0264-9381/31/18/183001>.
- [5] B. J. Lawrie, P. D. Lett, A. M. Marino, and R. C. Pooser, *ACS Photonics* **6**, 1307 (2019), <https://doi.org/10.1021/acsp Photonics.9b00250>, URL <https://doi.org/10.1021/acsp Photonics.9b00250>.
- [6] F. Hudelist, J. Kong, C. Liu, J. Jing, Z. Ou, and W. Zhang, *Nature communications* **5**, 3049 (2014).
- [7] V. Boyer, A. M. Marino, R. C. Pooser, and P. D. Lett, *Science* **321**, 544 (2008), URL <http://link.aps.org/doi/10.1103/PhysRevA.78.043816>.

- [8] A. M. Marino, V. Boyer, R. C. Pooser, P. D. Lett, K. Lemons, and K. M. Jones, Phys. Rev. Lett. **101**, 093602 (2008), URL <https://link.aps.org/doi/10.1103/PhysRevLett.101.093602>.
- [9] M. W. Holtfreerich and A. M. Marino, Phys. Rev. A **93**, 063821 (2016), URL <https://link.aps.org/doi/10.1103/PhysRevA.93.063821>.
- [10] A. Kumar, H. Nunley, and A. M. Marino, Phys. Rev. A **95**, 053849 (2017), URL <https://link.aps.org/doi/10.1103/PhysRevA.95.053849>.
- [11] M. T. Simons, A. H. Haddab, J. A. Gordon, D. Novotny, and C. L. Holloway, IEEE Access **7**, 164975 (2019).
- [12] M. T. Simons, A. H. Haddab, and J. A. Gordon, in *2019 Antenna Measurement Techniques Association Symposium (AMTA)* (2019), pp. 1–4.
- [13] T. S. Iskhakov, I. N. Agafonov, M. V. Chekhova, G. O. Rytikov, and G. Leuchs, Phys. Rev. A **84**, 045804 (2011), URL <https://link.aps.org/doi/10.1103/PhysRevA.84.045804>.
- [14] J. Park, H. Kim, and H. S. Moon, Physical review letters **122** **14**, 143601 (2019).
- [15] J. Park, H. Kim, and H. S. Moon, Opt. Lett. **45**, 2403 (2020), URL <http://ol.osa.org/abstract.cfm?URI=ol-45-8-2403>.
- [16] N. Prajapati and I. Novikova, Opt. Lett. **44**, 5921 (2019), URL <http://ol.osa.org/abstract.cfm?URI=ol-44-24-5921>.
- [17] H. Cao, S.-C. Gao, C. Zhang, J. Wang, D.-Y. He, B.-H. Liu, Z.-W. Zhou, Y.-J. Chen, Z.-H. Li, S.-Y. Yu, et al., Optica **7**, 232 (2019), URL <http://www.osapublishing.org/optica/abstract.cfm?URI=optica-7-3-232>.

- [18] N. Prajapati, N. Super, N. R. Lanning, J. P. Dowling, and I. Novikova, *Opt. Lett.* **44**, 739 (2019), URL <http://ol.osa.org/abstract.cfm?URI=ol-44-4-739>.
- [19] W. E. Lamb, W. P. Schleich, M. O. Scully, and C. H. Townes, *Laser Physics: Quantum Controversy in Action* (Springer New York, New York, NY, 1999), pp. 442–459, ISBN 978-1-4612-1512-7, URL [https://doi.org/10.1007/978-1-4612-1512-7\\_27](https://doi.org/10.1007/978-1-4612-1512-7_27).
- [20] S. H. L. Guang S. He, *Physics of Nonlinear Optics* (World Scientific, River Edge, NJ, 1999), 1st ed.
- [21] P. A. Franken, A. E. Hill, C. W. Peters, and G. Weinreich, *Phys. Rev. Lett.* **7**, 118 (1961), URL <https://link.aps.org/doi/10.1103/PhysRevLett.7.118>.
- [22] P. A. M. Dirac, *Proc. R. Soc. Lond. A* **114**, 245 (1927).
- [23] M. O. Scully and M. S. Zubairy, *Quantum Optics* (Cambridge University Press, Cambridge, UK, 1997).
- [24] P. Meystre, *Elements of Quantum Optics* (Springer, 2007).
- [25] R. Bernheim, *Optical Pumping* (W. A. Benjamin, Inc., New York, 1965).
- [26] U. L. Andersen, T. Gehring, C. Marquardt, and G. Leuchs, *Physica Scripta* **91**, 053001 (2016), URL <https://doi.org/10.1088%2F0031-8949%2F91%2F5%2F053001>.
- [27] N. Sangouard, C. Simon, H. de Riedmatten, and N. Gisin, *Rev. Mod. Phys.* **83**, 33 (2011), URL <https://link.aps.org/doi/10.1103/RevModPhys.83.33>.
- [28] K. Heshami, D. G. England, P. C. Humphreys, P. J. Bustard, V. M. Acosta, J. Nunn, and B. J. Sussman, *Journal of Modern Optics* **63**, 2005 (2016), <http://dx.doi.org/>

10.1080/09500340.2016.1148212, URL <http://dx.doi.org/10.1080/09500340.2016.1148212>.

- [29] M. S. Underwood, Master's thesis, University of Calgary, CALGARY, ALBERTA (2008).
- [30] W. Tittel, M. Afzelius, T. Chanelière, R. Cone, S. Kröll, S. Moiseev, and M. Sellars, *Laser & Photonics Reviews* **4**, 244 (2010), <https://onlinelibrary.wiley.com/doi/pdf/10.1002/lpor.200810056>, URL <https://onlinelibrary.wiley.com/doi/abs/10.1002/lpor.200810056>.
- [31] J. P. Marangos, *J. Mod. Opt.* **45**, 471 (1998).
- [32] D. F. Phillips, A. Fleischhauer, A. Mair, R. L. Walsworth, and M. D. Lukin, *Phys. Rev. Lett.* **86**, 783 (2001).
- [33] E. E. Mikhailov, V. A. Sautenkov, Y. V. Rostovtsev, and G. R. Welch, *JOSA B* **21**, 425 (2004), [quant-ph/0309151](https://arxiv.org/abs/quant-ph/0309151).
- [34] B. J. Dalton and P. L. Knight, *Opt. Commun.* **42**, 411 (1982).
- [35] A. M. Akulshin, A. Cimmino, A. I. Sidorov, P. Hannaford, and G. I. Opat, *Phys. Rev. A* **67**, 011801 (2003), URL <http://link.aps.org/doi/10.1103/PhysRevA.67.011801>.
- [36] P. S. Michelberger, T. F. M. Champion, M. R. Sprague, K. T. Kaczmarek, M. Barbieri, X. M. Jin, D. G. England, W. S. Kolthammer, D. J. Saunders, J. Nunn, et al., *New Journal of Physics* **17**, 043006 (2015), URL <http://stacks.iop.org/1367-2630/17/i=4/a=043006>.
- [37] M. Dabrowski, R. Chrapkiewicz, and W. Wasilewski, *Opt. Express* **22**, 26076 (2014), URL <http://www.opticsexpress.org/abstract.cfm?URI=oe-22-21-26076>.



- [38] P. R. Hemmer, A. V. Turukhin, M. S. Shahriar, and J. A. Musser, *Opt. Lett.* **26**, 361 (2001), URL <http://ol.osa.org/abstract.cfm?URI=ol-26-6-361>.
- [39] C. Santori, D. Fattal, S. M. Spillane, M. Fiorentino, R. G. Beausoleil, A. D. Greentree, P. Olivero, M. Draganski, J. R. Rabeau, P. Reichart, et al., *Opt. Express* **14**, 7986 (2006), URL <http://www.opticsexpress.org/abstract.cfm?URI=oe-14-17-7986>.
- [40] V. M. Acosta, K. Jensen, C. Santori, D. Budker, and R. G. Beausoleil, *Phys. Rev. Lett.* **110**, 213605 (2013), URL <https://link.aps.org/doi/10.1103/PhysRevLett.110.213605>.
- [41] P. J. Bustard, R. Lausten, D. G. England, and B. J. Sussman, *Phys. Rev. Lett.* **111**, 083901 (2013), URL <https://link.aps.org/doi/10.1103/PhysRevLett.111.083901>.
- [42] G. Romanov, C. O'Brien, and I. Novikova, *Journal of Modern Optics* **63**, 2048 (2016), <http://dx.doi.org/10.1080/09500340.2015.1133856>, URL <http://dx.doi.org/10.1080/09500340.2015.1133856>.
- [43] N. Prajapati, G. Romanov, and I. Novikova, *J. Opt. Soc. Am. B* **34**, 1994 (2017), URL <http://josab.osa.org/abstract.cfm?URI=josab-34-9-1994>.
- [44] Y.-S. Lee and H. S. Moon, *Opt. Express* **24**, 10723 (2016), URL <http://www.opticsexpress.org/abstract.cfm?URI=oe-24-10-10723>.
- [45] N. Lauk, C. O'Brien, and M. Fleischhauer, *Phys. Rev. A* **88**, 013823 (2013), URL <http://link.aps.org/doi/10.1103/PhysRevA.88.013823>.
- [46] M. D. Lukin, M. Fleischhauer, A. S. Zibrov, H. G. Robinson, V. L. Velichansky, L. Hollberg, and M. O. Scully, *Phys. Rev. Lett.* **79**, 2959 (1997).

- [47] V. Wong, R. S. Bennink, A. M. Marino, R. W. Boyd, C. R. Stroud, and F. A. Narducci, Phys. Rev. A **70**, 053811 (2004), URL <https://link.aps.org/doi/10.1103/PhysRevA.70.053811>.
- [48] K.-i. Harada, K. Mori, J. Okuma, N. Hayashi, and M. Mitsunaga, Phys. Rev. A **78**, 013809 (2008), URL <http://link.aps.org/doi/10.1103/PhysRevA.78.013809>.
- [49] A. Eilam, A. D. Wilson-Gordon, and H. Friedmann, Opt. Lett. **33**, 1605 (2008), URL <http://ol.osa.org/abstract.cfm?URI=ol-33-14-1605>.
- [50] I. Vurgaftman and M. Bashkansky, Phys. Rev. A **87**, 063836 (2013), URL <http://link.aps.org/doi/10.1103/PhysRevA.87.063836>.
- [51] K. Zhang, J. Guo, L. Q. Chen, C. Yuan, Z. Y. Ou, and W. Zhang, Phys. Rev. A **90**, 033823 (2014), URL <http://link.aps.org/doi/10.1103/PhysRevA.90.033823>.
- [52] D. J. Saunders, J. H. D. Munns, T. F. M. Champion, C. Qiu, K. T. Kaczmarek, E. Poem, P. M. Ledingham, I. A. Walmsley, and J. Nunn, Phys. Rev. Lett. **116**, 090501 (2016), URL <https://link.aps.org/doi/10.1103/PhysRevLett.116.090501>.
- [53] J. Nunn, S. Thomas, J. Munns, K. Kaczmarek, C. Qiu, A. Feizpour, E. Poem, B. Brecht, D. Saunders, P. Ledingham, et al., <https://arxiv.org/abs/1601.00157> (2016), URL <https://arxiv.org/abs/1601.00157>.
- [54] Y. Zhang, U. Khadka, B. Anderson, and M. Xiao, Phys. Rev. Lett. **102**, 013601 (2009), URL <https://link.aps.org/doi/10.1103/PhysRevLett.102.013601>.
- [55] C. Li, Z. Jiang, Y. Zhang, Z. Zhang, F. Wen, H. Chen, Y. Zhang, and M. Xiao, Phys. Rev. Applied **7**, 014023 (2017), URL <https://link.aps.org/doi/10.1103/PhysRevApplied.7.014023>.

- [56] Y. Du, Y. Zhang, C. Zuo, C. Li, Z. Nie, H. Zheng, M. Shi, R. Wang, J. Song, K. Lu, et al., Phys. Rev. A **79**, 063839 (2009), URL <https://link.aps.org/doi/10.1103/PhysRevA.79.063839>.
- [57] M. Fleischhauer, U. Rathe, and M. O. Scully, Phys. Rev. A **46**, 5856 (1992).
- [58] R. W. Boyd, M. S. Malcuit, D. J. Gauthier, and K. Rzaewski, Phys. Rev. A **35**, 1648 (1987), URL <https://link.aps.org/doi/10.1103/PhysRevA.35.1648>.
- [59] W. R. Garrett, Phys. Rev. Lett. **70**, 4059 (1993), URL <https://link.aps.org/doi/10.1103/PhysRevLett.70.4059>.
- [60] A. I. Lvovsky, S. R. Hartmann, and F. Moshary, Phys. Rev. Lett. **82**, 4420 (1999), URL <https://link.aps.org/doi/10.1103/PhysRevLett.82.4420>.
- [61] A. G. Radnaev, Y. O. Dudin, R. Zhao, H. H. Jen, S. D. Jenkins, A. Kuzmich, and T. A. B. Kennedy, Nature Photon. **6**, 894–899 (2010).
- [62] K. T. Kaczmarek, P. M. Ledingham, B. Brecht, S. E. Thomas, G. S. Thekkadath, O. Lazo-Arjona, J. H. D. Munns, E. Poem, A. Feizpour, D. J. Saunders, et al. (2017), 1704.00013, URL <http://arxiv.org/abs/1704.00013>.
- [63] J. Keaveney, A. Sargsyan, D. Sarkisyan, A. Papoyan, and C. S. Adams, Journal of Physics B: Atomic, Molecular and Optical Physics **47**, 075002 (2014), URL <https://doi.org/10.1088%2F0953-4075%2F47%2F7%2F075002>.
- [64] G. O. Ariunbold, V. A. Sautenkov, and M. O. Scully, Physics Letters A **376**, 335 (2012), ISSN 0375-9601, URL <http://www.sciencedirect.com/science/article/pii/S03759601111014198>.
- [65] A.S.Zibrov, M.D.Lukin, L.Hollberg, and M.O.Scully, Phys. Rev. A **65**, 051801 (2002).

- [66] A. M. Akulshin, R. J. McLean, A. I. Sidorov, and P. Hannaford, *Opt. Express* **17**, 22861 (2009), URL <http://www.opticsexpress.org/abstract.cfm?URI=oe-17-25-22861>.
- [67] A. Vernier, S. Franke-Arnold, E. Riis, and A. S. Arnold, *Opt. Express* **18**, 17020 (2010), URL <http://www.opticsexpress.org/abstract.cfm?URI=oe-18-16-17020>.
- [68] E. Brekke and L. Alderson, *Opt. Lett.* **38**, 2147 (2013), URL <http://ol.osa.org/abstract.cfm?URI=ol-38-12-2147>.
- [69] M. B. Kienlen, N. T. Holte, H. A. Dassonville, A. M. C. Dawes, K. D. Iversen, R. M. McLaughlin, and S. K. Mayer, *American Journal of Physics* **81**, 442 (2013), <http://dx.doi.org/10.1119/1.4795311>, URL <http://dx.doi.org/10.1119/1.4795311>.
- [70] J. F. Sell, M. A. Gearba, B. D. DePaola, and R. J. Knize, *Opt. Lett.* **39**, 528 (2014), URL <http://ol.osa.org/abstract.cfm?URI=ol-39-3-528>.
- [71] A. Akulshin, D. Budker, and R. McLean, *Opt. Lett.* **39**, 845 (2014), URL <http://ol.osa.org/abstract.cfm?URI=ol-39-4-845>.
- [72] E. Brekke and E. Herman, *Opt. Lett.* **40**, 5674 (2015), URL <http://ol.osa.org/abstract.cfm?URI=ol-40-23-5674>.
- [73] T. Meijer, J. D. White, B. Smeets, M. Jeppesen, and R. E. Scholten, *Opt. Lett.* **31**, 1002 (2006), URL <http://ol.osa.org/abstract.cfm?URI=ol-31-7-1002>.
- [74] A. M. Akulshin, D. Budker, and R. J. McLean, *J. Opt. Soc. Am. B* **34**, 1016 (2017), URL <http://josab.osa.org/abstract.cfm?URI=josab-34-5-1016>.

- [75] A. Akulshin, C. Perrella, G.-W. Truong, R. McLean, and A. Luiten, *Journal of Physics B: Atomic, Molecular and Optical Physics* **45**, 245503 (2012), URL <https://doi.org/10.1088%2F0953-4075%2F45%2F24%2F245503>.
- [76] N. Prajapati, A. M. Akulshin, and I. Novikova, *J. Opt. Soc. Am. B* **35**, 1133 (2018), URL <http://josab.osa.org/abstract.cfm?URI=josab-35-5-1133>.
- [77] E. Brekke and S. Potier, *Appl. Opt.* **56**, 46 (2017), URL <http://ao.osa.org/abstract.cfm?URI=ao-56-1-46>.
- [78] G. Walker, A. S. Arnold, and S. Franke-Arnold, *Phys. Rev. Lett.* **108**, 243601 (2012), URL <https://link.aps.org/doi/10.1103/PhysRevLett.108.243601>.
- [79] A. M. Akulshin, R. J. McLean, E. E. Mikhailov, and I. Novikova, *Opt. Lett.* **40**, 1109 (2015), URL <http://ol.osa.org/abstract.cfm?URI=ol-40-6-1109>.
- [80] A. M. Akulshin, I. Novikova, E. E. Mikhailov, S. A. Suslov, and R. J. McLean, *Opt. Lett.* **41**, 1146 (2016), URL <http://ol.osa.org/abstract.cfm?URI=ol-41-6-1146>.
- [81] H.-A. Bachor and T. C. Ralph, *A Guide to Experiments in Quantum Optics* (Wiley-VCH, USA, 2004), 2nd ed., ISBN 3527403930.
- [82] R. E. Slusher, L. W. Hollberg, B. Yurke, J. C. Mertz, and J. F. Valley, *Phys. Rev. Lett.* **55**, 2409 (1985), URL <http://link.aps.org/doi/10.1103/PhysRevLett.55.2409>.
- [83] M. Dowran, A. Kumar, B. J. Lawrie, R. C. Pooser, and A. M. Marino, *Optica* **5**, 628 (2018), URL <http://www.osapublishing.org/optica/abstract.cfm?URI=optica-5-5-628>.

- [84] Q. Glorieux, L. Guidoni, S. Guibal, J.-P. Likforman, and T. Coudreau, in *Quantum Optics*, edited by V. N. Zadkov and T. Durt, International Society for Optics and Photonics (SPIE, 2010), vol. 7727, pp. 9 – 16, URL <https://doi.org/10.1117/12.854953>.
- [85] X. Guo, X. Li, N. Liu, L. Yang, and Z. Y. Ou, *Applied Physics Letters* **101**, 261111 (2012), <https://doi.org/10.1063/1.4773303>, URL <https://doi.org/10.1063/1.4773303>.
- [86] H. Vahlbruch, M. Mehmet, K. Danzmann, and R. Schnabel, *Phys. Rev. Lett.* **117**, 110801 (2016), URL <https://link.aps.org/doi/10.1103/PhysRevLett.117.110801>.
- [87] I. R. Berchera and I. P. Degiovanni, *Metrologia* **56**, 024001 (2019), URL <https://doi.org/10.1088%2F1681-7575%2Faaf7b2>.
- [88] A. Mosset, F. Devaux, and E. Lantz, *Phys. Rev. Lett.* **94**, 223603 (2005), URL <https://link.aps.org/doi/10.1103/PhysRevLett.94.223603>.
- [89] M. A. Taylor, J. Janousek, V. Daria, J. Knittel, B. Hage, H.-A. Bachor, and W. P. Bowen, *Nature Photonics* **7**, 229 (2013), ISSN 1749-4893, URL <https://doi.org/10.1038/nphoton.2012.346>.
- [90] M. A. Taylor and W. P. Bowen, *Physics Reports* **615**, 1 (2016), ISSN 0370-1573, quantum metrology and its application in biology, URL <http://www.sciencedirect.com/science/article/pii/S0370157315005001>.
- [91] F. Wolfgramm, A. Cerè, F. A. Beduini, A. Predojević, M. Koschorreck, and M. W. Mitchell, *Phys. Rev. Lett.* **105**, 053601 (2010), URL <http://link.aps.org/doi/10.1103/PhysRevLett.105.053601>.

- [92] T. Horrom, R. Singh, J. P. Dowling, and E. E. Mikhailov, *Phys. Rev. A* **86**, 023803 (2012), URL <https://link.aps.org/doi/10.1103/PhysRevA.86.023803>.
- [93] J. Aasi, J. Abadie, B. P. Abbott, R. Abbott, T. D. Abbott, M. R. Abernathy, C. Adams, T. Adams, P. Addesso, R. X. Adhikari, et al., *Nature Photonics* **7**, 613 (2013), ISSN 1749-4893, URL <https://doi.org/10.1038/nphoton.2013.177>.
- [94] A. Pathak and A. Ghatak, *Journal of Electromagnetic Waves and Applications* **32**, 229 (2018), <https://doi.org/10.1080/09205071.2017.1398109>, URL <https://doi.org/10.1080/09205071.2017.1398109>.
- [95] C. Xu, L. Zhang, S. Huang, T. Ma, F. Liu, H. Yonezawa, Y. Zhang, and M. Xiao, *Photon. Res.* **7**, A14 (2019), URL <http://www.osapublishing.org/prj/abstract.cfm?URI=prj-7-6-A14>.
- [96] G. Hétet, B. C. Buchler, O. Glöeckl, M. T. L. Hsu, A. M. Akulshin, H. A. Bachor, and P. K. Lam, *Opt. Express* **16**, 7369 (2008), URL <http://www.opticsexpress.org/abstract.cfm?URI=oe-16-10-7369>.
- [97] L.-M. Duan, G. Giedke, J. I. Cirac, P. Zoller, and A. K. Pati, *Quantum Information with Continuous Variables* (Springer Netherlands, Dordrecht, 2003), ISBN 978-94-015-1258-9, URL [https://doi.org/10.1007/978-94-015-1258-9\\_13](https://doi.org/10.1007/978-94-015-1258-9_13).
- [98] J. Du, L. Cao, K. Zhang, and J. Jing, *Applied Physics Letters* **110**, 241103 (2017).
- [99] M. Lassen, G. Leuchs, and U. L. Andersen, *Phys. Rev. Lett.* **102**, 163602 (2009), URL <https://link.aps.org/doi/10.1103/PhysRevLett.102.163602>.
- [100] S. Chen, B. Yang, Y. He, Z. Xie, M. Su, J. Liu, J. Xiao, Y. Li, G. Zhao, and D. Fan, *Optics Communications* **452**, 405 (2019), ISSN 0030-4018, URL <http://www.sciencedirect.com/science/article/pii/S0030401819303001>.

- [101] Y. Shen, X. Wang, Z. Xie, C. Min, X. Fu, Q. Liu, M. Gong, and X. Yuan, *Light: Science & Applications* **8**, 90 (2019), ISSN 2047-7538, URL <https://doi.org/10.1038/s41377-019-0194-2>.
- [102] M. Vasnetsov and K. Staliunas, *Optical vortices* (Nova Science Publishers, NY, 1999).
- [103] G. Knöner, S. Parkin, T. A. Nieminen, V. L. Y. Loke, N. R. Heckenberg, and H. Rubinsztein-Dunlop, *Opt. Express* **15**, 5521 (2007), URL <http://www.opticsexpress.org/abstract.cfm?URI=oe-15-9-5521>.
- [104] O. Ilic, I. Kaminer, B. Zhen, O. D. Miller, H. Buljan, and M. Soljačić, *Science Advances* **3** (2017), <http://advances.sciencemag.org/content/3/6/e1602738.full.pdf>, URL <http://advances.sciencemag.org/content/3/6/e1602738>.
- [105] P. Woźniak, P. Banzer, F. Bouchard, E. Karimi, G. Leuchs, and R. W. Boyd, *Phys. Rev. A* **94**, 021803 (2016), URL <https://link.aps.org/doi/10.1103/PhysRevA.94.021803>.
- [106] L. Allen, M. W. Beijersbergen, R. J. C. Spreeuw, and J. P. Woerdman, *Phys. Rev. A* **45**, 8185 (1992), URL <https://link.aps.org/doi/10.1103/PhysRevA.45.8185>.
- [107] B. C. dos Santos, K. Dechoum, and A. Z. Khoury, *Phys. Rev. Lett.* **103**, 230503 (2009), URL <https://link.aps.org/doi/10.1103/PhysRevLett.103.230503>.
- [108] K. Liu, J. Guo, C. Cai, S. Guo, and J. Gao, *Phys. Rev. Lett.* **113**, 170501 (2014), URL <https://link.aps.org/doi/10.1103/PhysRevLett.113.170501>.
- [109] N. Bozinovic, Y. Yue, Y. Ren, M. Tur, P. Kristensen, H. Huang, A. E. Willner, and S. Ramachandran, *Science* **340**, 1545 (2013), ISSN 0036-8075, <http://science.sciencemag.org/content/340/6140/1545.full.pdf>, URL <http://science.sciencemag.org/content/340/6140/1545>.



- [110] G. Walker, A. S. Arnold, and S. Franke-Arnold, *Phys. Rev. Lett.* **108**, 243601 (2012), URL <https://link.aps.org/doi/10.1103/PhysRevLett.108.243601>.
- [111] W. T. Buono, L. F. C. Moraes, J. A. O. Huguenin, C. E. R. Souza, and A. Z. Khoury, *New Journal of Physics* **16**, 093041 (2014), URL <http://stacks.iop.org/1367-2630/16/i=9/a=093041>.
- [112] A. M. Akulshin, I. Novikova, E. E. Mikhailov, S. A. Suslov, and R. J. McLean, *Opt. Lett.* **41**, 1146 (2016), URL <http://ol.osa.org/abstract.cfm?URI=ol-41-6-1146>.
- [113] K. Shigematsu, Y. Toda, K. Yamane, and R. Morita, *Japanese Journal of Applied Physics* **52**, 08JL08 (2013), URL <http://stacks.iop.org/1347-4065/52/i=8S/a=08JL08>.
- [114] L. Chen and W. She, *Opt. Lett.* **34**, 1855 (2009), URL <http://ol.osa.org/abstract.cfm?URI=ol-34-12-1855>.
- [115] A. E. Willner, H. Huang, Y. Yan, Y. Ren, N. Ahmed, G. Xie, C. Bao, L. Li, Y. Cao, Z. Zhao, et al., *Adv. Opt. Photon.* **7**, 66 (2015), URL <http://aop.osa.org/abstract.cfm?URI=aop-7-1-66>.
- [116] D. Ma and X. Liu, in *2015 International Conference on Wireless Communications Signal Processing (WCSP)* (2015), pp. 1–5.
- [117] B. Yurke, S. L. McCall, and J. R. Klauder, *Phys. Rev. A* **33**, 4033 (1986), URL <https://link.aps.org/doi/10.1103/PhysRevA.33.4033>.
- [118] J. Harms, Y. Chen, S. Chelkowski, A. Franzen, H. Vahlbruch, K. Danzmann, and R. Schnabel, *Phys. Rev. D* **68**, 042001 (2003), URL <http://link.aps.org/doi/10.1103/PhysRevD.68.042001>.

- [119] B. E. Anderson, B. L. Schmittberger, P. Gupta, K. M. Jones, and P. D. Lett, *Phys. Rev. A* **95**, 063843 (2017), URL <https://link.aps.org/doi/10.1103/PhysRevA.95.063843>.
- [120] Y. Michael, L. Bello, M. Rosenbluh, and A. Pe'er, *npj Quantum Information* **5**, 81 (2019), ISSN 2056-6387, URL <https://doi.org/10.1038/s41534-019-0197-0>.
- [121] W. Du, J. Jia, J. F. Chen, Z. Y. Ou, and W. Zhang, *Opt. Lett.* **43**, 1051 (2018), URL <http://ol.osa.org/abstract.cfm?URI=ol-43-5-1051>.
- [122] B. E. Anderson, P. Gupta, B. L. Schmittberger, T. Horrom, C. Hermann-Avigliano, K. M. Jones, and P. D. Lett, *Optica* **4**, 752 (2017), URL <http://www.osapublishing.org/optica/abstract.cfm?URI=optica-4-7-752>.
- [123] P. Gupta, B. L. Schmittberger, B. E. Anderson, K. M. Jones, and P. D. Lett, *Opt. Express* **26**, 391 (2018), URL <http://www.opticsexpress.org/abstract.cfm?URI=oe-26-1-391>.
- [124] D. B. Horoshko, M. I. Kolobov, F. Gumpert, I. Shand, F. König, and M. V. Chekhova, *Journal of Modern Optics* **67**, 41 (2020), <https://doi.org/10.1080/09500340.2019.1674394>, URL <https://doi.org/10.1080/09500340.2019.1674394>.
- [125] D. A. Kopylov, K. Y. Spasibko, T. V. Murzina, and M. V. Chekhova, *New Journal of Physics* **21**, 033024 (2019), URL <https://doi.org/10.1088%2F1367-2630%2F2103024>.
- [126] W. W. Parson, *Modern Optical Spectroscopy With Exercises and Examples from Biophysics and Biochemistry* (Springer, 2015).

- [127] K. Eberhardt, C. Stiebing, C. Matthäus, M. Schmitt, and J. Popp, *Expert Review of Molecular Diagnostics* **15**, 773 (2015), pMID: 25872466, <https://doi.org/10.1586/14737159.2015.1036744>, URL <https://doi.org/10.1586/14737159.2015.1036744>.
- [128] A. Virga, C. Ferrante, G. Batignani, D. De Fazio, A. D. G. Nunn, A. C. Ferrari, G. Cerullo, and T. Scopigno, *Nature Communications* **10**, 3658 (2019), ISSN 2041-1723, URL <https://doi.org/10.1038/s41467-019-11165-1>.
- [129] C. W. Thiel, in *Semantic Scholar* (2001).
- [130] M. Gonze, R. Saint-Loup, J. Santos, B. Lavorel, R. Chaux, G. Millot, H. Berger, L. Bonamy, J. Bonamy, and D. Robert, *Chemical Physics* **148**, 417 (1990), ISSN 0301-0104, URL <http://www.sciencedirect.com/science/article/pii/0301010490890350>.
- [131] J. R. Nestor, *The Journal of Chemical Physics* **69**, 1778 (1978), <https://doi.org/10.1063/1.436712>, URL <https://doi.org/10.1063/1.436712>.
- [132] S. Shim and R. A. Mathies, *Journal of Raman Spectroscopy* **39**, 1526 (2008), <https://onlinelibrary.wiley.com/doi/pdf/10.1002/jrs.2109>, URL <https://onlinelibrary.wiley.com/doi/abs/10.1002/jrs.2109>.
- [133] B. Petrak, N. Djeu, and A. Muller, *Opt. Express* **22**, 21999 (2014), URL <http://www.opticsexpress.org/abstract.cfm?URI=oe-22-18-21999>.
- [134] F. Billard, D. Gachet, and H. Rigneault, *J. Opt. Soc. Am. B* **26**, 1295 (2009), URL <http://josab.osa.org/abstract.cfm?URI=josab-26-7-1295>.
- [135] G. Lu and B. Fei, *Journal of biomedical optics* **19**, 10901 (2014), ISSN 1560-2281, 24441941[pmid], URL <https://pubmed.ncbi.nlm.nih.gov/24441941>.

- [136] J. D. Jackson, *Classical Electrodynamics* (Wiley, New York, 1975).
- [137] S. C. Rand, *Nonlinear and Quantum Optics* (Oxford, 2010).
- [138] N. Zettili, *Quantum Mechanics Concepts and Applications* (Wiley, 2009).
- [139] S. E. Harris, *Physics Today* **50**, 36 (1997).
- [140] C. Affolderbach, S. Knappe, R. Wynands, A. V. Taichenachev, and V. I. Yudin, *Phys. Rev. A* **65**, 043810 (2002).
- [141] K. Qin, S. Hu, S. T. Retterer, I. I. Kravchenko, and S. M. Weiss, *Opt. Lett.* **41**, 753 (2016), URL <http://ol.osa.org/abstract.cfm?URI=ol-41-4-753>.
- [142] G. V. Romanov, Ph.D. thesis, College of William and Mary, Virginia, USA (2017).
- [143] M. T. Simons, Ph.D. thesis, College of William and Mary, Williamsburg (2014).
- [144] D. A. Steck (2010), URL <http://steck.us/alkalidata>.
- [145] M. Fleischhauer, A. Imamoglu, and J. P. Marangos, *Rev. Mod. Phys.* **77**, 633 (2005), URL <http://link.aps.org/doi/10.1103/RevModPhys.77.633>.
- [146] N. B. Phillips, Ph.D. thesis, College of William and Mary, Virginia, USA (2011).
- [147] M. Fleischhauer and M. Lukin, *PHYSICAL REVIEW A* **65** (2002), ISSN 1050-2947.
- [148] I. Novikova, A. B. Matsko, and G. R. Welch, *J. Opt. Soc. Am. B* **22**, 44 (2005), URL <http://josab.osa.org/abstract.cfm?URI=josab-22-1-44>.
- [149] H. Failache, P. Valente, G. Ban, V. Lorent, and A. Lezama, *Phys. Rev. A* **67**, 043810 (2003).

- [150] M. Klein, I. Novikova, D. F. Phillips, and R. L. Walsworth, *Journal of Modern Optics* **53**, 2583 (2006), <http://www.tandfonline.com/doi/pdf/10.1080/09500340600952135>, URL <http://www.tandfonline.com/doi/abs/10.1080/09500340600952135>.
- [151] R. Boyd, *Nonlinear Optics* (Academic Press, 2008).
- [152] A. G. Radnaev, Y. O. Dudin, R. Zhao, H. H. Jen, S. D. Jenkins, A. Kuzmich, and T. A. B. Kennedy, *Nature Research* **6**, 894 (2010), URL <https://www.nature.com/articles/nphys1773#citeas>.
- [153] M. Jain, H. Xia, G. Y. Yin, A. J. Merriam, and S. E. Harris, *Phys. Rev. Lett.* **77**, 4326 (1996).
- [154] E. Bahar, X. Ding, A. Dahan, H. Suchowski, and J. Moses, *Opt. Express* **26**, 25582 (2018), URL <http://www.opticsexpress.org/abstract.cfm?URI=oe-26-20-25582>.
- [155] K. Drese and M. Holthaus, *Eur. Phys. J. D* **5**, 063840 (1999), URL <https://link.springer.com/article/10.1007/s100530050236>.
- [156] M. Zhang, R. N. Lanning, Z. Xiao, J. P. Dowling, I. Novikova, and E. E. Mikhailov, *Phys. Rev. A* **93**, 013853 (2016), URL <https://link.aps.org/doi/10.1103/PhysRevA.93.013853>.
- [157] O. Emile and J. Emile, *Annalen der Physik* **530**, 1800111 (2018), <https://onlinelibrary.wiley.com/doi/pdf/10.1002/andp.201800111>, URL <https://onlinelibrary.wiley.com/doi/abs/10.1002/andp.201800111>.
- [158] C. C. Gary and P. L. Knight, *Introductory Quantum Optics* (Cambridge, 2005).

- [159] M. Jasperse, Master's thesis, The University of Melbourne, Melbourne (2010).
- [160] M. Turnbull, Ph.D. thesis, University of Birmingham, Birmingham (2013).
- [161] P. U. and S. J., *Differential Absorption Spectroscopy* (Springer, 2008).
- [162] M. Fleischhauer and M. D. Lukin, Phys. Rev. Lett. **84**, 5094 (2000), URL <https://link.aps.org/doi/10.1103/PhysRevLett.84.5094>.
- [163] I. Novikova, R. L. Walsworth, and Y. Xiao, Laser & Photonics Reviews **6**, 333 (2012), ISSN 1863-8899, URL <http://dx.doi.org/10.1002/lpor.201100021>.
- [164] K. F. Reim, P. Michelberger, K. C. Lee, J. Nunn, N. K. Langford, and I. A. Walmsley, Phys. Rev. Lett. **107**, 053603 (2011), URL <http://link.aps.org/doi/10.1103/PhysRevLett.107.053603>.
- [165] M. D. Lukin, Reviews of Modern Physics **75**, 457 (2003), URL <http://link.aps.org/abstract/RMP/v75/p457>.
- [166] T. Hong, A. V. Gorshkov, D. Patterson, A. S. Zibrov, J. M. Doyle, M. D. Lukin, and M. G. Prentiss, Phys. Rev. A **79**, 013806 (2009), URL <http://link.aps.org/abstract/PRA/v79/e013806/>.
- [167] N. B. Phillips, A. V. Gorshkov, and I. Novikova, J. Mod. Optics **56**, 1916 (2009).
- [168] J. Geng, G. T. Campbell, J. Bernu, D. B. Higginbottom, B. M. Sparkes, S. M. Assad, W. P. Zhang, N. P. Robins, P. K. Lam, and B. C. Buchler, New Journal of Physics **16**, 113053 (2014), URL <http://stacks.iop.org/1367-2630/16/i=11/a=113053>.
- [169] J. Nunn, I. A. Walmsley, M. G. Raymer, K. Surmacz, F. C. Waldermann, Z. Wang, and D. Jaksch, Phys. Rev. A **75**, 011401 (2007), URL <https://link.aps.org/doi/10.1103/PhysRevA.75.011401>.

- [170] A. V. Gorshkov, T. Calarco, M. D. Lukin, and A. S. Sørensen, *Phys. Rev. A* **77**, 043806 (2008), URL <http://link.aps.org/doi/10.1103/PhysRevA.77.043806>.
- [171] A. M. Akulshin, R. J. McLean, E. E. Mikhailov, and I. Novikova, *Opt. Lett.* **40**, 1109 (2015), URL <http://ol.osa.org/abstract.cfm?URI=ol-40-6-1109>.
- [172] B. Srivathsan, G. K. Gulati, B. Chng, G. Maslennikov, D. Matsukevich, and C. Kurtstiefer, *Phys. Rev. Lett.* **111**, 123602 (2013), URL <https://link.aps.org/doi/10.1103/PhysRevLett.111.123602>.
- [173] M. Parniak and W. Wasilewski, *Phys. Rev. A* **91**, 023418 (2015), URL <https://link.aps.org/doi/10.1103/PhysRevA.91.023418>.
- [174] A. Leszczyński, M. Parniak, and W. Wasilewski, *Opt. Express* **25**, 284 (2017), URL <http://www.opticsexpress.org/abstract.cfm?URI=oe-25-1-284>.
- [175] T. T. Grove, V. Sanchez-Villicana, B. C. Duncan, S. Maleki, and P. L. Gould, *Physica Scripta* **52**, 271 (1995), URL <http://stacks.iop.org/1402-4896/52/i=3/a=008>.
- [176] N. B. Phillips, I. Novikova, E. E. Mikhailov, D. Budker, and S. Rochester, *Journal of Modern Optics* **60**, 64 (2013), 1205.2567, URL <http://www.tandfonline.com/doi/abs/10.1080/09500340.2012.733433>.
- [177] R. F. Offer, D. Stulga, E. Riis, S. Franke-Arnold, and A. S. Arnold, *ArXiv e-prints* (2018), 1805.08190.
- [178] I. D. Maleev and G. A. Swartzlander, *J. Opt. Soc. Am. B* **20**, 1169 (2003), URL <http://josab.osa.org/abstract.cfm?URI=josab-20-6-1169>.
- [179] G. Molina-Terriza, J. P. Torres, and L. Torner, *Phys. Rev. Lett.* **88**, 013601 (2001), URL <https://link.aps.org/doi/10.1103/PhysRevLett.88.013601>.

- [180] J. P. Torres, Y. Deyanova, L. Torner, and G. Molina-Terriza, *Phys. Rev. A* **67**, 052313 (2003), URL <https://link.aps.org/doi/10.1103/PhysRevA.67.052313>.
- [181] B. Yurke, S. L. McCall, and J. R. Klauder, *Phys. Rev. A* **33**, 4033 (1986), URL <https://link.aps.org/doi/10.1103/PhysRevA.33.4033>.
- [182] M. V. Chekhova and Z. Y. Ou, *Adv. Opt. Photon.* **8**, 104 (2016), URL <http://aop.osa.org/abstract.cfm?URI=aop-8-1-104>.
- [183] Q. Glorieux, R. Dubessy, S. Guibal, L. Guidoni, J.-P. Likforman, T. Coudreau, and E. Arimondo, *Phys. Rev. A* **82**, 033819 (2010), URL <https://link.aps.org/doi/10.1103/PhysRevA.82.033819>.
- [184] P. Gupta, R. W. Speirs, K. M. Jones, and P. D. Lett, *Opt. Express* **28**, 652 (2020), URL <http://www.opticsexpress.org/abstract.cfm?URI=oe-28-1-652>.
- [185] C. Gerry and P. Knight, *Nonclassical light* (Cambridge University Press, 2004), p. 150–194.
- [186] L.-M. Duan, G. Giedke, J. I. Cirac, and P. Zoller, *Phys. Rev. Lett.* **84**, 2722 (2000), URL <https://link.aps.org/doi/10.1103/PhysRevLett.84.2722>.
- [187] A. Kumar, H. Nunley, and A. M. Marino, *Phys. Rev. A* **95**, 053849 (2017), URL <https://link.aps.org/doi/10.1103/PhysRevA.95.053849>.
- [188] S. M. Hendrickson, M. M. Lai, T. B. Pittman, and J. D. Franson, *Phys. Rev. Lett.* **105**, 173602 (2010), URL <https://link.aps.org/doi/10.1103/PhysRevLett.105.173602>.
- [189] A. J. Olson, E. J. Carlson, and S. K. Mayer, *American Journal of Physics* **74**, 218 (2006), <https://doi.org/10.1119/1.2173278>, URL <https://doi.org/10.1119/1.2173278>.



- [190] J. Wallace and P. Hobbs, *Atmospheric Science: An Introductory Survey* (Academic Press, 2006).
- [191] S. E. Thomas, T. M. Hird, J. H. D. Munns, B. Brecht, D. J. Saunders, J. Nunn, I. A. Walmsley, and P. M. Ledingham, *Phys. Rev. A* **100**, 033801 (2019), URL <https://link.aps.org/doi/10.1103/PhysRevA.100.033801>.
- [192] Z. Zhang, J. Feng, X. Liu, J. Sheng, Y. Zhang, Y. Zhang, and M. Xiao, *Opt. Lett.* **43**, 919 (2018), URL <http://ol.osa.org/abstract.cfm?URI=ol-43-4-919>.
- [193] S. Gnatiessoro, A. Mosset, E. Lantz, and F. Devaux, *OSA Continuum* **2**, 3393 (2019), URL <http://www.osapublishing.org/osac/abstract.cfm?URI=osac-2-12-3393>.

## VITA

### Nikunj Kumar Prajapati

Nikunj Prajapati was born in Nadiad, India and came to America at the age of 5. He grew up near Atlantic City, New Jersey, and stayed there for undergrad, attending Stockton University. After getting his B.S. in physics, he continued along the academic route and found himself at William & Mary as a graduate student. Here, he joined the research group of Irina Novikva and worked on using nonlinear optics for the enhancement of quantum technologies. In the next phase, he will work as a postdoc at the National Institute of Standards and Technology (NIST) in Boulder, Colorado on the detection of RF waves using Rydberg atoms.